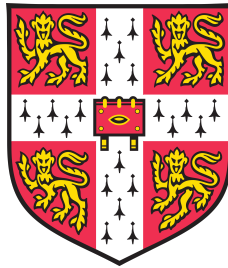# Skyrmions – beyond rigid body quantisation

## Christopher J. Halcrow

University of Cambridge

Department of Applied Mathematics and Theoretical Physics

Robinson College

March 2017

This dissertation is submitted for
the degree of Doctor of Philosophy

# Skyrmions – beyond rigid body quantisation.

## Christopher J. Halcrow

In the Skyrme model, nuclei are described as topological solitons known as Skyrmions. To make contact with nuclear data one must quantise these Skyrmions; most calculations to date have used rigid body quantisation, where the Skyrmions are allowed to rotate but remain rigid. The method reproduces some experimental results for light nuclei but there are some contradictions with data. In this thesis we study a more sophisticated quantisation scheme where the Skyrmions may deform, called vibrational quantisation, in the hope of fixing some of these problems.

Vibrational quantisation is applied to the dodecahedral $B = 7$ Skyrmion, which models Lithium-7. Using rigid body quantisation, the Skyrme model predicts a spin $\frac{7}{2}$ ground state while in reality the Lithium-7 nucleus ground state has spin $\frac{3}{2}$. We show that a quantisation which includes a 5-dimensional vibrational manifold of deformed Skyrme configurations remedies this problem, giving the correct ground state spin. Further, the model leads to a robust prediction that the ground state of the nucleus has a larger root mean square matter radius than the second quantum state, in contrast with standard nuclear models.

We consider the vibrational modes of the tetrahedral $B = 16$ Skyrmion, to describe Oxygen-16. Motivated by Skyrme dynamics, a special 2-dimensional submanifold of configurations is constructed. We study the manifold in detail by modelling it as a 6-punctured sphere with constant negative curvature. The Schrödinger equation is solved on the sphere and the results give an excellent fit to the experimental energy spectrum. The model describes an energy splitting between certain states with equal spins but opposite parities, which is hard to explain in other models. We also find the first ever isospin 0, spin-parity $0^-$ state in the Skyrme model. A method to calculate electromagnetic transition rates between states is formulated and then applied to our system.

By considering a special type of Skyrme configuration, where a single Skyrmion orbits a large core, we show that the Skyrme model can reproduce a classical spin-orbit force due to the structure of the Skyrme fields. We quantise this model to try and find out if the classical picture holds quantum mechanically.

*Dedicated to*
*Mam and Dad*

# Declaration

This dissertation is the result of my own work and includes nothing which is the outcome of work done in collaboration except as declared in the Preface and specified in the text.

It is not substantially the same as any that I have submitted, or, is being concurrently submitted for a degree or diploma or other qualification at the University of Cambridge or any other University or similar institution except as declared in the Preface and specified in the text. I further state that no substantial part of my dissertation has already been submitted, or, is being concurrently submitted for any such degree, diploma or other qualification at the University of Cambridge or any other University of similar institution except as specified in the text.


Christopher J. Halcrow

October 5, 2017

# Acknowledgements

I would like to thank my PhD supervisor Professor Nick Manton. He gave me freedom to research what I was interested in, while providing a guiding hand as I did. The biggest compliment I can give him is that I'm more interested in science now than I was at the start of this PhD. Much of this is due to Nick's enthusiasm and optimism about the subject. I thank him for passing some of this on to me.

My research has been influenced by countless conversations with my fellow Skyrmion researchers. Special thanks to Chris Lau for helping introduce me to the field and to Chris King for making our collaboration so enjoyable. Pavilion B has been a joy to work in, mostly because of the great people around. Thanks to the other HEP students from my year – Alex Arvanitakis, James Gundry and Carl Turner – as well as some old timers: Chris Blair, Alasdair Routh and Andrew Singleton who made me feel very welcome when I first arrived. Many thanks to Ruadhaí Dervan, Will Cook, Gavin Cheung, Nathan Procter, Alec Barns-Graham and Vishal Patil, all of whom made my PhD extra fun. Manda Stagg has helped with the many unusual queries I have had and it has always been comforting to know that she is there, in case of any emergency that may occur! I also commend her taste in film. The other inhabitants of B2.12, Rahul Jha and Ciaran Hughes, made sure that I never dreaded coming in to the office. I thank them for that, as well as their advice in navigating the world of research. However, they do still owe me a Snickers.

Beyond the confines of the CMS, the past seven years at Robinson College would never have been as enjoyable without Ros, Clive, Mat or Letty. Many thanks to them for all the good times and for their support. More support came from home and I must say a special thanks to my family, Kathy and Stuart Hubbard and the "Wacky Gang" for always being so encouraging!

# Contents

# List of Figures

# List of Tables

# Chapter 1

# Introduction

In the 1950s Tony Skyrme proposed a radical new model of nuclei which is now called the Skyrme model. It is a nonlinear field theory of pions which supports topologically non-trivial solutions called Skyrmions [1]. These are static, spatially localised field configurations which are labelled by an integer-valued topological charge, $B$. They are stable due to the topology of the system. Skyrme's idea was to identify these Skyrmions as nuclei, with the topological charge equal to the baryon number. The simplest Skyrmion has charge one and is spherically symmetric. Its low energy dynamics are identical to those of a point particle. Moreover when two $B = 1$ Skyrmions are widely separated their interaction resemble phenomenological nucleon-nucleon potentials [2]. Hence Skyrme's suggestion agrees with some basic phenomenology of nucleons.

The model looks less conventional as the baryon number is increased. When multiple charge one Skyrmions are put near each other, they conglomerate into a single object where individual Skyrmions lose their identity. Finite $B$ nuclei are described by these unusual objects. For example, the Helium-4 nucleus is modelled as a cubic Skyrmion. Here, there is no unique way to see where the four composite nucleons are within the nucleus. This is in stark contrast to many nuclear models which begin with a system of nucleons interacting via a phenomenological potential. A key advantage of the Skyrme model is that all interactions and dynamics are determined by the initial Lagrangian. This only has a few parameters, essentially an energy scale and a length scale. In addition, the theory unifies mesons and baryons. When Skyrme first proposed the model, these facts were enough

to generate interest in the topic. Later, Witten showed that baryons in large $N$ QCD act like solitons based on how their masses scale [3]. More recently Sakai and Sugimoto [4] rederived Skyrme's Lagrangian from a holographic QCD model. These observations, alongside the aforementioned attractive features of the Skyrme model motivates our study of the theory.

Nuclear models have a long history, dating back to Rutherford's discovery of the nucleus in 1909. We shall briefly review some popular models to try and place Skyrme's idea in a wider context. In the shell model, nuclei are described as a collection of nucleons which do not directly interact. Each nucleon only sees the others through an effective, central potential. This generates a Schrödinger equation for the nucleons and hence an energy spectrum. By the Pauli exclusion principle, levels of this spectrum are filled as $B$ is increased. Each level is called a shell. For special values of $B$, a shell is filled and the corresponding nucleus is tightly bound and very stable. These special values are called magic numbers and give rise to magic nuclei. The excited states of magic (or nearly magic) nuclei correspond to a single nucleon being excited to a higher energy shell; the spin of the nucleus is determined by the spin of the single excited nucleon. The shell model is highly successful near magic nuclei but less successful elsewhere on the nuclear table. The liquid drop model describes nuclei as charged spheres of liquid. The excited states correspond to collective motion on the surface of the sphere. The model successfully reproduces the energy spectrum and transition rates of nuclei such as Sulphur-32. Another set of ideas are the cluster models. In these, large nuclei are constructed using smaller nuclei. The Helium-4 nucleus, also known as the $\alpha$-particle, has very low binding energy. Hence it is often used as a building block for larger nuclei. The $\alpha$-particles are arranged in geometric shapes to create the larger nucleus and excited states are described by vibrations around the shapes. These three models have very different physics behind them: individual nucleon spins, collective motion and clusters are central to each respectively. Given their contradictory nature the most surprising fact is that they are all successful in describing certain nuclei. This variety shows the rich and wide range of physics present in nuclear theory. One aim of this thesis is to show that, when quantised appropriately, we can make a connection between the Skyrme model and these conventional yet disparate models.

The Skyrme model is valid in the low energy limit of QCD. Here the quark and

gluon degrees of freedom are frozen out; instead the mesonic degrees of freedom are relevant. In fact we will focus on only the lightest mesons: the pions. Hence the Lagrangian, $\mathcal{L}$, is constructed from the pion fields, $\boldsymbol{\pi}$. It is helpful to write these in terms of an $SU(2)$ valued matrix

$$U(t, \boldsymbol{x}) = \sigma(t, \boldsymbol{x}) + i\boldsymbol{\pi}(t, \boldsymbol{x}).\boldsymbol{\tau}\,, \tag{1.1}$$

where $\tau_i$ are the Pauli matrices and $\sigma$ is an auxiliary field which satisfies

$$\sigma^2 + \boldsymbol{\pi}.\boldsymbol{\pi} = 1\,, \tag{1.2}$$

so that $U \in SU(2)$. The low energy Lagrangian inherits Lorentz and chiral symmetry from the full theory. Chiral symmetry relates the up and down quarks in full QCD, giving them equal mass. This leads to a vanishing mass for all the pions and equal masses for the proton and neutron. The symmetry is only approximately realised in nature, broken by a small mass difference in the up and down quarks which leads to a small but non-zero pion mass. Hence in constructing $\mathcal{L}$, one should begin with a fully chiral symmetric Lagrangian and then add a small pion mass term to break this symmetry. The Skyrme model has classical field configurations - the Skyrmions - and their dynamics at its core and so it is essential to construct a Lagrangian with a well defined time evolution. In practice, this means $\mathcal{L}$ must have at most second order time derivatives. This restriction, along with Lorentz and approximate chiral symmetry leads us to write down the following Lagrangian

$$\mathcal{L} = -\frac{F_\pi^2}{16}\mathrm{Tr}\left(R_\mu R^\mu\right) + \frac{1}{32e^2}\mathrm{Tr}\left([R_\mu, R_\nu][R^\mu, R^\nu]\right) + \frac{1}{8}m_\pi^2 F_\pi^2\,\mathrm{Tr}(U - \mathbf{1}_2)\,, \tag{1.3}$$

where $R_\mu = (\partial_\mu U)U^\dagger$ is the right current of the Skyrme field, $F_\pi$ is the pion decay constant, $e$ is a dimensionless parameter and $m_\pi$ is the pion mass. It is more natural to work in Skyrme units. In these, the energy and length units are $F_\pi/4e$ and $2/eF_\pi$ respectively. The Lagrangian becomes

$$\mathcal{L} = -\frac{1}{2}\mathrm{Tr}\left(R_\mu R^\mu\right) + \frac{1}{16}\mathrm{Tr}\left([R_\mu, R_\nu][R^\mu, R^\nu]\right) + m^2\,\mathrm{Tr}(U - \mathbf{1}_2)\,, \tag{1.4}$$

where $m = 2m_\pi/eF_\pi$ is the dimensionless pion mass. The first term in (1.3) has second order spatial derivatives, and a Lagrangian containing only this term is called a sigma model. These theories do not support soliton solutions as one can scale any solution down to a point, which has zero energy. The next term in (1.3),

3

commonly called the Skyrme term, prevents the scaling instability seen in sigma models, allowing for stable soliton solutions.

If the pion mass were zero, the Lagrangian would be invariant under

$$U \to AUB^T \,, \tag{1.5}$$

where $A$ and $B$ are constant $SU(2)$ matrices. This is full chiral symmetry. A non-zero pion mass enforces $A = B$, breaking the $SU(2) \times SU(2)$ symmetry down to an $SU(2)$ symmetry known as isospin symmetry. The pions are the goldstone bosons associated with this symmetry breaking. With the non-zero pion mass, the Lagrangian is invariant under

$$U \to AUA^T \,. \tag{1.6}$$

This transformation is called an isorotation. It continuously cycles the pion fields into one another. Once quantised, the symmetry gives rise to isospin, the quantity which distinguishes protons and neutrons. While this is an exact symmetry, the proton-neutron pair has degenerate energy in the Skyrme model.

The pion mass term has another important consequence. Consider the static problem, which has Lagrangian

$$\mathbb{M}_B = \int -\frac{1}{2}\mathrm{Tr}\,(R_i R_i) - \frac{1}{16}\mathrm{Tr}\,([R_i, R_j][R_i, R_j]) - m^2\,\mathrm{Tr}(U - \mathbf{1}_2)\,d^3x\,. \tag{1.7}$$

We identify this as the rest mass of the nucleus for a given $B$. For a configuration to have finite mass, it must tend to the vacuum ($U = \mathbf{1}_2$) at spatial infinity. Hence, for static configurations with finite energy, we may compactify the sphere at $\infty$ into a point. This means the target space of the field is $\mathbb{R}^3 \cup \{\infty\} \cong S^3$, the 3-sphere. In addition the pion fields $U$ take values in $SU(2) \cong S^3$. Hence finite energy field configurations are maps from $S^3 \to S^3$. These maps are labelled by an integer $B$, the aforementioned topological charge. Although the conserved integer does not arise from a continuous symmetry, there does exist a topological current

$$\mathcal{B}_\mu = \frac{1}{24\pi^2}\epsilon_{\mu\nu\rho\sigma}\mathrm{Tr}\,(R^\nu R^\rho R^\sigma)\,, \tag{1.8}$$

which satisfies

$$B = \int \mathcal{B}_0\,d^3x \in \mathbb{Z}\,. \tag{1.9}$$

One may use a Bogomolny bound style argument [5] to show that the energy of a static field configuration is bounded by the baryon number as

$$\mathbb{M}_B \geq 12\pi^2 B \,. \tag{1.10}$$

The energy minimisers stay close to this bound, but never saturate it. The $B = 1$ Skyrmion has energy

$$\mathbb{M}_1 \approx 1.416 \times 12\pi^2 \times 1 \tag{1.11}$$

when $m = 1$. As $B$ increases, the solutions become closer to saturating the bound. In the $B \to \infty$ limit we find that

$$\lim_{B \to \infty} \mathbb{M}_B \approx 1.238 \times 12\pi^2 \times B \,. \tag{1.12}$$

In nuclear physics, the energy of a nucleus is linearly correlated with its baryon number. Hence it is natural to identify $B$ with baryon number. One may confirm this guess by including the Wess-Zumino-Witten term in (1.3). This leads to the derivation of the Gell-Mann–Nishijima equation

$$Q = \frac{1}{2}B + I_3 \,, \tag{1.13}$$

where $Q$ is the charge of a configuration and $I_3$ is its isospin projection [6]. This well known identity confirms $B$ as the baryon number.

The classical binding energy of a Skyrmion is the energy required to pull a Skyrmion apart into its consistory $B = 1$ clusters. This is

$$B\mathbb{M}_1 - \mathbb{M}_B \,. \tag{1.14}$$

If the inequality (1.10) was saturated for each $B$, the theory is called BPS. In these theories there is no classical binding energy. Nuclei have a similar definition of binding energy, it is the energy required to break a nucleus into individual protons and neutrons. The binding energy is an important physical quantity for a given nucleus. We know that $\alpha$-particles play an important role in nuclear physics; this is largely due to their particularly small binding energy.

## 1.1  Classical solutions

The Euler-Lagrange equations for a static field configuration are analytically intractable and we must find solutions numerically, for a given $B$. Our numerical

techniques are detailed in Appendix A. Alternatively, one could consider approximate solutions using the rational map [7] or Atiyah-Manton [8] constructions . We call any static solution, even a local minimum, a Skyrmion and distinguish the different Skyrmions in the same baryon sector by their symmetry. To visualise the Skyrmions one could plot the pion vector $\boldsymbol{\pi} = \{\pi_1, \pi_2, \pi_3\}$ at each point $\boldsymbol{x}$. We do this for the $B = 1$ and $B = 7$ Skyrmions in the leftmost plots of Figure 1.1. This does not give much information about the symmetries of the configuration which will be important for quantisation. To get this information visually we could plot a contour of constant energy or baryon density. However, the direction of the pion field did hold important information. To take account of both aspects we combine the two visualisation methods. We first colour the vectors of Figure 1.1 depending on their direction. They are coloured using the Runge colour sphere. The Skyrmion is white/black when $\pi_3$ equals $\pm 1$ and red, green and blue when $\pi_1 + i\pi_2$ is equal to 1, $\exp(2\pi i/3)$ and $\exp(4\pi i/3)$ respectively. This colouring scheme was originally proposed in [9]. We then colour the energy density contour depending on the value of $\boldsymbol{\pi}$ on the surface. This three step process is displayed in Figure 1.1. Looking at the final plot in each case, it is clear that the $B = 1$ and $B = 7$ Skyrmions have spherical and dodecahedral symmetries respectively.

The notion of symmetry is slightly complicated by the colouring of the Skyrmions. We say that a Skyrmion has a symmetry if it is invariant under a physical rotation followed by an isorotation. The isorotations are simply rotations of the pion field $\boldsymbol{\pi}$. Visually, isorotations are recolourings of the Skyrmion. The $B = 1$ Skyrmion has spherical symmetry since any rotation may be compensated by an isorotation.

The $B = 2$ and $B = 3$ Skyrmions have toroidal and tetrahedral symmetry respectively as shown in Figure 1.2. The tetrahedral Skyrmion may be broken into a $B = 1$ and $B = 2$ Skyrmion by pulling on a vertex as seen in Figure 1.3. This shows how closely the solutions are related despite looking rather different.

The $B = 4$ Skyrmion has a large classical binding energy due to its highly symmetric shape - a cube. Once quantised, the $B = 4$ Skyrmion models the $\alpha$-particle, showing that the Skyrme model has links with $\alpha$-particle models which are popular in nuclear theory [10]. The $\alpha$-particle is made from two protons and two neutrons. This appears to contradict the cubic model. However one may pull the cube into four $B = 1$ Skyrmions as in Figure 1.4 by pulling on four of its vertices, restoring the conventional picture. Note that there is not a unique way
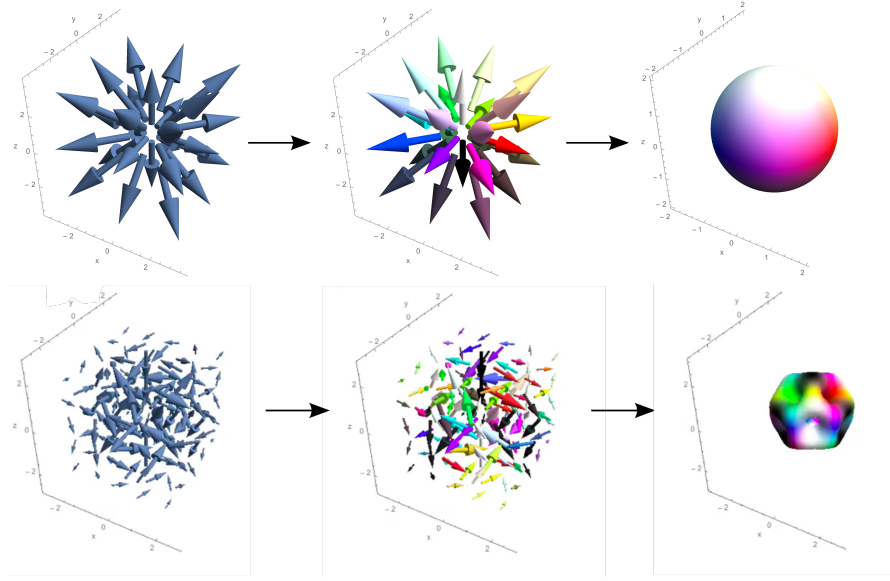
Figure 1.1: The process of colouring the energy densities of the Skyrme configurations for the $B = 1$ and $B = 7$ Skyrmions. We colour the density contours according to the direction the pion field at that point in space.
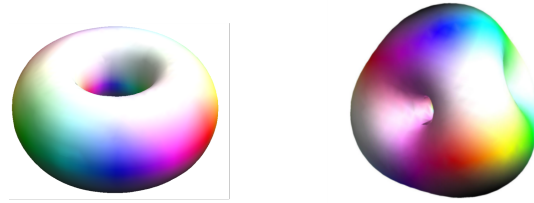


Figure 1.2: The $B = 2$ Skyrmion (left) which has toroidal symmetry and the $B = 3$ Skyrmion (right) which has tetrahedral symmetry.



Figure 1.3: The $B = 3$ Skyrmion is pulled apart into the $B = 2$ Skyrmion and the $B = 1$ Skyrmion.

to do this process. One may pull on the other four vertices instead.
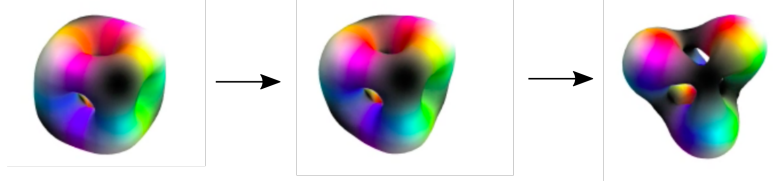


Figure 1.4: The $B = 4$ Skyrmion may be pulled apart into four $B = 1$ solutions. This shows that the cubic solution is related to standard models of the the $^4$He nucleus even though it looks radically different at first sight.

The high binding energy of the $B = 4$ cube makes it a good building block for larger Skyrmions. The $B = 8$, $B = 12$ and $B = 16$ Skyrmions can all be understood in terms of cluster configurations of the cubes. The $B = 8$ Skyrmion looks like two $B = 4$ cubes next to one another. The $B = 12$ sector has two low lying solutions. One is a triangle of clusters while the other is a chain. These are shown in Figure 1.5. As $B$ increases the configuration spaces become more complicated. The $B = 16$ sector has four known low energy Skyrmions. We discuss these in detail in Chapter 4. One may use the clusters to construct very large Skyrmions such as the cubic $B = 108$ solution discovered in [9] and even a neutron star [11]. As $B$ tends to infinity, the Skyrmions form a crystal. This looks like an infinite lattice of $B = 4$ Skyrmions [12].
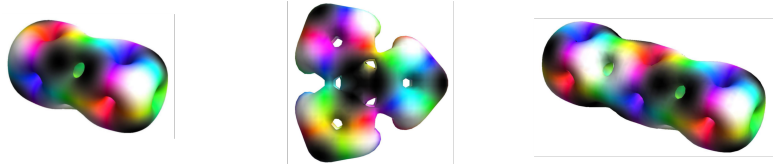


Figure 1.5: The lowest energy $B = 8$ Skyrmion (left), the $B = 12$ Skyrmion with $D_3$ symmetry (middle) and the $B = 12$ Skyrmion with $D_4$ symmetry (right). The final two are known as the triangular and chain configurations respectively.

Returning to finite $B$, the $B = 5$ and 6 Skyrmions are shown in Figure 1.6. The $B = 7$ Skyrmion has dodecahedral symmetry and hence has high classical

binding energy. This is not true of $^7$Li, which it models. We shall discover why in Chapter 3.
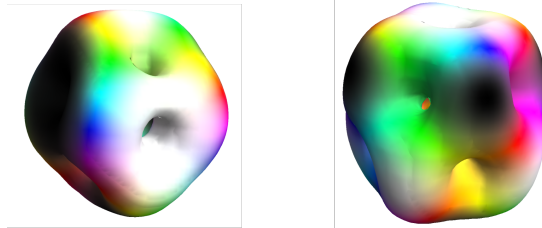


Figure 1.6: The $B = 5$ Skyrmion (left) and the $B = 6$ Skyrmion (right).

The Skyrmions in this section were all calculated using $m = 1$. When the pion mass is zero, the solutions change shape. Most significantly, the $B = 4$ cluster model breaks down. Instead of the configurations seen in Figure 1.5 the Skyrmions are shell-like in nature [13]. These configurations have large regions in their centers where sigma is approximately equal to -1. This is energetically unfavored by the pion mass term explaining the transition from shell-like solutions to cluster-like ones, as the pion mass is increased.

## 1.1.1   Modifications

The Skyrmions presented so far are solutions to the standard Skyrme model defined in (1.3). However the Lagrangian can be modified in a number of ways. The three modifications we discuss in detail all have the same aim: to decrease the classical binding energy of the Skyrmions. Real nuclei have binding energies of a few MeV per nucleon. Classical Skyrmions have a classical binding energy of around 50 MeV [14]. One could try to remedy this shortcoming by studying a modified Skyrme model which has smaller classical binding energies.

When constructing the Skyrme Lagrangian we insisted that it must respect Lorentz and chiral symmetry and have second order time derivatives. There is another pionic term one can add to the Lagrangian (1.3) with these properties. It has sixth order spatial derivatives and so is commonly called the $6^{\text{th}}$ order term, denoted $\mathcal{L}_6$. It takes the form

$$\mathcal{L}_6 \propto 2(24\pi^2)^2 \text{Tr}(B_\mu B^\mu) = \frac{3}{2}\text{Tr}\left([R_\mu, R^\nu][R_\nu, R^\lambda][R_\lambda, R^\mu]\right) . \tag{1.15}$$

The theory given by

$$\mathcal{L}_{\text{BPS}} = \mathcal{L}_6 + m\text{Tr}(1 - U)\,, \tag{1.16}$$

is BPS. Hence the energy bound (1.10) is saturated and the Skyrmions have zero classical binding energy. The solutions are invariant under volume preserving diffeomorphisms, just like a perfect fluid. To reintroduce a small binding energy, as is seen experimentally, one can study a theory close to the BPS limit such as

$$\mathcal{L} = \epsilon\mathcal{L}_2 + \mathcal{L}_6 + m_\pi Tr(1 - U)\,, \tag{1.17}$$

where $\mathcal{L}_2$ is the term with only two spatial derivatives from (1.3) and $\epsilon$ is a small parameter. This idea was put forward by Adam et al. in [15]. In theory, one begins by studying the model at $\epsilon = 0$ and finds the Skyrmions of the BPS theory. Then introducing a small $\epsilon$ should act as a small perturbation. However, in practice the solutions of the BPS theory are very complicated due to their large symmetry group. Only the $B = 1$ solution is known. Since we do not understand the initial theory, perturbing from it is hopeless. Numerical studies have been able to reach $\epsilon = 0.2$ but this is not small enough to reproduce the experimental binding energies [16].

Alternatively, the binding energy of the Skyrmions may be decreased by altering the potential term in (1.3). In [16, 17] the authors consider adding the potential

$$\text{Tr}\,(1 - U)^4 \tag{1.18}$$

to the Lagrangian. If this term dominates, the Skyrmions look like point particles taking positions on a face centred cubic lattice. This model can get close to reproducing the binding energies of real nuclei. There are many local minima in each baryon sector and ideally a quantisation scheme should include all of these solutions. This may make a thorough quantisation of the model prohibitively difficult. In addition, the Skyrme model is unique due to its conglomerate solutions where particles lose their individual identity. The point particle model does away with these unique features of the original Skyrme model.

Another idea is to couple the standard Skyrme model to vector mesons. It was shown in [18] that if one includes a certain infinite tower of mesons the model becomes BPS. The more mesons that are included, the closer to a BPS theory it becomes. The inclusion of the first meson decreases the classical binding energy of the $B = 4$ Skyrmion by a factor of four [19].

All these modifications of the standard Skyrme model are designed to decrease the classical binding energies of the Skyrmions. However, we will argue that this is unnecessary. Nuclear binding energies should be compared with *quantum* binding energies, not classical ones. By doing a more thorough quantisation of the standard Skyrme model, as laid out in the next chapter, the binding energies will naturally decrease.

## 1.2   Outline of Thesis

This thesis is concerned with quantisation of the Skyrme model. In Chapter 2 we describe rigid body quantisation, which is the most common approach. We argue that the method has several shortcomings and so we introduce a more sophisticated scheme called vibrational quantisation and show how wavefunctions are constructed in this scheme. Chapter 3 describes a vibrational quantisation of the $B = 7$ Skyrmion, which has dodecahedral symmetry. In rigid body quantisation, the $B = 7$ Skyrmion has a ground state with spin $\frac{7}{2}$. This contradicts the experimental data: Lithium-7 has a spin $\frac{3}{2}$ ground state. The calculation necessitates the careful study of a five-dimensional vibrational manifold. We calculate the rovibrational wavefunctions on this manifold in two ways. Our first method emphasises the global symmetries of the system but makes several crude approximations. In our second approach, we try to take account of several difficult features of the system such as its anharmonic potential. The ground state of the system is shown to have spin $\frac{3}{2}$, remedying the previously stated contradiction between data and the model. In Chapter 4 we describe the Oxygen-16 nucleus using a vibrational manifold inspired by Skyrme dynamics. Using this manifold we are able to construct a model which includes several low lying Skyrmions in the quantisation procedure such as the tetrahedral and flat square configurations. The inclusion of both resolves some long-standing problems in the study of Oxygen-16 such as the existence of an energy gap between the two low lying spin 2 states. We also find a spin-parity $0^-$, isospin 0 state for the first time in the Skyrme model. To further test our results, a method of calculating the electromagnetic transition rates between rovibrational states is developed and we compare our results to experimental data. Chapter 5 contains a more speculative idea. When one Skyrmion orbits another, its orbital angular momentum is in the same direction as its spin

due to the structure of the pion fields of the Skyrmions. We propose that this provides the origin of the spin-orbit force, a physically important term in the shell model. To do this, we model the Skyrmions as cogwheels and quantise the system. The conclusions of this thesis are contained in Chapter 6.

# Chapter 2

# Skyrmion quantisation

To make contact with nuclear data, one must quantise the Skyrmions. We adopt a semi-classical approach, assuming the leading order contribution to the physics is the classical information. For example, the mass of a nucleus should be well approximated by the classical mass of its corresponding Skyrmion. The first corrections come from quantising the zero modes of the Skyrmions. These are those transformations which leave the configuration's energy unchanged: translations, rotations and isorotations. We will ignore translations throughout this thesis as nuclear data is presented in the rest frame of the system. The rotation and isorotation zero modes give rise to a conserved angular momentum $J$ and isoangular momentum $I$. These give a correction to the mass formula of order $\hbar^2$. The Skyrmions can deform into composite parts, as we saw in Figure 1.3. Ideally, we would also account for these degrees of freedom in the quantisation procedure. If the deformations can be approximately described by a harmonic potential, the correction to the mass is of order $\hbar$. Finally pion-Skyrmion interactions give rise to a Casimir energy, also of order $\hbar$. Qualitatively, the quantum energy of a Skyrme configuration from these contributions is

$$ E = \mathbb{M}_B + \frac{1}{2}\hbar\left(\sum \omega\right) + \hbar\mathcal{C} + \hbar^2 E_{J,I} + O\left(\hbar^3\right) , \tag{2.1} $$

where $\omega$ represents the frequencies of the vibrational modes, $C$ represents the Casimir energy and $E_{J,I}$ represents the contribution from the rotational and isorotational zero modes. The hierarchy of these corrections comes from a semi-classical point of view. The order of importance is also supported by looking at a large $N_c$ limit of QCD. We shall now consider each of these quantum contributions in turn.

## 2.1  Zero modes

We introduce coordinates to parametrise the Skyrmion's orientation in rotational and isorotational space. Each of these spaces is a copy of $SO(3)$ and can be parametrised by Euler angles. We denote the rotational angles $(\psi, \theta, \phi)$ and the isorotational angles $(\alpha, \beta, \gamma)$. Our conventions are most easily seen pictorially as in Figure 2.1. A rotation of the Skyrmion corresponds to three composite rotations: a rotation of $\psi$ around the axis $(0, 0, 1)$ followed by a rotation of $\theta$ around $(1, 0, 0)$ and finally a rotation of $\phi$ around $(0, 0, 1)$. We denote the $3 \times 3$ rotation matrix $R^J$. The isorotation is applied to each pion vector in the same way. We denote the corresponding isorotational matrix as $R^I$. This is related to the isospin transformation (1.6) as

$$R^I = \frac{1}{2}\text{Tr}\left(\tau_i A \tau_j A^{-1}\right) . \tag{2.2}$$

With these conventions the $B = 1$ Skyrmion is invariant under the combined transformation

$$\alpha \to \alpha + a, \quad \psi \to \psi + a , \tag{2.3}$$

for any constant $a$.

Given a static Skyrme configuration $U_0(\boldsymbol{x})$, the related configurations generated by rotations and isorotations are captured by the formula

$$U_0(\boldsymbol{x}, \alpha, \beta, \gamma, \psi, \theta, \phi) = A(\alpha, \beta, \gamma)U_0\left(R^J(\psi, \theta, \phi)\boldsymbol{x}\right) A(\alpha, \beta, \gamma)^T . \tag{2.4}$$

The set of Skyrme configurations in (2.4) is called the zero mode configuration space. There is a quantisation scheme where we only include these configurations. This is called zero-mode quantisation, originally proposed for soliton models in [20] and for Skyrmion specifically in [21]. Physically, we allow the Skyrmion to rigidly rotate but not to deform or interact with the pion field that surrounds it. Hence this quantisation scheme is often called rigid body quantisation.

We quantise these modes by letting each coordinate depend on time. We then substitute (2.4) into the Lagrangian (1.3). This gives the reduced Lagrangian

$$\mathcal{L} = \mathbb{M}_B + \frac{1}{2}(\boldsymbol{a}, \boldsymbol{c}).\Lambda.(\boldsymbol{a}, \boldsymbol{c})^T , \tag{2.5}$$

where $\boldsymbol{a}$ and $\boldsymbol{c}$ are the classical isoangular and angular velocities given by

$$a_j = -i\text{Tr}\left(\tau_j A^\dagger \dot{A}\right) \text{ and } c_j = i\text{Tr}\left(\tau \dot{C} C^\dagger\right) \tag{2.6}$$
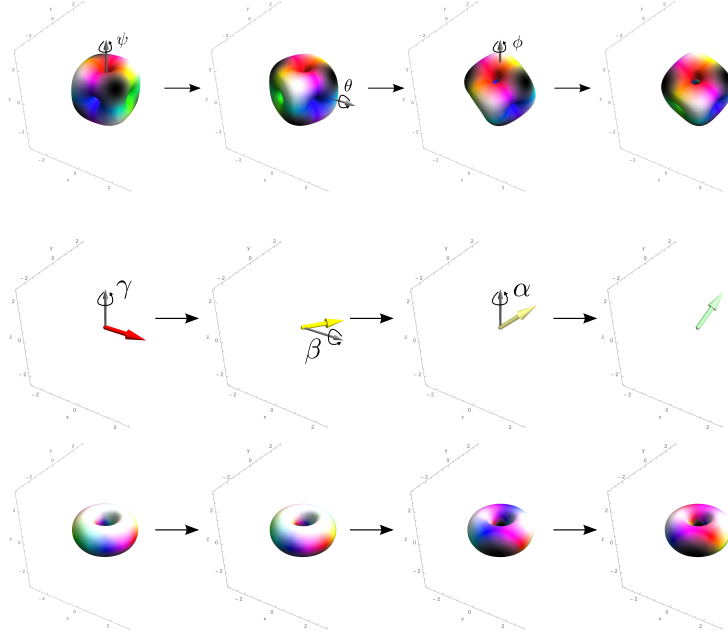
Figure 2.1: Our conventions for the Euler angles discussed in the text. Note that the rotational transformations act on the Skyrme configurations themselves and the isorotational transformations act on the pion vectors.

and $C$ is the $SU(2)$ matrix describing rotations, analogous to (2.2). $\Lambda$ is the moment of inertia tensor, it takes the form

$$\Lambda = \begin{pmatrix} U & -W \\ -W^T & V \end{pmatrix} , \tag{2.7}$$

with

$$U_{ij} = -\int \mathrm{Tr}\left(T_i T_j + \frac{1}{4}[R_k, T_i][R_k, T_j]\right) d^3x \tag{2.8}$$

$$W_{ij} = \int \epsilon_{jlm} x_l \mathrm{Tr}\left(T_i R_m + \frac{1}{4}[R_k, T_i][R_k, R_m]\right) d^3x \tag{2.9}$$

$$V_{ij} = -\int \epsilon_{ilm}\epsilon_{jnp} x_l x_n \mathrm{Tr}\left(R_m R_p + \frac{1}{4}[R_k, R_m][R_k, R_p]\right) d^3x , \tag{2.10}$$

where $T_i = \frac{i}{2}[\tau_i, U_0]U_0^{-1}$. The classical Hamiltonian is then

$$\mathcal{H} = \mathbb{M} + \frac{1}{2}\left(\boldsymbol{K}, \boldsymbol{L}\right) . \Lambda^{-1} . \left(\boldsymbol{K}, \boldsymbol{L}\right)^T , \tag{2.11}$$

15

where $\boldsymbol{K}$ and $\boldsymbol{L}$ are the classical body-fixed isoangular and angular momenta respectively. There are also space-fixed momenta which we denote $\boldsymbol{I}$ and $\boldsymbol{J}$.

The Hamiltonian (2.11) can be canonically quantised. The momenta become operators giving rise to the quantum Hamiltonian

$$\hat{\mathcal{H}} = \mathbb{M}_B + \frac{\hbar^2}{2}(\hat{\boldsymbol{K}}, \hat{\boldsymbol{L}}).\Lambda^{-1}.(\hat{\boldsymbol{K}}, \hat{\boldsymbol{L}})^T \tag{2.12}$$

$$= \mathbb{M} + \frac{\hbar^2}{2}\nabla^2 \,, \tag{2.13}$$

where $\nabla^2$ is the Laplacian on $SO(3) \times SO(3)$. The momentum operators can be written in terms of the angles defined earlier. For example the third component of the body-fixed angular momentum operator is

$$\hat{K}_3 = -i\hbar\frac{\partial}{\partial\phi} \,. \tag{2.14}$$

The space-fixed third components of the momenta, $\hat{J}_3 = -i\hbar\partial_\psi$ and $\hat{I}_3 = -i\hbar\partial_\gamma$, each commute with the Hamiltonian; as does $\hat{\boldsymbol{L}}.\hat{\boldsymbol{L}} = \hat{\boldsymbol{J}}.\hat{\boldsymbol{J}}$ and $\hat{\boldsymbol{K}}.\hat{\boldsymbol{K}} = \hat{\boldsymbol{I}}.\hat{\boldsymbol{I}}$. Hence there are four conserved quantities for each energy eigenstate, denoted $J_3$, $I_3$, $J(J+1)$ and $I(I+1)$. The third component $J_3$ takes values between $-J$ and $J$, and similar for $I_3$.

The Schrödinger equation for this Hamiltonian has been extensively studied [22]. The solutions are Wigner-D functions which are labelled by the four conserved quantities as well as the body-fixed angular momenta: $L_3$ and $K_3$. Note that while the Wigner-D functions have definite $L_3$ and $K_3$, the rigid body wavefunctions generally will not. We denote the rotational Wigner functions $D^J_{L_3,J_3}(\psi, \theta, \phi)$ and similar for the isorotational basis. Hence the solutions of the Schrödinger equation can be written

$$\Psi = \sum_{L_3,K_3} c_{L_3,K_3} D^J_{L_3,J_3}(\psi, \theta, \phi) D^I_{K_3,I_3}(\alpha, \beta, \gamma) \,, \tag{2.15}$$

which we often denote as

$$|\Psi\rangle = \sum_{L_3,K_3} c_{L_3,K_3} |J, L_3, J_3\rangle |I, K_3, I_3\rangle \,. \tag{2.16}$$

This is the wavefunction of a generalised rigid rotor and its rotational energy is given by

$$E_{\text{rot}} = -\frac{\hbar^2}{2} \langle\Psi|\nabla^2|\Psi\rangle \,. \tag{2.17}$$

16

This formula simplifies significantly if a Skyrmion has a lot of symmetry. For example, the $B = 1$ Skyrmion has rotational energy

$$\frac{\hbar^2}{4\Lambda'} \left( J(J+1) + I(I+1) \right) , \tag{2.18}$$

where $V_{ij} = U_{ij} = W_{ij} = \Lambda' \delta_{ij}$. The symmetries of the Skyrmions also give constraints on the constants $c_{L_3, K_3}$ and restrict the allowed values of $I$ and $J$. We shall now examine these constraints.

## 2.1.1 FR constraints

Single Skyrmions model nucleons, which are fermions. Hence a charge $B$ Skyrmion, being composed of $B$ nucleons, is a boson if $B$ is even and a fermion if $B$ is odd. If one applies a $2\pi$ rotation to the wavefunction (2.16), using the exponent of the rotation operator, the result should be

$$e^{2\pi i \boldsymbol{n} \cdot \hat{\boldsymbol{J}}} |\Psi\rangle = (-1)^{2B} |\Psi\rangle , \tag{2.19}$$

where $\boldsymbol{n}$ is any unit vector.

Finkelstein and Rubinstein realised solitons could be quantised as bosons or fermions consistently [23]. They first argued that, if the configurations space is not simply connected, one must look at the covering space of configurations rather than just the configuration space; in our case $SU(2) \times SU(2)$ rather than $SO(3) \times SO(3)$. The fundamental group of $SU(2) \times SU(2)$ is $\mathbb{Z}_2$ and so loops in the space are either contractible or not with these two properties forming the elements of the group $\mathbb{Z}_2$. Crucially, the union of two non-contractible loops is contractible. A $2\pi$ rotation traces out a closed loop in configuration space. We assume that if this loop is contractible, the wavefunction should transform trivially under this rotation operator. If it is not, the wavefunction should pick up a sign. Under this assumption, one can derive (2.19) [24]. The other consistent quantisation method would be to insist the wavefunction transforms trivially in both cases. This would give rise to a theory of just bosons. It has been shown that this leads to a contradiction for the Skyrme model when the field takes values in $SU(3)$ [25], but this has not yet been shown for the simpler model we are currently considering. Hence, we will simply reject this quantisation on physical grounds; we demand the $B = 1$ Skyrmion is a fermion. A similar story holds for isospin

- the wavefunction (2.16) picks up a factor $\pm 1$ (for even or odd $B$) under a $2\pi$ isorotation. These restrictions tell us that a Skyrmion with even or odd baryon number $B$ have integer or half-integer spin and isospin respectively.

Each Skyrmion has a symmetry group which is usually non-trivial. The group acts on the Skyrmion by rotation-isorotation operator pairs. Each combined transformation generates a closed path in configuration space. For consistency, the same rules as above must apply: if the path is non-contractible the wavefunction picks up a sign and if it is contractible the wavefunction transforms trivially. For example, the cubic Skyrmion is invariant under a $2\pi/3$ rotation about $(1,1,1)$ followed by a $2\pi/3$ isorotation about $(0,0,1)$. Hence the wavefunction must satisfy

$$e^{2\pi i/3^{3/2}(1,1,1)\cdot\hat{\boldsymbol{L}}}e^{2\pi i/3\hat{K}_3}\left|\psi\right\rangle = (-1)^N\left|\psi\right\rangle\ ,\tag{2.20}$$

where $N$ is equal to 0 or 1. We call $N$ the Finkelstein-Rubinstein number and relations of this form Finkelstein-Rubinstein (FR) constraints. We are left to determine $N$, which can be done in a number of ways. One is to physically pull apart the Skyrmion and keep track of how the individual Skyrmions, each a fermion, transform [27]. Another is to approximate the Skyrmion using rational maps [7]. If this can be done, Krusch developed a simple formula to find $N$ [26].

Once we find the FR constraints for all rotation-isorotation transformations which generate the symmetry group of the Skyrmion, we may calculate the allowed spin states. This tells us the spin of the ground state for a given baryon number. This is compared to real nuclear data in Table 2.1 for $B = 1,\ldots 8$. We focus on nuclei with small isospin. The model does quite well, with matches for all nuclei except $B = 5$ and $B = 7$. Note that these are the predictions for zero mode quantisation – not for the Skyrme model itself. To take any of these results seriously we must understand when rigid body quantisation is an appropriate approximation. To do this we will consider a more sophisticated scheme: vibrational quantisation.

| $B$ | Model $(J, I)$ | Exp $(J, I)$ | Nucleus | Match? |
|---|---|---|---|---|
| 1 | $\left(\frac{1}{2}, \frac{1}{2}\right)$ | $\left(\frac{1}{2}, \frac{1}{2}\right)$ | Proton / Neutron | Y |
| 2 | $(1, 0)$ | $(1, 0)$ | Deuteron | Y |
| 3 | $\left(\frac{1}{2}, \frac{1}{2}\right)$ | $\left(\frac{1}{2}, \frac{1}{2}\right)$ | $^3$H / $^3$He | Y |
| 4 | $(0, 0)$ | $(0, 0)$ | $^4$He | Y |
| 5 | $\left(\frac{1}{2}, \frac{1}{2}\right)$ | $\left(\frac{3}{2}, \frac{1}{2}\right)$ | $^5$He / $^5$Li | N |
| 6 | $(1, 0)$ | $(1, 0)$ | $^6$Li | Y |
| 7 | $\left(\frac{7}{2}, \frac{1}{2}\right)$ | $\left(\frac{3}{2}, \frac{1}{2}\right)$ | $^7$Li / $^7$Be | N |
| 8 | $(0, 0)$ | $(0, 0)$ | $^8$Be | Y |

Table 2.1: A comparison of the predicted spins of the ground state nuclei for each $B$ for zero-mode quantisation, against experimental data.

## 2.2 Vibrational modes

In zero mode quantisation we allowed the Skyrmion to rigidly rotate and isorotate. We will now also let the Skyrmion deform. To do this we must study the space of deformed Skyrme configurations. A charge $B$ Skyrmion can split into $B$ individual charge 1 Skyrmions, each of which can move and rotate. Hence the full deformation space has at least $6B$ dimensions. If the charge 1 Skyrmions are allowed to deform further, by radially expanding and contracting for example, the deformation space will have more dimensions. The zero modes are physically distinct to the deformations and hence we may try to separate the two types of transformation. We do this by defining the centred deformation space which factors out the overall translations, rotations and isorotations. We call the centred space the vibrational manifold and denote it $\mathcal{M}$. The full space can be thought of as this manifold with a fibre containing the zero modes of the Skyrme configuration, $\mathbb{R}^3 \times SO(3) \times SO(3)$, attached. The total space is a principle bundle.

To study quantum states including deformations, we must solve the Schrödinger equation on the total space. If we can put a coordinate $\boldsymbol{s}$ on $\mathcal{M}$ and find the metric $g$, the kinetic operator for small energies is known. It is the Laplace-Beltrami operator which is defined in terms of $g$ as

$$\Delta = \frac{1}{\sqrt{|g|}} \partial_i \left( \sqrt{|g|} g^{ij} \partial_j \right) , \tag{2.21}$$

where $\boldsymbol{\partial} = (\frac{\partial}{\partial \boldsymbol{s}}, \nabla)$ and $\nabla$ is the gradient on $SO(3) \times SO(3)$. The operator $\Delta$ preserves all classical symmetries of the kinetic energy after quantisation. The potential energy is the static energy of the deformed Skyrme configuration at $\boldsymbol{s}$. Hence the Schrödinger equation is

$$\left( -\frac{\hbar^2}{2} \Delta + V(\boldsymbol{s}) \right) \Psi = E\Psi \,, \tag{2.22}$$

where $\Psi$ is the total wavefunction. Despite its simple appearance this is a highly non-trivial equation: the metric is $6B$ dimensional and generically has few nice properties; there are FR constraints on $\mathcal{M}$ that the wavefunction $\Psi$ musy obey and the potential is hard to generate and anharmonic. The anharmonicity may be seen physically. Suppose we pull a $B = 3$ Skyrmion apart into $B = 1$ and $B = 2$ parts as we saw in Figure 1.3. There is little difference between the energy of the rightmost configuration in Figure 1.3 and the clusters totally separated. The authors of [32] solved (2.22) on a one-dimensional submanifold of the vibrational manifold in the $B = 2$ sector. The calculation provides a much more realistic model of the Deuteron in the Skyrme model, compared to rigid body quantisation.

To make progress solving (2.22) one must make approximations. We shall try to gain intuition about the system by assuming $\mathcal{M}$ is Euclidean. Moreover, we take the metric on the full space to be block diagonal so that the kinetic operator separates into a part which only acts via the rotational coordinates and a part which only acts via the vibrational ones. The total wavefunction is separable and takes the form

$$\Psi = \sum_i u_i(\boldsymbol{s}) \, |\Theta\rangle_i \,. \tag{2.23}$$

We call the $u_i$ vibrational wavefunctions and the $|\Theta\rangle_i$ rotational wavefunctions or spin states. The total wavefunction is known as the rovibrational wavefunction. The spin states are exactly those discussed in our analysis of rigid body quantisation. They satisfy

$$-\nabla^2 |\Theta\rangle_i = E_{J,I}(\boldsymbol{s}) \, |\Theta\rangle_i \,, \tag{2.24}$$

where $E_{J,I}$ depends on $\boldsymbol{s}$ through its dependence on the moment of inertia tensor (2.8). The vibrational wavefunctions then satisfy

$$-\frac{\hbar^2}{2} \nabla_E^2 u(s) + \left( V(s) - \frac{\hbar^2}{2} E_{J,I}(\boldsymbol{s}) \right) u(\boldsymbol{s}) = E_{\text{vib}} u(s) \,. \tag{2.25}$$

20

where $\nabla_E^2$ is the Laplacian on Euclidean space and we call $E_{\text{vib}}$ the vibrational energy.

We can solve the Schrödinger equation exactly by making two assumptions. First, that the Skyrmion's deformation does not greatly alter the moment of inertia tensor. This amounts to taking $E_{J,I}(\boldsymbol{s})$ to be constant. The dependence can be reinstated later using perturbation theory provided the deformations are small. Secondly we take $V(s)$ to be harmonic around its minimum (wlog at $\boldsymbol{s} = \boldsymbol{0}$), the minimal energy Skyrmion. Note that these assumptions are justified when deformations of the Skyrmion are small which is true near the origin of $\mathcal{M}$. Low energy states are concentrated near here, and so our analysis may be valid for low energy states of the system.

The deformations near the Skyrmion at $\boldsymbol{s} = \boldsymbol{0}$ may be classified by the irreducible representations (irreps) of the Skyrmion's symmetry group which we denote $\mathcal{G}_0$. Now $\mathcal{M}$ can be written as a product space, the constitute submanifolds labelled by the irreducible representations of $\mathcal{G}_0$. We may solve the Schrödinger equation on each submanifold and then combine the solutions. The harmonic potential can have different frequencies in each submanifold. The ground state vibrational wavefunction $u_0(\boldsymbol{s})$ is the ground state harmonic oscillator wavefunction with energy

$$\sum_{A=\text{reps}} \left( \sum_{i=1}^{\dim \text{ of } A} \frac{1}{2} \hbar \omega^A \right) , \tag{2.26}$$

where $\omega^A$ is the frequency of the potential in the submanifold labelled by the irrep $A$. The ground state is isotropic in $\mathcal{M}$ and concentrated around $\boldsymbol{s} = \boldsymbol{0}$. The rovibrational wavefunction

$$|\Psi\rangle = u_0(\boldsymbol{s}) |\Theta\rangle , \tag{2.27}$$

is non-zero everywhere on $\mathcal{M}$. Some FR constraints still apply at all points on $\mathcal{M}$, although they change depending on the symmetry of the Skyrme configuration at $\boldsymbol{s}$. In this case, the spin state $|\Theta\rangle$ must be allowed everywhere on $\mathcal{M}$ for (2.27) to be consistent with the FR constraints since $u_0(\boldsymbol{s})$ is non-zero everywhere on $\mathcal{M}$. This happens if $|\Theta\rangle$ is consistent with the FR constraints of the Skyrmion at $\boldsymbol{s} = \boldsymbol{0}$ and if this configuration is the maximally symmetric configuration on $\mathcal{M}$. This is true if the symmetry group of the vibrational manifold is the same as the symmetry group of the Skyrmion. Physically, this assumes that when the

Skyrmion breaks apart, the deformed configurations will all have less symmetry than the Skyrmion. Overall, the wavefunction (2.27) is concentrated around the Skyrmion at $s = 0$ and has the same spin state as found in rigid body quantisation – the one allowed by the Skyrmion. Hence the wavefunction (2.27) is analogous to a rigid body wavefunction. In fact one can recover the rigid body scheme by taking $\omega \to \infty$. This freezes out excited modes, leaving just the ground state (2.27). In this limit the vibrational wavefunction becomes a delta function on $\mathcal{M}$.

Note that since the vibrational wavefunction $u_0$ is isotropic, it transforms trivially under any element of the symmetry group of $\mathcal{M}$. In (2.27), this wavefunction is combined with a spin state which transforms simply under the symmetry group of the Skyrmion: trivially if the element has a positive FR number and it picks up a sign if the element has a negative FR number. This suggests there is a relationship between the representations of vibrational wavefunctions, spin states and the allowed rovibrational wavefunctions. We now formalise this relationship.

Suppose the vibrational manifold $\mathcal{M}$ and the Skyrmion have the same symmetry group, $\mathcal{G}_0$. There are three representations of this group which we shall use. They are

- $\boldsymbol{\rho}^{\text{FR}}$ : This is the Finkelstein-Rubinstein representation. An element is equal to $+1$ or $-1$ if the Finkelstein-Rubinstein number $N$, defined in (2.20), is equal to 0 and 1 respectively.

- $\boldsymbol{\rho}_R^{\text{FR}}$ : For a given spin/isospin pair $(J, I)$ the usual basis of spin/isospin states is

$$(|J, J\rangle \otimes |I, I\rangle, |J, J\rangle \otimes |I, I-1\rangle, \ldots |J, -J\rangle \otimes |I, -I\rangle) . \tag{2.28}$$

Now consider an element $g \in \mathcal{G}_0$ which corresponds to a rotation of $\theta_1$ around the axis $\boldsymbol{n}_1$ followed by an isorotation of $\theta_2$ around the axis $\boldsymbol{n}_2$. This acts on the basis (2.28) as the matrix

$$M_R^{\text{FR}}(g) = e^{i\theta_1 \boldsymbol{n}_1 \cdot \hat{\boldsymbol{L}}} e^{i\theta_2 \boldsymbol{n}_2 \cdot \hat{\boldsymbol{K}}} . \tag{2.29}$$

Note that the dimension of this matrix depends on the values of $J$ and $I$. We can always reduce this representation into

$$\boldsymbol{\rho}_R^{\text{FR}} = \boldsymbol{\rho}^{\text{FR}} \otimes \boldsymbol{\rho}^R . \tag{2.30}$$

22

The matrix $M_R(g)$ is then equal to

$$M_R(g) = (-1)^N M_R^{\text{FR}}(g) \,. \tag{2.31}$$

- $\boldsymbol{\rho}_v$ : Suppose we find a degenerate set of vibrational wavefunctions $\{u_i\}$ and define the vector $\boldsymbol{u} = (u_1, \ldots u_n)$. Under an element of the symmetry group $g \in \mathcal{M} \simeq \mathcal{G}_0$ these transform into each other as

$$\boldsymbol{u} \to M_v(g)\boldsymbol{u} \,. \tag{2.32}$$

This defines the representation of the vibrational wavefunctions.

Suppose there is a basis of vibrational wavefunctions with representation $\boldsymbol{\rho}_v$ and a basis of spin states with representation $\boldsymbol{\rho}_R$. If $\boldsymbol{\rho}_v$ and $\boldsymbol{\rho}_R$ are isomorphic we can find a rovibrational wavefunction that transforms trivially under the combined rotational-vibrational action. This will satisfy the FR constraints at all points in $\mathcal{M}$. For example, at the origin of $\mathcal{M}$, all the vibrational wavefunctions are equal. Hence the vibrational action is trivial. So, if the combined action is trivial then so is the operator corresponding to $M_R$. Hence, at the origin of $\boldsymbol{s}$, the rovibrational wavefunction transforms as

$$|\Psi\rangle \to M_R^{FR} |\Psi\rangle = (-1)^N |\Psi\rangle \,, \tag{2.33}$$

as required.

In practice, knowing that a basis of spin states and vibrational wavefunctions will combine to create a valid rovibrational state does not help construct the state itself. For example, rather than finding a special subset of spin states which transform exactly as required, it is often practical to use the basis (2.28). We shall now show how to construct such states. Suppose there is a basis of vibrational wavefunctions and a basis of spin states which transform as (2.30) and (2.32) respectively. We can construct a rovibrational wavefunction of the form

$$|\Psi\rangle = \sum_i a_{ij} u_i |\Theta\rangle_j \,. \tag{2.34}$$

To be a valid rovibrational wavefunction, this should transform trivially under the combined rotational-vibrational action of each element which leaves $\mathcal{M}$ unchanged. This means that

$$|\Psi\rangle = \sum_i a_{ij} u_i |\Theta\rangle_j \to \sum_i a_{ij} M_R(g)_{ik} u_k M_v^{-1}(g)_{jl} |\Theta\rangle_l = |\Psi\rangle \,, \tag{2.35}$$

which leads to an equation for the coefficients

$$\left(M_R(g)_{ik} M_v^{-1}(g)_{jl} - \delta_{ik}\delta_{jl}\right) a_{ij} = 0 \,, \tag{2.36}$$

for each element of the group $g \in \mathcal{G}_0$. This can be turned into a nullspace problem by defining $(\boldsymbol{a}_i)_j = a_{ij}$ and $\boldsymbol{b} = (\boldsymbol{a}_1, \boldsymbol{a}_2, \ldots \boldsymbol{a}_n)$. The vector $\boldsymbol{b}$ is then the zero eigenvector of a matrix, which can be derived from (2.36). There is one of these constraints for each element of the symmetry group.

For a simple example, consider the $B = 3$ Skyrmion with tetrahedral symmetry as seen in Figure 1.2. The tetrahedral group has two generating elements: $g_3$ and $g_2$ which correspond to a $C_3$ symmetry and a $C_2$ symmetry respectively. For spin $\frac{1}{2}$, isospin $\frac{1}{2}$ the spin state basis is four dimensional. If the Skyrmion is orientated with a vertex which points in the $(1, 1, 1)$ direction and the Skyrmion has white on the center of its top edge, the spin states transform into each other as

$$M_R(g_3) = \frac{1}{2} \begin{pmatrix} i & i & i & i \\ -1 & 1 & -1 & 1 \\ -1 & -1 & 1 & 1 \\ -i & i & i & -i \end{pmatrix} \text{ and } M_R(g_2) = \begin{pmatrix} -1 & 0 & 0 & 0 \\ 0 & 1 & 0 & 0 \\ 0 & 0 & 1 & 0 \\ 0 & 0 & 0 & -1 \end{pmatrix}. \tag{2.37}$$

The ground state vibrational wavefunction $u_0$ is the isotropic harmonic oscillator and so this transforms trivially. Hence, this wavefunction has $M_v = 1$ for each of these symmetry elements. So in this case the coefficients $a_{ij}$ with $i = 1$, $j = 1, .., 4$ are simply the common eigenvalue one eigenvectors of the matrices displayed in (2.37). There is only one such vector, which is proportional to

$$(0, 1, -1, 0) \,. \tag{2.38}$$

This means that there is exactly one rovibrational wavefunction which can be constructed using the ground state vibrational wavefunction and has spin $\frac{1}{2}$ and isospin $\frac{1}{2}$. It is

$$u_0(\boldsymbol{s}) \left( \left| \frac{1}{2}, \frac{1}{2} \right\rangle \left| \frac{1}{2}, -\frac{1}{2} \right\rangle - \left| \frac{1}{2}, -\frac{1}{2} \right\rangle \left| \frac{1}{2}, \frac{1}{2} \right\rangle \right) \,. \tag{2.39}$$

This obeys the FR constraints on the full vibrational manifold, provided the manifold has at most tetrahedral symmetry.

The explicit construction of excited states is more complicated, but we can calculate which spins are allowed rather easily. For a given symmetry group $\mathcal{G}_0$, spin-isospin pair $(J, I)$ and set of vibrational wavefunctions $\{u_i\}$, one should find the representations $\boldsymbol{\rho}_R$ and $\boldsymbol{\rho}_v$. These can be decomposed in terms of their irreps and compared. If the two share any irreps, they may be combined to form a valid rovibrational wavefunction. We shall see multiple examples throughout this thesis. Note that rigid body quantisation is equivalent to only allowing vibrational wavefunctions which transform trivially under all elements of $\mathcal{G}_0$: precisely the ground states of the vibrational problem. Excited states do not have this restriction and so vibrational quantisation allows many more spin and isospin combinations than rigid body quantisation.

The binding energy of a vibrationally quantised Skyrmion is significantly different than if we used rigid body quantisation. Suppose we use a scheme where the Skyrmion is allowed to break into its consistory $B = 1$ parts. This requires $6B - 9$ vibrational modes and hence the energy of the Skyrmion, in a harmonic approximation, is

$$E_B = \mathbb{M}_B + \frac{1}{2}\hbar\bar{\omega}(6B - 9) + \frac{\hbar^2}{2}E_{J,I}\,, \tag{2.40}$$

where $\bar{\omega}$ is some appropriately averaged frequency. The expression is to be compared to the energy of $B$ single nucleons which is

$$BE_1 = B\mathbb{M}_1 + B\frac{3\hbar^2}{8\Lambda'}\,. \tag{2.41}$$

Note that there is no vibrational energy for a $B = 1$ Skyrmion since it cannot be broken down any further. Hence, the binding energy of a Skyrmion with charge $B$ in the vibrational quantisation scheme is $\frac{1}{2}\hbar\bar{\omega}(6B - 9)$ smaller than it would be in the rigid body scheme. So, taking account of vibrational modes naturally reduces the binding energy, bringing the Skyrme model closer to real nuclear data.

We have shown the link between rigid body quantisation and vibrational quantisation. We now focus on their differences which are most apparent when the symmetry groups of the Skyrmion and $\mathcal{M}$ are not equal. In these cases, the vibrational picture shows when rigid body quantisation is inappropriate.

**Approximate symmetry**

Suppose there is a Skyrmion with an approximate symmetry at $s = 0$ and that the symmetry becomes exact at $s^*$, nearby on $\mathcal{M}$. Here, we imagine that the Skyrme configuration at $s^*$ is not necessarily a local minimum of the system. Now let $|\Theta\rangle$ be a rotational state allowed by the Skyrmion at $s = 0$ but not at $s^*$. If one were to rigidly quantise the Skyrmion, the analogous rovibrational state would be

$$\Psi = u_0(s) |\Theta\rangle \ . \tag{2.42}$$

However, $\Psi(s^*)$ is non-zero and hence the FR constraints at $s^*$ are not satisfied. This is a contradiction and so the wavefunction (2.42) is not a valid state. If $|\Theta\rangle$ was allowed at $s^*$ there would be no contradiction. We deduce that to apply rigid body quantisation to a configuration with approximate symmetry, one should actually use the FR constraints that arise from the exact symmetry. By this argument, applying rigid body quantisation to modestly deformed Skyrmions, as in [14], is invalid.

This analysis is important for quantisation of rotationally deformed Skyrmions. When a Skyrmion acquires spin it naturally deforms. This affects the symmetries of the solution as has been studied in [29]. The deformations are small for physically reasonable spins. Our analysis shows that these small deformations will not greatly affect the allowed quantum states of the static solution.

**Enhanced symmetry**

On occasion, a vibrational manifold will contain Skyrme configurations with a symmetry group not contained in $\mathcal{G}_0$. This happens for the $B = 3$ Skyrmion. The vibrational manifold contains the mode shown in Figure 2.2, first discovered in [28]. This mode contains the $B = 3$ torus which has a continuous symmetry not shared by the tetrahedron. We say this point has *enhanced symmetry*. The rovibrational wavefunctions must respect the symmetries of this configuration which bring additional FR constraints into the problem. In the $B = 3$ case, the tetrahedron allows for a spin $\frac{1}{2}$, isospin $\frac{1}{2}$ state but this is not allowed at the torus. Hence, the rovibrational state with $J = I = \frac{1}{2}$ must vanish there. The torus is far away from the tetrahedron in configuration space and has high energy. Hence the total wavefunction will already be small at this point and the existence of the torus will

not greatly alter the energies of the wavefunction. In other cases, the effect will be large. We shall study such a case in the $B = 16$ sector during Chapter 3.
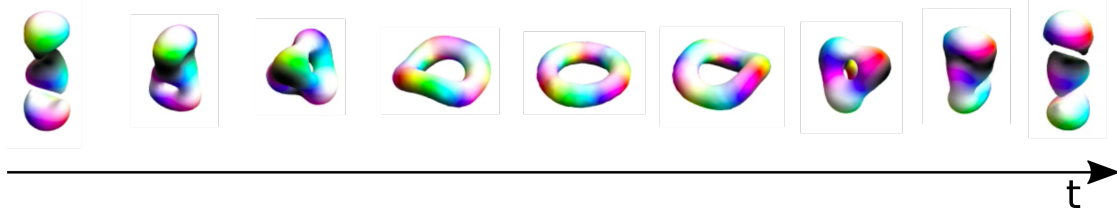


Figure 2.2: Two $B = 1$ Skyrmions are symmetrically shot towards a third lying between them. The three form a tetrahedron then continue on to form a $B = 3$ torus. They emerge from the torus forming the dual tetrahedron before going off to infinity having regained their original, spherical form.

In [30] it was proposed to quantise the two Skyrmions of the $B = 12$ sector (the triangle and chain, as seen in Figure 1.5) separately, using RB quantisation for each. Thinking of vibrational quantisation, we know that this is only appropriate if the configurations are far apart in $\mathcal{M}$. If this were the case, the two vibrational wavefunctions would have little overlap and be approximately orthogonal. We shall not comment on whether the triangular and chain configurations are far apart in $\mathcal{M}$; just point out that one must show that they are to have confidence in the calculation of [30].

By considering vibrational quantisation we have discovered some rules of thumb for rigid body quantisation. These are:

- If a Skyrmion has an approximate symmetry, one should quantise as if the Skyrmion actually has the exact symmetry.

- Rigid body quantisation of a Skyrmion is inappropriate if its vibrational manifold contains another configuration with enhanced symmetry. The effect is more important if the enhanced configuration is nearby the Skyrmion in $\mathcal{M}$ and has low energy.

- If Skyrmions are far apart in $\mathcal{M}$, one may apply rigid body quantisation separately to each configuration.

Table 2.1 contains the results of rigid body quantisation compared to nuclear data. The two troubling results were for $B = 5$ and $B = 7$. The $B = 5$ Skyrmion has $D_{2d}$ symmetry. However, there are other low energy Skyrme configurations with enhanced symmetry as discussed in [14]. Perhaps a vibrational quantisation including these configurations would alter the results. The $B = 7$ is a rather special Skyrmion due to its large symmetry group. To resolve the incorrect ground state spin, one must calculate the vibrational wavefunctions carefully. We shall do this in Chapter 3.

## 2.3 Casimir energy

Casimir energy takes account of vacuum fluctuations around the Skyrmion. This is practically and theoretically difficult as the calculation of Casimir energy necessitates renormalisation of the Skyrme model - a non-renormalisable theory. One must assume that counter terms are small. These difficulties mean that only a limited amount of work has been done on Casimir energy calculations. In the $B = 1$ sector the authors of [31] found the mass correction to the $B = 1$ Skyrmion to be around 50% of its classical value. Hence the Casimir contribution is clearly large. We are mostly interested in energy spectra – specifically the ordering of states and the gaps between them. We shall assume that the Casimir energy contributes the same zero-point energy to each state in a given baryon sector. With this assumption, we can compare the energy of states we find, but do not trust their total energies.

## 2.4 Summary

In this chapter, we described quantisation of the Skyrme model and saw that rigid body quantisation leads to results in conflict with nuclear data. Specifically, it predicts an incorrect spin for the $^5$He and $^7$Li ground states. We argue that vibrational quantisation may resolve these problems as well as lowering the binding energy of the Skyrmions, another issue of the model. We will consider vibrational quantisation of the $B = 7$ Skyrmion in the next chapter. The $B = 5$ Skyrmion should be looked at in future work to see if our suggestion works out in detail.

In addition, we argued that rigid body quantisation is inappropriate when the vibrational manifold contains a low energy Skyrme configuration with enhanced symmetry. To find such configurations, a careful study of the vibrational manifold is required. Hence, these spaces should be carefully studied in future work.

# Chapter 3

# Vibrational quantisation of the $B = 7$ Skyrmion

*This chapter is an extension of the work in the single author paper [33].*

Rigid body quantisation of the $B = 7$ Skyrmion predicts a spin $\frac{7}{2}$ ground state for the $^7\mathrm{Be}/^7\mathrm{Li}$ isodoublet. The dodecahedral symmetry of the $B = 7$ Skyrmion rules out low energy states with spin $\frac{1}{2}$, $\frac{3}{2}$ and $\frac{5}{2}$. In reality, experimental data show that all these states exist and the ground state has spin $\frac{3}{2}$. The first excited state of $^7\mathrm{Li}$ has spin $\frac{1}{2}$ and lies 0.5 MeV above the ground state while the spin $\frac{7}{2}$ state is the second excited state lying 4.6 MeV above. In this chapter we shall see that the inclusion of vibrational modes in the quantisation procedure resolves this problem.

The $^7\mathrm{Li}$ and $^7\mathrm{Be}$ nuclei are special. Among all nuclei with $B < 30$ they are the only ones that have an observed spin $\frac{7}{2}$ state lying below the lowest spin $\frac{5}{2}$ state. The $B = 7$ Skyrmion is also special. It has the largest finite symmetry group of any known Skyrmion with non-zero pion mass. We shall see that this large symmetry group is the reason why the spin $\frac{7}{2}$ state has abnormally low energy.

The $^7\mathrm{Li}$ nucleus is usually described using a cluster model [34] which asserts that the nucleus is made of two interacting clusters. These are an alpha particle and a tritium nucleus. This model successfully reproduces the energy spectrum and some electrostatic properties of the nucleus. We shall see that the inclusion of vibrational modes in Skyrmion quantisation highlights a connection between the

Skyrme model and the ideas of clustering.

This chapter is organised as follows. In Section 3.1 we study the structure of the $B = 7$ Skyrmion and one of its vibrational manifolds. We discuss how one should include vibrations in the quantisation procedure and the effects of the Finkelstein-Rubinstein constraints in Section 3.2. Here, we consider the quantisation in two different schemes, one focusing on the global structure of vibrational space and one focusing on some complications of the real model such as the anharmonic potential. We then compare the results of our quantisation with nuclear data before concluding and discussing further work in Section 3.3.

## 3.1    A vibrational manifold of the $B = 7$ Skyrmion

The $B = 7$ Skyrmion has dodecahedral symmetry as seen in Figure 3.1. There is $D_5$ symmetry around each face of the Skyrmion and $D_3$ symmetry around each vertex. These, alongside the additional reflection symmetry, generate the full symmetry group of the Skyrmion $Y_h$.

The vibrational modes around the Skyrmion were numerically generated and studied in [35] by considering small perturbations around the $B = 7$ Skyrmion. Two low frequency modes were found, one of which had a clear physical interpretation and a clean peak in the power spectrum. We will assume that this is the lowest energy vibrational mode and exclude all others from our analysis. This mode generates a vibrational manifold of Skyrme configurations with each point in the manifold corresponding to a specific deformed Skyrme configuration. Our aim is to understand the structure of the manifold and to find subspaces where the Skyrme configurations have some symmetry.
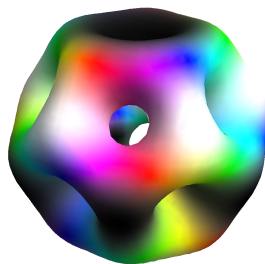


Figure 3.1: A surface of constant baryon density for the $B = 7$ Skyrmion.

The vibrational mode we consider has five fold degeneracy and so generates a 5-dimensional vibrational manifold which we denote $\mathcal{V}_5$. Each point $\boldsymbol{v} \in \mathcal{V}_5$ corresponds to a quadrupole deformation tensor of the Skyrmion, $Q(\boldsymbol{v})$. There is a natural mapping from a hyperplane in $\mathbb{R}^6$ (isomorphic to $\mathcal{V}_5$) to the space of quadrupole tensors. It is

$$(v_1, v_2, v_3, v_4, v_5, v_6) \mapsto \begin{pmatrix} v_1 & 2^{-\frac{1}{2}} v_6 & 2^{-\frac{1}{2}} v_5 \\ 2^{-\frac{1}{2}} v_6 & v_2 & 2^{-\frac{1}{2}} v_4 \\ 2^{-\frac{1}{2}} v_5 & 2^{-\frac{1}{2}} v_4 & v_3 \end{pmatrix}, \qquad (3.1)$$

where $\boldsymbol{v}$ satisfies $(1, 1, 1, 0, 0, 0) \cdot \boldsymbol{v} = 0$ to ensure the quadrupole tensor is traceless. We can add vectors on the hyperplane; this is equivalent to adding the quadrupole tensors in $\mathbb{R}^3$. We choose the normalisation so that a unit vector $\hat{\boldsymbol{v}}$ maps to a quadrupole which satisfies $Q_{ij} Q_{ij} = 1$. Each quadrupole tensor, $Q(\boldsymbol{v})$, has an associated symmetry group which acts on $\mathbb{R}^3$. Any symmetry shared by the quadrupole tensor and the $B = 7$ Skyrmion is a symmetry of the Skyrme configuration at the point $\boldsymbol{v}$.

In [35] it was found that the vibration we consider preserves the Skyrmion's $D_5$ symmetry along certain lines in $\mathcal{V}_5$. Physically, this vibration pulls on two opposite faces of the dodecahedron and breaks the Skyrmion into three clusters: a $B = 3$ torus sandwiched between two $B = 2$ tori. This can happen in six ways as there are six pairs of faces on the Skyrmion. Hence there are six special lines in $\mathcal{V}_5$ which preserve $D_5$ symmetry. They are evenly spaced and are aligned with the vertices of a regular 5-simplex. We must position the 5-simplex in $\mathcal{V}_5$ so that each vertex, $\boldsymbol{v}_a$, maps to a quadrupole tensor which is circle invariant around the axis passing through the Skyrmion faces that are being pulled upon. This ensures that the Skyrme configuration at $\boldsymbol{v}_a$ preserves $D_5$ symmetry. We use the Veronese mapping to help us. This is a map from $\mathbb{R}P^2$ to a 2-dimensional subspace of $\mathcal{V}_5$. Explicitly it takes

$$(x_1, x_2, x_3) \mapsto \left( x_1^2 - \frac{1}{3} r^2, x_2^2 - \frac{1}{3} r^2, x_3^2 - \frac{1}{3} r^2, x_2 x_3, x_1 x_3, x_1 x_2 \right). \qquad (3.2)$$

This then maps to a quadrupole via (3.1) which is circle invariant around $(x_1, x_2, x_3)$. For example, the Skyrmion has $D_5$ symmetry around the axis $\boldsymbol{x}_1 = (0, 0, 1)$. This goes, via the Veronese mapping, to the 6-vector

$$\boldsymbol{v}_1 = (-6^{-\frac{1}{2}}, -6^{-\frac{1}{2}}, (2/3)^{\frac{1}{2}}, 0, 0, 0) \qquad (3.3)$$
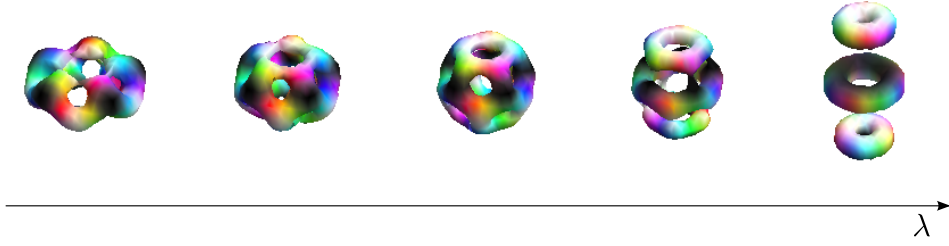
Figure 3.2: A vibration in $\mathcal{V}_5$ which preserves $D_5$ symmetry. The parameter $\lambda$ measures the amplitude of the vibration. This figure was generated using the gradient flow approximation to dynamics. The minimum energy Skyrmion is at $\lambda = 0$. This deforms into a ring-like configuration for $\lambda < 0$ and three clusters for $\lambda > 0$.

which maps to the quadrupole

$$Q_1 = \begin{pmatrix} -6^{-\frac{1}{2}} & 0 & 0 \\ 0 & -6^{-\frac{1}{2}} & 0 \\ 0 & 0 & (2/3)^{\frac{1}{2}} \end{pmatrix}. \tag{3.4}$$

This is circle invariant around $\boldsymbol{x}_1$ as desired. Repeating this process, we may generate the vertices of the 5-simplex in $\mathcal{V}_5$ from the lines which pass through the faces of the dodecahedron. This procedure has the corollary that all six vertices of the 5-simplex lie on the 2-dimensional Veronese surface. We denote the 5-simplex vertices as $\boldsymbol{v}_a \in \mathcal{V}_5$ and the corresponding quadrupole tensors $Q_a$; these are circle invariant around $\boldsymbol{x}_a$. Any configuration which lies on the line $\lambda \boldsymbol{v}_a \in \mathcal{V}_5$, $\lambda \in \mathbb{R}$ has $D_5$ symmetry. The parameter $\lambda$ is the amplitude of the vibration. For $\lambda > 0$ the Skyrmion deforms as described above: a pair of opposite faces are pulled upon. When $\lambda < 0$ the faces are pushed together and the Skyrmion flattens out. The full vibration is displayed in Figure 3.2.

We may use the geometry of the 5-simplex to find additional symmetric subspaces in $\mathcal{V}_5$. The planes passing through an edge of the simplex can be written as

$$\mu \boldsymbol{v}_a + \nu \boldsymbol{v}_b, \tag{3.5}$$

where $a \neq b$ and $\mu, \nu \in \mathbb{R}$. The corresponding quadrupole has a $C_2$ symmetry, shared with the $B = 7$ Skyrmion, about the axis $\boldsymbol{x}_a \times \boldsymbol{x}_b$. This is enhanced to a

33

$D_2$ symmetry when $\mu = \nu$.

The 5-simplex has 20 triangular faces. A line passing through the centre of a face takes the form

$$\lambda(\boldsymbol{v}_a + \boldsymbol{v}_b + \boldsymbol{v}_c),\tag{3.6}$$

where $a \neq b \neq c$. In fact, this line passes through two vertices of the dodecahedron which are dual to each other. Thus there are only ten distinct lines. The quadrupole tensor derived from (3.6) has only two distinct eigenvalues. Thus it is circle invariant around the eigenvector of the non-degenerate eigenvalue. This eigenvector passes through a vertex of the $B = 7$ Skyrmion which has $D_3$ symmetry. Thus the Skyrme configurations on these 10 lines in $\mathcal{V}_5$ retain $D_3$ symmetry. Note that, since these quadrupoles are circle invariant, these points in $\mathcal{V}_5$ also lie on the Veronese surface discussed earlier. It is instructive to view the physical picture. When $\lambda > 0$ the three component quadrupole tensors pull on three pairs of opposite faces. Three faces always surround a vertex of the Skyrmion, as do the opposite faces; the remaining three pairs form a ring around its centre. The quadrupole tensors around the vertex sum to give a quadrupole which pulls in the direction of the surrounded vertex. This is seen in Figure 3.3. When large, this vibration breaks the Skyrmion into two $B = 3$ Skyrmions sandwiching a $B = 1$ Skyrmion. When $\lambda < 0$ the faces surrounding the vertex are pushed upon and the $B = 7$ Skyrmion breaks into 7 individual $B = 1$ Skyrmions.

The analysis so far is based on small perturbations around the Skyrmion. We believe that there will be a bifurcation where the exact symmetries discussed above will break. For example, the $D_3$ symmetry will break to a $C_3$ symmetry. This allows the asymptotic configuration in $\mathcal{V}_5$ to be a two-cluster system consisting of a $B = 3$ and $B = 4$ Skyrmion. This has lower energy than the three-cluster system described in the previous paragraph. These are hard to distinguish near the origin of $\mathcal{V}_5$ and so the difference will not be apparent in our analysis. Thus we shall assume that the Skyrme configuration along this vibration, at large amplitudes, will be the $C_3$ symmetric $3 + 4$ cluster configuration instead of the $D_3$ symmetric $3 + 1 + 3$ configuration. The entire vibration is displayed in Figure 3.4.
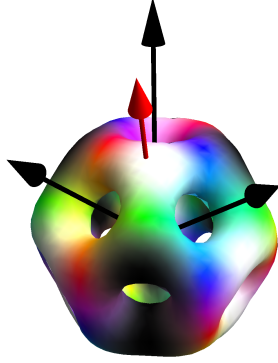
Figure 3.3: When three faces of the Skyrmion are pulled equally, a $D_3$ symmetry remains. The sum of the quadrupoles which pull on the faces of the Skyrmion give a quadrupole which is circle invariant about the red axis which passes through a vertex as shown.
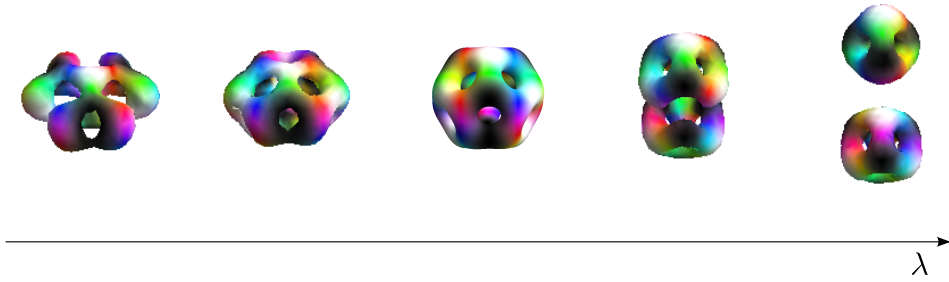


Figure 3.4: A vibration in $\mathcal{V}_5$ which preserves $C_3$ symmetry. The parameter $\lambda$ measures the amplitude of the vibration. The minimum energy Skyrmion is at $\lambda = 0$. This deforms into seven individual distorted Skyrmions for $\lambda < 0$ and two clusters for $\lambda > 0$.

## 3.2 Quantisation on the vibrational manifold

Our aim is to quantise the $B = 7$ Skyrmion taking the lowest energy vibrational mode into account. The vibrational manifold we quantise on is $\mathcal{V}_5$ which has a fibre at each point containing the rotations and isorotations. We can think of the full space as a family of Skyrme configurations parametrised by vibrational ($\boldsymbol{v}$), rotational ($\phi, \theta, \psi$) and isorotational ($\alpha, \beta, \gamma$) coordinates. The angular coordinates are two sets of Euler angles defined in Chapter 2. To quantise we promote all

these parameters, including $\boldsymbol{v}$, to dynamical degrees of freedom by allowing them to depend on time. The kinetic energy can be written in terms of the angular and isoangular velocities defined in (2.6) and the vibrational velocity as

$$T = \frac{1}{2}(\dot{\boldsymbol{v}}, \boldsymbol{a}, \boldsymbol{c}).g(\boldsymbol{v}).(\dot{\boldsymbol{v}}, \boldsymbol{a}, \boldsymbol{c})^T , \qquad (3.7)$$

where $g(\boldsymbol{v})$ is the metric on the full space, which depends on the Skyrme configuration at $\boldsymbol{v} \in \mathcal{V}_5$.

With the kinetic energy written in this way, the quantum kinetic operator is

$$-\frac{\hbar^2}{2}\Delta = -\frac{\hbar^2}{2}\frac{1}{\sqrt{|g|}}\partial_i \left( \sqrt{|g|}g^{ij}\partial_j \right) , \qquad (3.8)$$

where $|g|$ is the determinant of the metric. This preserves the classical symmetries of the kinetic energy after quantisation.

The potential energy, $V(\boldsymbol{v})$, is the mass (1.7) of the configuration at $\boldsymbol{v}$. The Hamiltonian is

$$\mathcal{H} = -\frac{\hbar^2}{2}\Delta + V(\boldsymbol{v}) . \qquad (3.9)$$

To find bound states of definite energy we solve the stationary Schrödinger equation arising from this Hamiltonian,

$$\mathcal{H}\Psi = E\Psi . \qquad (3.10)$$

The FR constraints on $\Psi$ can be written in terms of the classical symmetries of the Skyrmion. For example, the $B = 7$ Skyrmion is invariant under a $2\pi/5$ rotation around the 3-axis followed by a $-4\pi/5$ isorotation around the 3-axis in isospace. In operator form, this $C_5$ symmetry puts the following constraint on the wavefunction

$$e^{\frac{2\pi i}{5}\hat{L}_3}e^{-\frac{4\pi i}{5}\hat{K}_3}\Psi = -\Psi , \qquad (3.11)$$

where $\hat{L}_3$ and $\hat{K}_3$ are the body fixed angular momentum operators defined earlier. Similarly, the $C_3$ symmetry gives the constraint

$$e^{2\pi i/3\,\boldsymbol{n}_1\cdot\hat{\boldsymbol{L}}}e^{i\xi\,\boldsymbol{n}_2\cdot\hat{\boldsymbol{K}}}\Psi = \Psi . \qquad (3.12)$$

where $\boldsymbol{n}_1 = (-\sqrt{\frac{2}{15}(5 - \sqrt{5})}, 0, \sqrt{\frac{1}{15}(5 + 2\sqrt{5})})$ is a vector which passes through one of the dodecahedron's vertices while $\xi$ and $\boldsymbol{n}_2$ define the isorotation required to

36

return the Skyrmion to its original colouring. The FR numbers can be calculated using the rational map ansatz [7] as set out in [26].

The constraints (3.11) and (3.12) both apply when the Skyrmion has dodecahedral symmetry. This occurs at the origin of $\mathcal{V}_5$. For a generic point $\boldsymbol{v}$ there is no symmetry and thus no constraints. In the previous section we found lines in $\mathcal{V}_5$ which had some symmetry. One set of these preserved $D_5$ symmetry. Thus, on these lines, only a constraint such as (3.11) applies, as well as an additional constraint which enhances the $C_5$ symmetry to $D_5$. Another set of lines preserved $C_3$ symmetry, meaning the wavefunction must satisfy a constraint such as (3.12) on these.

Now the problem is formulated. To include the lowest vibrational mode when studying the states of $^7\text{Li}/^7\text{Be}$ we must solve (3.10), an 11-dimensional Schrödinger equation, subject to (3.11) and (3.12) at $\boldsymbol{s} = 0$, just a constraint such as (3.11) on six lines in the vibrational space (representing the $D_5$ preserving directions in $\mathcal{V}_5$) and a constraint such as (3.12) on ten lines. There are further constraints on the edges of the 5-simplex. To set up and solve this problem fully is too hard and so we will make some simplifying assumptions.

We approach the problem in two ways. First, we focus on the symmetries of $\mathcal{V}_5$ and solve a simplified problem which is consistent with all FR constraints discussed above. This relies on the method we developed in Chapter 2. The calculation allows us to gain an understanding of the structure of the wavefunction globally but contains many assumptions: a harmonic potential, a separable kinetic operator and no $\boldsymbol{v}$ dependence on the moments of inertia. We then try to find the effect on the non-linearity of the potential and the variable moments of inertia by considering the problem on a 1-dimensional subspace of $\mathcal{V}_5$. We call the approaches the 'global approach' and the 'local approach' respectively.

### 3.2.1 A global quantisation

Near the origin of $\mathcal{V}_5$ the potential is harmonic and the metric is flat. We will solve the problem with these assumptions and further that the metric on the full space has no cross terms, so that $g$ is block diagonal. The total wavefunction takes the form

$$|\Psi\rangle = \sum_i u^{(i)}(\boldsymbol{v}) |\Theta\rangle_i \, , \tag{3.13}$$

where the vibrational wavefunctions $u^{(i)}$ satisfy the harmonic oscillator Schrödinger equation in five-dimensions. The potential is

$$V(\boldsymbol{v}) = \frac{5}{6}\frac{1}{2}\hbar\omega^2\boldsymbol{v}.\boldsymbol{v}\,, \tag{3.14}$$

where we have defined the frequency of the vibration, $\omega$. Note that we are using the 6-dimensional vector $\boldsymbol{v}$ to describe a 5-dimensional space. The advantage of this approach is that the symmetry properties of the manifold are simpler. The ground state solution is

$$u_0(\boldsymbol{v}) \propto \mathrm{Exp}\left(-\frac{5\omega}{12\hbar}\boldsymbol{v}.\boldsymbol{v}\right)\,, \tag{3.15}$$

which has energy $\frac{5}{2}\hbar\omega$. The first excited states have degeneracy five. They are of the form

$$u_1^{(i)}(\boldsymbol{v}) \propto \boldsymbol{v}.\boldsymbol{v}_i\,\mathrm{Exp}\left(-\frac{5\omega}{12\hbar}\boldsymbol{v}.\boldsymbol{v}\right) \qquad i = 1,\ldots,6 \tag{3.16}$$

where $\boldsymbol{v}_i$ are vectors defined in Section 3.1. They point in the direction of a $D_5$ preserving mode in $\mathcal{V}_5$. Although there are six vectors $\boldsymbol{v}_i$, there are only five independent states since

$$\sum_i u_1^{(i)} \propto \left(\sum_i \boldsymbol{v}_i\right).\boldsymbol{v} = 0\,. \tag{3.17}$$

These states have energy $E = \frac{7}{2}\hbar\omega$.

We can classify the vibrational wavefunctions by the irreducible representations of the dodecahedral group $I$. The group has five irreducible representations which have dimension $1, 3, 3, 4$ and $5$. We follow the conventions of [35] by naming these the $\mathbf{1}, F_1, F_2, \mathbf{4}$ and $\mathbf{5}$ representations respectively. To find how the vibrational wavefunctions decompose into irreps, we use character theory. For a given irrep, each element of the group $I$ is associated with a character,. The character is the trace of the matrix used to represent the group element, they are invariant under conjugation and so we only need to know the character for a given conjugacy class of group elements. There are five conjugacy classes of $I$, the first just contains the trivial element. Another is the class of $\frac{2\pi}{5}$ rotations about a face of the dodecahedron while the set of $\frac{4\pi}{5}$ rotations about the same axes forms another class. The next is the class of $\frac{2\pi}{3}$ rotations around any axis passing through a vertex of

| Rep | $e$ | $C_5$ | $C_5^2$ | $C_3$ | $C_2$ |
|-----|-----|-------|---------|-------|-------|
| 1 | 1 | 1 | 1 | 1 | 1 |
| $F_1$ | 3 | $\tau$ | $1-\tau$ | 0 | -1 |
| $F_2$ | 3 | $1-\tau$ | $\tau$ | 0 | -1 |
| 4 | 4 | -1 | -1 | 1 | 0 |
| 5 | 5 | 0 | 0 | -1 | 1 |

Table 3.1: The character table of the symmetry group $I$. The constant $\tau$ is equal to $\frac{1}{2}\left(1+\sqrt{5}\right)$.

the dodecahedron. Finally, there is the set of symmetries which correspond to $\pi$ rotations. The character table is displayed in Table 3.1.

Any basis of vibrational wavefunctions can be decomposed into subsets which transform as one of these representations. This is done by analysing how the wavefunctions transform under elements of $I$ which lie in each conjugacy class. In fact, it will be sufficient to consider only the $C_3$ and $C_5$ elements. The ground state wavefunction (3.15) transforms trivially under all symmetries and so it falls into the irrep **1**, also known as the trivial irrep. The excited states are more complicated. The wavefunctions (3.16) transform simply into each other under the symmetries of the dodecahedron. Under the $C_5$ element which leaves the top face invariant, the wavefunctions transform as

$$
C_5 : \boldsymbol{u} = \begin{pmatrix} u_1^{(1)} \\ u_1^{(2)} \\ u_1^{(3)} \\ u_1^{(4)} \\ u_1^{(5)} \\ u_1^{(6)} \end{pmatrix} \rightarrow M_v(g_5)\boldsymbol{u} = \begin{pmatrix} 1 & 0 & 0 & 0 & 0 & 0 \\ 0 & 0 & 0 & 0 & 0 & 1 \\ 0 & 1 & 0 & 0 & 0 & 0 \\ 0 & 0 & 1 & 0 & 0 & 0 \\ 0 & 0 & 0 & 1 & 0 & 0 \\ 0 & 0 & 0 & 0 & 1 & 0 \end{pmatrix} \begin{pmatrix} u_1^{(1)} \\ u_1^{(2)} \\ u_1^{(3)} \\ u_1^{(4)} \\ u_1^{(5)} \\ u_1^{(6)} \end{pmatrix} , \tag{3.18}
$$

while a $C_3$ symmetry around the axis $\boldsymbol{v}_1 + \boldsymbol{v}_2 + \boldsymbol{v}_3$ permutes the wavefunctions as

$$
C_3 : \boldsymbol{u} = \begin{pmatrix} u_1^{(1)} \\ u_1^{(2)} \\ u_1^{(3)} \\ u_1^{(4)} \\ u_1^{(5)} \\ u_1^{(6)} \end{pmatrix} \rightarrow M_v(g_3)\boldsymbol{u} = \begin{pmatrix} 0 & 1 & 0 & 0 & 0 & 0 \\ 0 & 0 & 1 & 0 & 0 & 0 \\ 1 & 0 & 0 & 0 & 0 & 0 \\ 0 & 0 & 0 & 0 & 0 & 1 \\ 0 & 0 & 0 & -1 & 0 & 0 \\ 0 & 0 & 0 & 0 & -1 & 0 \end{pmatrix} \begin{pmatrix} u_1^{(1)} \\ u_1^{(2)} \\ u_1^{(3)} \\ u_1^{(4)} \\ u_1^{(5)} \\ u_1^{(6)} \end{pmatrix} . \tag{3.19}
$$

We follow the notation of Chapter 2. Suppose the wavefunctions fall into the representation $\boldsymbol{\rho}_v$ and let the character of this representation under the symmetry group element $g$ be denoted $\chi^g_{\boldsymbol{\rho}_v}$. We know that this six-dimensional space of excited vibrational wavefunctions contains the combination

$$\sum_i u_1^{(i)} = 0, \tag{3.20}$$

which transforms trivially under all elements, since it is equal to zero. Hence the irreducible decomposition of the wavefunctions takes the form $\boldsymbol{\rho}_v = 1 \oplus \boldsymbol{\rho}'_v$. Under the direct sum of representation, the characters of each representation add. Hence the characters of $\boldsymbol{\rho}'_v$ are

$$\chi^{g_3}_{\boldsymbol{\rho}'_v} = \text{Tr}(M_v(g_3)) - 1 = -1 \tag{3.21}$$

and

$$\chi^{g_5}_{\boldsymbol{\rho}'_v} = \text{Tr}(M_v(g_5)) - 1 = 0. \tag{3.22}$$

Comparison with the character table tells us that $\boldsymbol{\rho}'_v$ is the irrep **5**.

We now combine the vibrational wavefunctions with rotational states. A valid rovibrational state can be created if the vibrational wavefunctions transform in the same way as the spin states. Hence, we must classify the spin states in the same way as we have classified the vibrational states: by decomposing them into irreducible representations. The transformations $C_3$ and $C_5$ have equivalent transformations which act on the Skyrme configurations in $\mathcal{V}_5$ in the form of rotations and isorotations. These can then be turned into operations on spin states by exponentiating the transformations. The $C_5$ operator is

$$\hat{R}_{g_5} = \exp\left(i\frac{2\pi}{5}\hat{L}_z\right)\exp\left(i\frac{6\pi}{5}\hat{K}_z\right), \tag{3.23}$$

where we have chosen the isorotational angle to be $6\pi/5$ rather than $-4\pi/5$ so that this transformation gives rise to a FR number of $+1$. Hence, we have automatically factored out the FR representation mentioned in Chapter 2. The $C_3$ operator is

$$\hat{R}_{g_3} = \exp\left(i\frac{2\pi}{3}\boldsymbol{n}_1.(\hat{L}_x, \hat{L}_y, \hat{L}_z)\right)\exp\left(i\frac{2\pi}{3}\boldsymbol{n}_2.(\hat{K}_x, \hat{K}_y, \hat{K}_z)\right), \tag{3.24}$$

where

$$\boldsymbol{n}_1 = \left(\sqrt{\frac{2}{15}(5 - \sqrt{5})}, 0, \sqrt{\frac{1}{15}(5 + 2\sqrt{5})}\right) \tag{3.25}$$

and

$$\boldsymbol{n}_2 = \left(-\sqrt{\frac{2}{15}(5+\sqrt{5})}, 0, -\sqrt{\frac{1}{15}(5-2\sqrt{5})}\right). \tag{3.26}$$

By considering these operators for a given $(J, I)$ pair, we find a representation of the spin state whose dimension depends on the spin and isospins being considered. The characters of the representation for some low spins and isospin are displayed in Table 3.2.

| $J/I$ | $\frac{1}{2}/\frac{1}{2}$ | $\frac{3}{2}/\frac{1}{2}$ | $\frac{5}{2}/\frac{1}{2}$ | $\frac{7}{2}/\frac{1}{2}$ |
|---|---|---|---|---|
| $\chi_{g_5}^R$ | -1 | $1-\tau$ | $\tau-1$ | 1 |
| $\chi_{g_3}^R$ | 1 | -1 | 0 | 1 |

Table 3.2: The characters of the rotation matrices (3.23) and (3.24).

This gives us enough information to decompose each spin, isospin pair. The decompositions are detailed in Table (3.3).

| $J/I$ | $\frac{1}{2}/\frac{1}{2}$ | $\frac{3}{2}/\frac{1}{2}$ | $\frac{5}{2}/\frac{1}{2}$ | $\frac{7}{2}/\frac{1}{2}$ |
|---|---|---|---|---|
| Irrep decomposition | $\mathbf{4}$ | $\mathbf{3}\oplus\mathbf{5}$ | $F_1\oplus\mathbf{4}\oplus\mathbf{5}$ | $\mathbf{1}\oplus F_1\oplus F_2\oplus\mathbf{4}\oplus\mathbf{5}$ |

Table 3.3: The irreducible decomposition of the spin state.

The spin $\frac{7}{2}$ states have a trivial factor and so there is a spin $\frac{7}{2}$ state which transforms trivially under all of these rotation-isorotation operators. This may be combined with the ground state $u_0$. The total state is of the form

$$|\Psi\rangle = u_0(\boldsymbol{v})\left(\sqrt{3}\left(|\frac{7}{2}, \frac{7}{2}\rangle |\frac{1}{2}, \frac{1}{2}\rangle - |\frac{7}{2}, -\frac{7}{2}\rangle |\frac{1}{2}, -\frac{1}{2}\rangle\right)\right.$$
$$\left.+\sqrt{7}\left(|\frac{7}{2}, \frac{3}{2}\rangle |\frac{1}{2}, -\frac{1}{2}\rangle + |\frac{7}{2}, -\frac{3}{2}\rangle |\frac{1}{2}, \frac{1}{2}\rangle\right)\right), \tag{3.27}$$

as expected since this state is seen in rigid body quantisation. Further, these decompositions tell us that the vibrational wavefunctions $\{u_1^{(i)}\}$, which fall into the $\mathbf{5}$ representation, may be combined with spin $\frac{3}{2}$, spin $\frac{5}{2}$ and spin $\frac{7}{2}$ states, since these all have a $\mathbf{5}$ factor. The spin $\frac{3}{2}$ state, $|\Psi\rangle^{(\frac{3}{2})}$ is vastly more complicated than

41

(3.27). We may calculate it using the technique described in Chapter 2. It is of the form

$$\sum_{i,L_3,K_3} a_{i,L_3,K_3} u^{(i)} \left| \frac{3}{2}, L_3 \right\rangle \left| \frac{1}{2}, K_3 \right\rangle .$$ (3.28)

Thirty-two of its forty-eight coefficients are non-zero and the analytic expression for any one of these coefficients is not easily written down. However, we can check that the rovibrational wavefunction is the correct one by viewing it at specific points in $\mathcal{V}_5$ where its expression simplifies. For example at $\boldsymbol{v} = (0,0,0,0,0,0)$ the wavefunction is

$$|\Psi\rangle^{(\frac{3}{2})} \propto \sum_i u_1^{(i)}(\boldsymbol{v}) = 0 .$$ (3.29)

This is necessary as no spin $\frac{3}{2}$, isospin $\frac{1}{2}$ states are allowed at the dodecahedron. At the point $\boldsymbol{v} = \boldsymbol{v}_1$ the wavefunction is proportional to

$$\left| \frac{3}{2}, \frac{3}{2} \right\rangle \left| \frac{1}{2}, -\frac{1}{2} \right\rangle + \left| \frac{3}{2}, -\frac{3}{2} \right\rangle \left| \frac{1}{2}, \frac{1}{2} \right\rangle ,$$ (3.30)

which is the state allowed by the $D_5$ symmetry preserved along the line $\lambda \boldsymbol{v}_1$ in $\mathcal{V}_5$. There are similar excited rovibrational states for spin $\frac{5}{2}$ and $\frac{7}{2}$.

The lowest energy spin $\frac{1}{2}$, isospin $\frac{1}{2}$ state is not permitted on $\mathcal{V}_5$. Instead it is concentrated on a vibrational manifold which transforms as the **4** representation. Baskerville found such a vibration in [35]. It has frequency $\omega' = 0.45$ compared to $\omega = 0.302$ for the vibration corresponding to $\mathcal{V}_5$. Hence the spin $\frac{1}{2}$ state will have approximately

$$\Delta E_v = \hbar(\omega' - \omega) ,$$ (3.31)

more vibrational energy than the excited states discussed above.

We can crudely approximate the energies of the four states mentioned above using

$$E = \frac{\hbar^2}{2V}J(J+1) + \frac{\hbar^2}{2U}I(I+1) + \frac{1}{2}\hbar\omega(5 + 2k_1) + \frac{1}{2}\hbar\omega'(4 + 2k_2) ,$$ (3.32)

where $V$ and $U$ are the average value of the spatial and isospatial moment of inertia tensors of the $B = 7$ Skyrmion and $k_i$ are equal to zero or one, depending on which state is being considered. To compare this to experimental data we must calibrate the model. We will do this later. For now, we present the rotational and vibrational contributions in Table 3.4. We see that one could calibrate the model

42

| State | Rotational | Isorotational | Vibration 1 | Vibration 2 |
|---|---|---|---|---|
| $\frac{7}{2}$ | $\frac{\hbar^2}{2V}\frac{7}{2}\frac{9}{2}$ | $\frac{\hbar^2}{2U}\frac{1}{2}\frac{3}{2}$ | $\frac{5}{2}\hbar\omega$ | $2\hbar\omega'$ |
| $\frac{3}{2}$ | $\frac{\hbar^2}{2V}\frac{3}{2}\frac{5}{2}$ | $\frac{\hbar^2}{2U}\frac{1}{2}\frac{3}{2}$ | $\frac{7}{2}\hbar\omega$ | $2\hbar\omega'$ |
| $\frac{5}{2}$ | $\frac{\hbar^2}{2V}\frac{5}{2}\frac{7}{2}$ | $\frac{\hbar^2}{2U}\frac{1}{2}\frac{3}{2}$ | $\frac{7}{2}\hbar\omega$ | $2\hbar\omega'$ |
| $\frac{7}{2}$ | $\frac{\hbar^2}{2V}\frac{7}{2}\frac{9}{2}$ | $\frac{\hbar^2}{2U}\frac{1}{2}\frac{3}{2}$ | $\frac{7}{2}\hbar\omega$ | $2\hbar\omega'$ |
| $\frac{1}{2}$ | $\frac{\hbar^2}{2V}\frac{1}{2}\frac{3}{2}$ | $\frac{\hbar^2}{2U}\frac{1}{2}\frac{3}{2}$ | $\frac{5}{2}\hbar\omega$ | $3\hbar\omega'$ |

Table 3.4: The approximate energy contributions for each state we discuss in the text. Here, we separate the approximate rotational, isorotation, vibrational (from $\mathcal{V}_5$) and vibrational (from the 4-dimensional vibrational manifold) energies.

to give a spin $\frac{7}{2}$ state which lies above the spin $\frac{1}{2}$ state, which could turn lie above the $\frac{3}{2}$ state as required from experimental data. However, our approximations are rather crude and we don't have much faith in the numbers of Table 3.4.

Several important issues were not considered in this analysis. Some are:

1. The potential (3.14) is harmonic. However, away from the origin of $\mathcal{V}_5$, the potential flattens out since the Skyrmion separates into individual clusters. A Morse potential or a numerically generated potential would reflect the physics more accurately.

2. We estimate the rotational energy by taking the moment of inertia tensor to be equal to its value at the dodecahedron. As the Skyrmion deforms, the moment of inertia tensor will change significantly.

3. The metric on $\mathcal{V}_5$ was assumed to be flat. This is true near the dodecahedron, but not away from it.

4. We assumed there were no cross-terms between the vibrational and rotational parts of the metric on $\mathcal{V}_5$. This was unjustified and in other systems the cross-terms can make a considerable difference to the energies of the states [51].

5. The spin $\frac{1}{2}$ state is concentrated on a vibrational manifold which transforms as the irrep **4**. To estimate the energy of this state, we should attempt to understand this manifold better.

In the next section, we will try to take account of the first three points mentioned here by considering the problem along a special line in $\mathcal{V}_5$.

## 3.2.2   A local quantisation

In the harmonic approach, the potential and the total wavefunctions are isotropic. In reality, the potential has low energy valleys in certain directions, such as along the special symmetric lines discussed in Section (3.1). The line preserving $C_3$ symmetry has the lowest asymptotic energy and so it is likely the lowest energy direction in $\mathcal{V}_5$. Hence, in reality the total wavefunction will be concentrated along these lines. We consider the problem restricted to the $C_3$ symmetric line, which reduces the difficulty of the problem. The simplicity means that we can take account of some of the complications neglected in the previous section. In the harmonic approximation, the vibrational wavefunction restricted to this line is a one-dimensional harmonic oscillator which satisfies

$$\left( -\frac{\hbar^2}{2} \frac{d^2}{ds^2} + \frac{1}{2} \omega^2 s^2 + E_J(0) \right) u_{\mathrm{h}}(s) = E u_{\mathrm{h}}(s) \,. \tag{3.33}$$

We have introduced the coordinate $s$ which parametrises the line. We will study the related Schrödinger equation but with the anharmonic potential, the variable moments of inertia and the correction to the flat metric incorporated.

The $C_3$ symmetry present on this line restricts the form of the metric which is now 7-dimensional. Using the same notation as in Section 2.1 the metric is

$$g = \begin{pmatrix} \Lambda & & 0 \\ & U & -W \\ 0 & -W^T & V \end{pmatrix} , \tag{3.34}$$

where $U$, $W$ and $V$ are $3 \times 3$ matrices and $\Lambda$ is a scalar. The kinetic energy is invariant under the action of the symmetry group of the vibration. This restriction means that, along this line in $\mathcal{V}_5$, the cross terms in the metric vanish and the kinetic energy is separable. The wavefunction takes the form

$$|\Psi\rangle = \sum_i u_i(s) |\Theta\rangle_i \,. \tag{3.35}$$

Consider a rotational state with spin $J$ and suppose the rotational energy contribution $E_J(s)$ satisfies

$$-\frac{\hbar^2}{2}\nabla^2\Theta_J = E_J(s)\Theta_J\,. \tag{3.36}$$

Note that the rotational energy contribution is a function of $s$ through its dependence on the moments of inertia which vary as the Skyrmion deforms. Then the Schrödinger equation

$$-\frac{\hbar^2}{2}\Delta\,|\Psi\rangle + V(s)\,|\Psi\rangle = E\,|\Psi\rangle\,, \tag{3.37}$$

reduces to the 1-dimensional equation

$$\left(-\frac{\hbar^2}{2\sqrt{|g|}}\partial_s\left(\frac{\sqrt{|g|}}{\Lambda}\partial_s\right) + V(s) + E_J(s)\right)u(s) = Eu(s)\,. \tag{3.38}$$

To solve this we must first generate $g(s)$, $V(s)$ and $E_J(s)$. We will do this using gradient flow.

Gradient flow generates a path of steepest descent in field space. We use the separated Skyrmion clusters as initial configurations which are then evolved in gradient flow time $\tau$ according to

$$\frac{d\boldsymbol{\pi}}{d\tau} = -\frac{\delta\mathbb{M}_7}{\delta\boldsymbol{\pi}}\,, \tag{3.39}$$

where $\boldsymbol{\pi}$ are the pion fields and $\mathbb{M}_7$ is the potential energy (1.7). This flow reduces the potential energy of the system and ends at a stationary point of field space. The fields $\boldsymbol{\pi}(\tau)$ approximate the Skyrme configurations along a line in $\mathcal{V}_5$. The solution of (3.39) is beyond analytic calculation and so we must use a numerical code to calculate the flow. The energy $V(\tau)$ and the metric $g(\tau)$ are calculated at numerous points during the process.

The metric at time $\tau$ can be expressed in terms of the currents $R_i(\tau) = (\partial_i U)U^{-1}$ and $T_i(\tau) = \frac{i}{2}[\sigma_i, U]U^{-1}$. The moments of inertia and $\Lambda$ are given

by

$$\Lambda = -\int \text{Tr}\left(R_\tau R_\tau + \frac{1}{4}[R_\tau, R_i][R_\tau, R_i]\right) d^3x \tag{3.40}$$

$$U_{ij} = -\int \text{Tr}\left(T_i T_j + \frac{1}{4}[R_k, T_i][R_k, T_j]\right) d^3x \tag{3.41}$$

$$W_{ij} = \int \epsilon_{jlm} x_l \text{Tr}\left(T_i R_m + \frac{1}{4}[R_k, T_i][R_k, R_m]\right) d^3x \tag{3.42}$$

$$V_{ij} = -\int \epsilon_{ilm}\epsilon_{jnp} x_l x_n \text{Tr}\left(R_m R_p + \frac{1}{4}[R_k, R_m][R_k, R_p]\right) d^3x \,. \tag{3.43}$$

In contrast to Chapter 2, the moments of inertia now depend on $\tau$.

Gradient flow time is an unnatural parameter when the Skyrmion clusters are widely separated and near the dodecahedral configuration. Thus, once we have found our quantities numerically we change variables to the geodesic distance, $s$ [12]. This can be defined in terms of the vibrational kinetic energy by demanding

$$T_{\text{vib}} = \frac{1}{2}\dot{s}^2 = \frac{1}{2}\Lambda(\tau)\dot{\tau}^2 \,, \tag{3.44}$$

which means that

$$s(\tau) = \int^\tau \sqrt{\Lambda(\tau')} \, d\tau' \,. \tag{3.45}$$

There are several advantages to this new coordinate. First, the geodesic distance is related to the cluster separation, $r$, asymptotically. We can calculate how the moments of inertia vary with $r$ and this gives an asymptotic check of the numerics. Additionally we are able to add an analytic tail to the numerically derived potential and moments of inertia. Further, we may now calculate the harmonic frequency near the origin of $\mathcal{V}_5$ and compare it to what was calculated in [35]. We find the frequency to be 0.34 compared with 0.302 as found in [35]. These are approximately the same, showing that the methods are consistent. The small difference is likely due to the different pion masses used. Finally, the new coordinate simplifies the Schrödinger equation (3.38). It now reads

$$\left(-\frac{\hbar^2}{2}\frac{d^2}{ds^2} - \frac{\hbar^2}{4}\partial_s \log(|g|)\frac{d}{ds} + V(s) + E_J(s)\right) u(s) = E u(s) \,. \tag{3.46}$$

From now on, $s$ will refer exclusively to the geodesic distance.

We must generate two gradient flows. For the first $(s > 0)$, the initial configuration for the gradient flow is constructed using a symmetrised product ansatz of

a $B = 3$ Skyrmion with a $B = 4$ Skyrmion. These are orientated as in Figure 3.4. The second flow ($s < 0$) begins with seven individual Skyrmions, six arranged in a hexagon with one in the center. We then patch the flows together at $s = 0$. The $C_3$ symmetry constrains the form of the metric. We find that $U$, $V$ and $W$ are all diagonal. Further

$$U_{11} = U_{22},\ V_{11} = V_{22},\ \text{and}\ W_{11} = W_{22}\,, \tag{3.47}$$

and we have set $\Lambda = 1$ by choosing our parameter to be the geodesic distance.

By considering the global wavefunctions derived in Section 3.2.1 restricted to the line of $C_3$ symmetric configurations in $\mathcal{V}_5$, we can discover which spin states are allowed along the line. The global wavefunctions of Section 3.2.1 are orientated so that the Skyrmion has manifest $D_5$ symmetry. We can reorient the Skyrmion (and spin state) to have manifest $C_3$ symmetry by applying a suitable rotation-isorotation operator to the spin states. Once the global wavefunction has been restricted and rotated, the spin $\frac{7}{2}$ ground state becomes proportional to

$$\left(|\tfrac{7}{2}, \tfrac{1}{2}\rangle\, |\tfrac{1}{2}, \tfrac{1}{2}\rangle + |\tfrac{7}{2}, -\tfrac{1}{2}\rangle\, |\tfrac{1}{2}, -\tfrac{1}{2}\rangle\right) + \left(|\tfrac{7}{2}, -\tfrac{5}{2}\rangle\, |\tfrac{1}{2}, \tfrac{1}{2}\rangle - |\tfrac{7}{2}, \tfrac{5}{2}\rangle\, |\tfrac{1}{2}, -\tfrac{1}{2}\rangle\right) \tag{3.48}$$

$$+ \frac{2}{\sqrt{7}}\left(|\tfrac{7}{2}, \tfrac{7}{2}\rangle\, |\tfrac{1}{2}, \tfrac{1}{2}\rangle - |\tfrac{7}{2}, -\tfrac{7}{2}\rangle\, |\tfrac{1}{2}, -\tfrac{1}{2}\rangle\right) \equiv |\Theta\rangle^{(1)}_{\frac{7}{2}} + |\Theta\rangle^{(2)}_{\frac{7}{2}} + \frac{2}{\sqrt{7}}|\Theta\rangle^{(3)}_{\frac{7}{2}}\,, \tag{3.49}$$

which is the state allowed by rigid body quantisation, as expected. Hence our ansatz for this rovibrational state is

$$|\Psi\rangle^{g}_{\frac{7}{2}} = u^{(1)}_{\frac{7}{2}}(s)\, |\Theta\rangle^{(1)}_{\frac{7}{2}} + u^{(2)}_{\frac{7}{2}}(s)\, |\Theta\rangle^{(2)}_{\frac{7}{2}} + \frac{2}{\sqrt{7}} u^{(3)}_{\frac{7}{2}}(s)\, |\Theta\rangle^{(3)}_{\frac{7}{2}}\,, \tag{3.50}$$

with the $u^{(i)}$ equal at $s = 0$ to satisfy the FR constraint at the dodecahedron. By a similar method, the ansatz for the vibrationally excited spin $\frac{3}{2}$, $\frac{5}{2}$ and $\frac{7}{2}$ states are

$$|\Psi\rangle_{\frac{3}{2}} = u_{\frac{3}{2}}(s)\left(\left|\tfrac{3}{2}, \tfrac{1}{2}\right\rangle \left|\tfrac{1}{2}, \tfrac{1}{2}\right\rangle + \left|\tfrac{3}{2}, -\tfrac{1}{2}\right\rangle \left|\tfrac{1}{2}, -\tfrac{1}{2}\right\rangle\right) \tag{3.51}$$

$$|\Psi\rangle_{\frac{5}{2}} = u^{(1)}_{\frac{5}{2}}(s)\left(\left|\tfrac{5}{2}, \tfrac{1}{2}\right\rangle \left|\tfrac{1}{2}, \tfrac{1}{2}\right\rangle + \left|\tfrac{5}{2}, -\tfrac{1}{2}\right\rangle \left|\tfrac{1}{2}, -\tfrac{1}{2}\right\rangle\right)$$

$$+ \frac{1}{\sqrt{2}} u^{(2)}_{\frac{5}{2}}(s)\left(\left|\tfrac{5}{2}, -\tfrac{5}{2}\right\rangle \left|\tfrac{1}{2}, \tfrac{1}{2}\right\rangle - \left|\tfrac{5}{2}, \tfrac{5}{2}\right\rangle \left|\tfrac{1}{2}, -\tfrac{1}{2}\right\rangle\right)$$

$$|\Psi\rangle^{e}_{\frac{7}{2}} = \frac{3}{2\sqrt{7}} v^{(1)}_{\frac{7}{2}}(s)\, |\Theta\rangle^{(1)}_{\frac{7}{2}} + \frac{1}{2\sqrt{7}} v^{(2)}_{\frac{7}{2}}(s)\, |\Theta\rangle^{(2)}_{\frac{7}{2}} - v^{(3)}_{\frac{7}{2}}(s)\, |\Theta\rangle^{(3)}_{\frac{7}{2}}\,.$$

Consider the spin $\frac{3}{2}$ state (3.51). Inserting this ansatz into the Schrödinger equation (3.10) we find that $u_{\frac{3}{2}}$ satisfies

$$\left( \frac{\hbar^2}{2} \left( \frac{V_{11}}{2\,(U_{11}V_{11} - W_{11}^2)} + \frac{3U_{11}}{2\,(V_{11}U_{11} - W_{11})} + \frac{1}{U_{33}V_{33} - W_{33}^2} \left( \frac{9}{4}U_{33} + \frac{1}{4}V_{33} - \frac{3}{2}W_{33} \right) \right) \right.$$
$$\left. - \frac{\hbar^2}{2} \frac{d^2}{ds^2} - \frac{\hbar^2}{4} \partial_s \log(|g|) \frac{d}{ds} + V(s) \right) u_{\frac{3}{2}}(s) = E u_{\frac{3}{2}}(s).$$

(3.52)

We would like to understand the contributions from rotations and vibrations separately. There is no unique way to split the energy; we choose to define the rotational energy contribution as the rigid body energy of the undeformed Skyrmion, $E_J(0)$. We may then split the energy $E$ into three parts: the classical mass of the Skyrmion $\mathbb{M}_7 = V(0)$, the contribution from the rigid rotation $E_J(0)$, and the energy contribution from the vibration $\epsilon_{\text{vib}}$. We write $E = \mathbb{M}_7 + E_J(0) + \epsilon_{\text{vib}}$ and the Schrödinger equation becomes

$$\left( -\frac{\hbar^2}{2} \frac{d^2}{ds^2} - \frac{\hbar^2}{4} \partial_s \log(|g|) \frac{d}{ds} + V_{\text{eff}}(s) \right) u_{\frac{3}{2}}(s) = \epsilon_{\text{vib}} u_{\frac{3}{2}}(s), \qquad (3.53)$$

where $V_{\text{eff}}(s) = V(s) - \mathbb{M}_7 + E_J(s) - E_J(0)$. Note that $V_{\text{eff}}(0) = 0$. We must now solve (3.53) numerically. As the potential energy in the direction of negative $s$ is very high and approximately harmonic where our wavefunctions are concentrated, the wavefunctions approximately satisfy the harmonic oscillator equation for large negative $s$. This gives us a boundary condition on $u(s)$. We then solve equation (3.53) numerically using a shooting technique, knowing that the wavefunction must decay asymptotically for large $s$.

The states made from several spin states are harder to deal with. For example, the spin $\frac{7}{2}$ ground state (3.50) contains three vibrational wavefunctions each satisfying a Schrödinger equation such as (3.53), with eigenvalues $\epsilon_{\text{vib}}^{(i)}$. However, these eigenvalues are all different since the effective potential is different in each case. Hence the rovibrational wavefunction (3.50) cannot be the true energy eigenstate, though it is an approximate one. Inclusion of cross terms in the metric, which appear on the total manifold, would let the states mix giving a consistent formalism. We approximate the true energy by calculating a weighted average, based on the relative importance of each term in the harmonic approximation. In this case the

approximate energy $\bar{\epsilon}_{\text{vib}}$ is equal to

$$\bar{\epsilon}_{\text{vib}} = \frac{7}{18} \left( \epsilon_{\text{vib}}^{(1)} + \epsilon_{\text{vib}}^{(2)} + \frac{4}{7}\epsilon_{\text{vib}}^{(3)} \right) . \tag{3.54}$$

We deal with all the states in this way.

**Calibration of the model**

Before comparing our results to experimental data we must calibrate the model. All previous calibrations are based on zero mode quantisation and as such we don't necessarily expect our choice of parameters to match previous studies. The vibrational energy contribution is of order $\hbar$ while the rotational energy contribution is of order $\hbar^2$. Thus the relative energies of the states will be sensitive to the value of $\hbar$.

In Figure 3.5 the quantum energy of each state is plotted (in Skyrme units) for various values of $\hbar$. The most important feature of the plot is that the spin $\frac{7}{2}$ state increases in energy, relative to the other states, as $\hbar$ increases. This is because the spin $\frac{7}{2}$ state has the largest rotational energy and the smallest vibrational energy; rotational effects dominate for large $\hbar$ while vibrational effects dominate for small $\hbar$. To match experimental data the spin $\frac{7}{2}$ state must lie between the spin $\frac{3}{2}$ state and the first spin $\frac{5}{2}$ state. This occurs when

$$60 < \hbar < 70 , \tag{3.55}$$

and as such we demand that $\hbar$ lies in this interval. For illustrative purposes we fix $\hbar = 65$. This is large compared to the parameter choice of [37] and [30] where the authors use rigid body quantisation. However, it is closer to the value of $\hbar$ used by Adkins, Nappi and Witten [21]. In their seminal paper, they quantised the $B = 1$ Skyrmion. This has no vibrational corrections and so it makes sense that a quantisation taking account of vibrational modes (such as ours) should have similar parameters to theirs.

We are left to choose the value of $F_\pi$, as $\hbar$ fixes the dimensionless constant $e$ through the identity $\hbar = 2e^2$. We will consider two alternative calibrations:

(i) $F_\pi = 60$ MeV

(ii) $F_\pi = 139$ MeV.
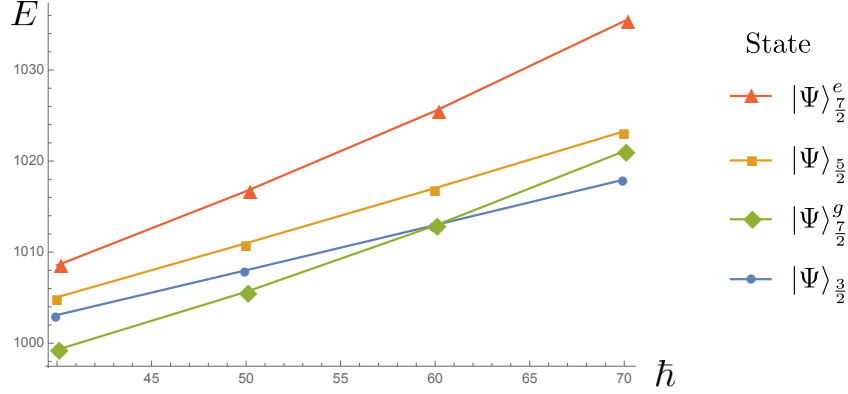
Figure 3.5: The quantum energy of each state (in Skyrme units) as a function of $\hbar$.

Parameter choice (i) gives a good fit to the size of the gaps in the energy spectrum but underestimates the total mass of the Skyrmion compared to the total mass of $^7$Li. Choice (ii) gives a reasonable value of the total mass but overestimates the gaps in the spectrum. We have fixed the dimensionless pion mass $m$ to 1 throughout.

**Results**

We solved the Schrödinger equation (3.53) for all states discussed in Section 3.2.2. The numerically generated vibrational wavefunctions $u(s)$ for each state is plotted in Table 3.5. We also note the classical mass of the Skyrmion $\mathbb{M}_7$, the energy contribution from rotations $E_J(0)$ and the contribution from vibrations $\epsilon_{\text{vib}}$, as well as the total energy of each state $E$. Our results are then compared to experimental data in Table 3.6 for each calibration (i) and (ii).

The results are promising. All of the states considered are seen experimentally and we are only missing the spin $\frac{1}{2}$ state which we have already discussed. The ordering is correct and most importantly, the second spin $\frac{7}{2}$ state lies between the spin $\frac{3}{2}$ and $\frac{5}{2}$ states. The spin $\frac{7}{2}$ state in our model has too much energy to be identified with the experimentally observed state. Hence, this is likely described by a spin $\frac{7}{2}$ state excited in a different vibrational manifold. The size of the gaps in the energy spectrum are reasonable for calibration (i) and much too large for calibration (ii).
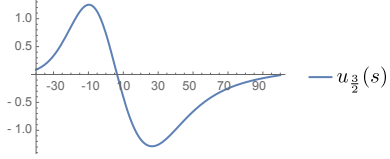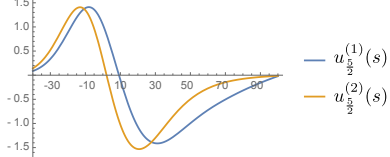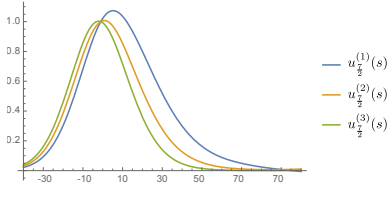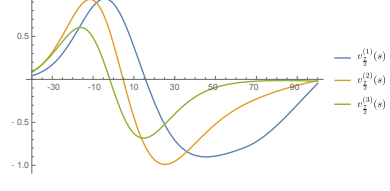
| State | Vibrational wavefunction | $\mathcal{M}_7 + E_J(0) + \epsilon_{\text{vib}}$ | $E$ |
|---|---|---|---|
| $\lvert \Psi \rangle_{\frac{3}{2}}$ |  | $985.13 + 10.34 + 20.88$ | $1016.35$ |
| $\lvert \Psi \rangle_{\frac{5}{2}}$ |  | $985.13 + 15.91 + 19.09$ | $1020.13$ |
| $\lvert \Psi \rangle_{\frac{7}{2}}^{\text{ground}}$ |  | $985.13 + 23.75 + 8.91$ | $1017.79$ |
| $\lvert \Psi \rangle_{\frac{7}{2}}^{\text{excited}}$ |  | $985.13 + 23.75 + 22.23$ | $1031.11$ |

Table 3.5: The numerical results for quantisation along the $C_3$ direction. We display the composite vibrational wavefunctions, classical mass energy contribution, rotational energy contribution and vibrational energy contribution for each spin state considered in the text. All results are in Skyrme units with $\hbar = 65$.

The remaining unexplained experimental states of the $^7$Li spectrum have spin $\frac{1}{2}$, $\frac{5}{2}$, $\frac{3}{2}$ and $\frac{3}{2}$. These have natural descriptions in our model. The spin $\frac{1}{2}$ and spin $\frac{5}{2}$ states are not allowed by the vibration we've considered. Instead, they will be excited in the mode with **4** symmetry. This vibration also accommodates the second spin $\frac{7}{2}$ state. In fact, the three states lie on an approximate rotational band [38], giving credence to the idea. The excited spin $\frac{3}{2}$ states have isospin $\frac{3}{2}$, a possibility we neglected for simplicity. This would also describe the ground states of $^7$B and $^7$He which have spin $\frac{3}{2}$.

The mass of the $^7$Li nucleus is 6535 MeV. Calibration (ii) gives the total mass

| | Energy relative to ground state (MeV) | | |
|---|---|---|---|
| State | Experiment | Calibration (i) | Calibration (ii) |
| $\lvert \Psi \rangle_{\frac{3}{2}}$ | 0 | 0 | 0 |
| $\lvert \Psi \rangle_{\frac{7}{2}}^{\text{ground}}$ | 4.63 | 3.80 | 8.79 |
| $\lvert \Psi \rangle_{\frac{5}{2}}$ | 6.68 | 9.95 | 23.06 |
| $\lvert \Psi \rangle_{\frac{7}{2}}^{\text{excited}}$ | 9.67 | 38.85 | 90.01 |

Table 3.6: A comparison of the experimentally obtained energy spectrum of $^7$Li (column 1) with the results from our calculation using Calibration (i) (column 2) and Calibration (ii) (column 3). The experimental data is from [38].

of the ground state to be 6195 MeV which is very close to the experimental value. Calibration (i) gives a much smaller value, only 2674 MeV. There are several ways this could be remedied. First, we have only taken one of the Skyrmion's vibrational modes into account. There are approximately $6B$ modes, all of which will contribute to the energy. The Casimir energy contribution is also large, a 50% correction in the $B = 1$ sector [31], though does not necessarily alter the structure of the energy spectrum [39]. Finally, the Lagrangian may be altered to include a 6th order term which can be chosen to contribute positively to the mass. When this term is the same order as the other terms in the Lagrangian, the Skyrmion solutions do not change significantly [40]. Thus the calculation in this paper would not vary greatly except for the total energy. These three factors could combine to give a reasonable value for the total mass. They also highlight the uncertainty in calculations of total mass in the Skyrme model.

Inclusion of the $C_3$ vibration has given us a good model of the spin $\frac{3}{2}$, $\frac{7}{2}$ and $\frac{5}{2}$ states of the $^7$Li/$^7$Be isodoublet. Further, it brings us closer to the cluster model of nuclei. This is apparent when we plot the classical baryon density at the second maximum of the vibrational wavefunctions. The quantum state is an admixture of different configurations. The leftmost density plotted in Figure 3.6 is a highly contributing configuration for the excited vibrational wavefunctions. The other important configuration is on the other side of the vibration. With this classical picture in mind, the spin $\frac{3}{2}$ state exhibits clustering while the spin $\frac{7}{2}$ state does not. This goes against conventional wisdom in the cluster model where the ground

state is generally the most isotropic.
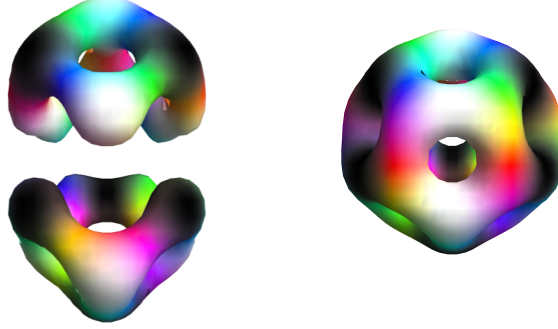


Figure 3.6: Plots of the baryon density at a maximum value of the vibrational wavefunctions. The spin $\frac{3}{2}$ state is on the left while the spin $\frac{7}{2}$ state is on the right.

### 3.2.3 The root mean square matter radius

Although the energy spectrum results are promising, they are sensitive to the calibration of the model. Hence, it would be better to find a result robust to calibration changes. We saw in Figure 3.6 that the different states appear to have different sizes and so a statement about the size of the nucleus may be the best route to find an interesting result. The simplest quantitative measure of the size of a nucleus is the root mean square (rms) matter radius, $\langle r_m \rangle$. We can calculate this for each value of $s$ by taking the square root of

$$r_m^2(s) = \frac{\int |\boldsymbol{x}|^2 \rho(\boldsymbol{x}, s)\, d^3x}{\int \rho(\boldsymbol{x}, s)\, d^3x}\,, \tag{3.56}$$

where $\rho(\boldsymbol{x}, s)$ is the energy density of the Skyrme configuration at $s$. For a given state, the rms matter radius is then

$$\langle r_m \rangle = \langle \Psi_J | r_m(s) | \Psi_J \rangle = \int r_m(s) u_J^2(s) \sqrt{|g|}\, ds\,, \tag{3.57}$$

where we have taken the vibrational wavefunctions to be normalised. We find that the matter radius of the spin $\frac{3}{2}$ state, in Skyrme units, is

$$\langle r_m \rangle_{\frac{3}{2}} = 2.11. \tag{3.58}$$

53

Experiments are unable to measure the matter radius directly. However in most nuclei the matter and charge radii are very similar. Thus we compare (3.58) to the experimentally determined charge radius, 2.444 fm. The result depends on our choice of $F_\pi$. Calibration (i) gives a matter radius of 2.43 fm, matching the experimental value. However calibration (ii) gives a very small radius, 1.05 fm. Earlier we found that calibration (i) gave a better match to the energy spectrum. This result adds weight to the idea that it is the better choice. Regardless, ratios of lengths are independent of $F_\pi$. As such we can compare the matter radii for the spin $\frac{7}{2}$ and spin $\frac{3}{2}$ states and have more trust in the result. We find that

$$\frac{\langle r_m \rangle_{\frac{3}{2}}}{\langle r_m \rangle_{\frac{7}{2}}} = 1.11 \,. \tag{3.59}$$

Thus we predict that the ground state of $^7$Li is 11% larger than the second excited state, which has spin $\frac{7}{2}$. The rms charge radius of an excited state is difficult to measure experimentally. As such there is no data to confirm our prediction. This is an important signature for the Skyrme model as this prediction is in conflict with the standard cluster model and shell model predictions.

### 3.2.4 Comparison with harmonic approximation

We are interested in the difference between the harmonic approximation and the Schrödinger equation displayed in (3.53). The three aspects we were able to include by restricting the equation were: the anharmonic potential, the non-flat metric of $\mathcal{V}_5$ and the $s$ dependence of the moments of inertia. We will try and extract the consequence of each of these effects.

In Figure 3.7, we plot the spin $\frac{3}{2}$ vibrational wavefunction $u_{\frac{3}{2}}$ against the harmonic wavefunction. The main difference between the wavefunctions is that the harmonic wavefunction is equally distributed around $s = 0$ while $u_{\frac{3}{2}}$ is focused more in the $s > 0$ region. This is because the potential is much flatter in this direction, where the Skyrmion splits into the $3 + 4$ cluster rather than the high energy seven-Skyrmion direction. The harmonic wavefunction has around 50% more energy than $u_{\frac{3}{2}}$, since the true potential flattens out asymptotically. This is a large difference. In Chapter 2, we discussed calculating the binding energy of a vibrationally quantised Skyrmion using a harmonic approximation. This result
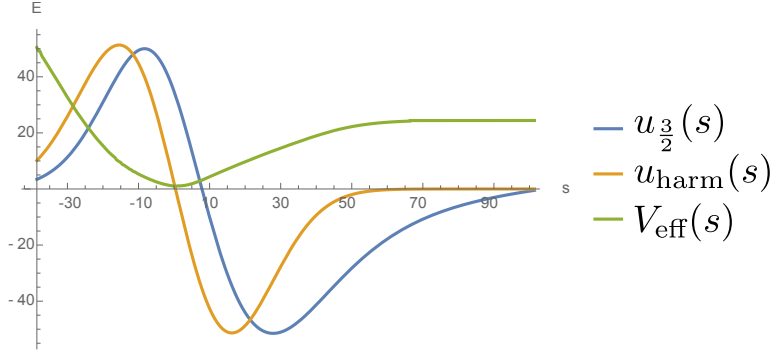
Figure 3.7: A comparison between the simple harmonic wavefunction (orange) and the wavefunction calculated in this chapter (blue). The effective potential is also plotted in green.

shows that a harmonic calculation could vastly overestimate the total quantum energy of the Skyrmion.

The best way to understand the moment of inertia dependence is to compare two vibrational wavefunctions with the same spin, such as the spin $\frac{5}{2}$ ones. The spin $\frac{5}{2}$ rovibrational wavefunction has the form

$$u_{\frac{5}{2}}^{(1)}\left(|\frac{5}{2},\frac{1}{2}\rangle\,|\frac{1}{2},\frac{1}{2}\rangle + |\frac{5}{2},-\frac{1}{2}\rangle\,|\frac{1}{2},-\frac{1}{2}\rangle\right) + \frac{u_{\frac{5}{2}}^{(2)}}{\sqrt{2}}\left(|\frac{5}{2},-\frac{5}{2}\rangle\,|\frac{1}{2},\frac{1}{2}\rangle - |\frac{5}{2},\frac{5}{2}\rangle\,|\frac{1}{2},-\frac{1}{2}\rangle\right).$$

(3.60)

The vibrational wavefunctions $u_{\frac{5}{2}}^{(1)}$ and $u_{\frac{5}{2}}^{(2)}$ have a vibrational energy of 17.3 and 22.7 respectively, in Skyrme units. The second spin $\frac{5}{2}$ state has much higher energy. This can be understood by considering the body-fixed spin classically. The highly excited state has $|L_3| = \frac{5}{2}$. This means that the spin is around the 3-axis. This gives a large energy contribution since the Skyrmion is prolate in this direction for positive $s$, where the vibrational wavefunction is concentrated. The lower energy spin $\frac{5}{2}$ state has $|L_3| = \frac{1}{2}$ which allows it to rotate about an axis orthogonal to the prolate one, which gives a much lower energy.

We can find the effect of the flat metric by redoing the calculation of this section but with the vibrational cross term equal to zero. We plot the spin $\frac{3}{2}$ vibrational wavefunction for each of these two cases in Figure (3.8). We see that the wavefunction with the metric correction included is concentrated more towards $s = 0$. The correction is a measure of the distance in configuration space. This

55

shows that the flat metric underestimates the distances in $\mathcal{V}_5$, though it is a small correction.
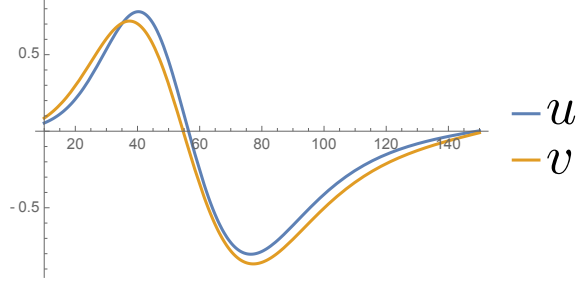


Figure 3.8: A comparison between the wavefunctions when the metric correction is included. The vibrational wavefunction with the cross-terms included is denoted $u$, while the vibrational wavefunction without the cross-term is $v$.

Overall, there is a large difference between the wavefunctions in both schemes, especially their energies. To really understand their differences we should try to solve the Schrödinger equation on the full 5-dimensional manifold which is beyond our current techniques.

## 3.3 Conclusion and outlook

In this chapter we have considered the inclusion of vibrational modes in the quantisation of the $B = 7$ Skyrmion. We argued that to understand the low lying states of the $^7$Li/$^7$Be isodoublet one can truncate to quantisation along a 1-dimensional line in vibrational space, $\mathcal{V}_5$. The space has a rich structure best understood using the geometry of a 5-simplex. Using this, we picked a special direction in the space to quantise along. The calculation gives a reasonable energy spectrum, much closer to the experimental data than had previously been found using rigid body quantisation. Most importantly, the spectrum can explain all experimentally seen states and has the spin $\frac{7}{2}$ state lying above the spin $\frac{3}{2}$ state.

During the quantisation procedure some cluster structure emerged. This brings the Skyrme model closer to the cluster models which are used widely in nuclear physics. The advantage of the Skyrme model is that the dynamics of the clusters are fully determined by the Skyrme Lagrangian. They can merge smoothly into the

$B = 7$ Skyrmion or be infinitely separated; our formalism naturally takes account of all configurations in between.

We predict that the excited spin $\frac{7}{2}$ state of $^7$Li is smaller than the spin $\frac{3}{2}$ ground state. The result depends crucially on the dodecahedral symmetry of the $B = 7$ Skyrmion. This symmetry appears to persist in modified Skyrme models except in extreme BPS models [16] [15]. Thus this prediction is an important signature for soliton models of finite nuclei.

Vibrational modes have the capacity to fix many issues in the Skyrme model including the high binding energies and small radii found using zero mode quantisation. They also have a fascinating and rich geometric structure. For these reasons alone, more work should be done to understand the vibrational spaces of Skyrmions. It is somewhat surprising that their inclusion leads to a resolution of problems in the $B = 7$ sector. Hopefully a similar analysis in other sectors can produce more surprises.

# Chapter 4

# A dynamical $\alpha$-cluster model of $^{16}$O

*This chapter is based on the calculation presented in the joint paper with C. King and N. S. Manton [41].*

The energy spectrum of the Oxygen-16 nucleus has posed a challenge to nuclear physicists for decades. Its ground state has spin-parity $0^+$, as does the first excited state at 6.05 MeV. We mention this excited state frequently and so we introduce the notation $0_e^+$ to refer to it. The fact that the two lowest energy states both have spin $0^+$ is unusual. Not many nuclei contain this feature in their spectrum and few models predict such states. There is a spin $3^-$ state at 6.1 MeV which is thought to lie on a rotational band with the ground state. The band also includes a spin $4^+$ state at 10.3 MeV. However, the band does not include a spin 2 state, hinting at some enhanced symmetry of the nucleus. Instead, the lowest energy spin $2^+$ state is at 6.9 MeV. There are many more states, around 100 are known up to 20 MeV, but knowledge of these low lying states suffices to describe the main theoretical work on the nucleus.

It was suggested in the 1930s that the nucleus could be described by four $\alpha$-particles arranged in a tetrahedron. This is the shape which maximises the number of short bonds between the particles. Wheeler [42] studied a point particle model localised around the tetrahedron. By looking at small fluctuations around this configuration he found a rich spectrum for the nucleus and a simple geometric interpretation of the states. For example, the ground state wavefunction is focused about the tetrahedron. We say that the ground state has a tetrahedral nature.

The shell model has also been used to describe the nucleus; the ground state of

Oxygen-16 is a doubly closed shell and so is spherically symmetric. Although the structure of the ground state in the shell model appears to contradict the tetrahedral configuration of Wheeler; Perring and Skyrme showed that they are in fact identical descriptions within a simple harmonic approximation [43] . Excitations in the shell model arise when individual nucleons are excited. The standard shell model struggles to describe the state $0_e^+$. Some studies [44] have shown that the state could be interpreted as a four-particle-four-hole configuration. Although this configuration has the correct spin-parity, its energy is much larger than 6.05 MeV [45]. In addition, the shell model cannot reproduce the large E3 transition rate between the low lying spin $3^-$ state and the ground state. This is part of a wider problem – the shell model struggles when collective behaviour becomes important. Elliott showed that one must factor out the center of mass coordinates to study collective behaviour in the shell model [46, 47]. This helped gain an understanding of some negative parity states of Oxygen-16 but the same model applied to positive parity states had limited success. A modern attempt [48] appears to do better, although the authors fail to find any $0^-$ or $3^+$ states, both of which exist in the low lying spectrum.

Recently, more fundamental models have been used to study the nucleus. These include the lattice ab initio model from Epelbaum et al. [49]. Here, individual nucleons interact via chiral effective field theory. Their degrees of freedom are positions on a lattice and the formalism uses powerful Monte Carlo methods to calculate an energy spectrum and allows the authors to probe the structure of each quantum state. They find that $\alpha$-clustering emerges from this single nucleon model. The ground state of the nucleus is dominated by the tetrahedral configuration - in agreement with other models. In contrast, the $0_e^+$ state looks more like a square arrangement of $\alpha$-particles. The authors also find that the first spin 2 state is square-like in nature, interpreting it as a rotational excitation of the spin $0_e^+$ state. We believe this interpretation is problematic. Suppose that the $0_e^+$ state and first $2^+$ state lie on a rotational band from the flat square while the $0^+$ and $3^-$ lie on a rotational band from the tetrahedron. Each band has a gradient associated to it and the ratio of these gradients is related to the relative sizes of the configurations. Hence, from the experimental energies we can calculate the size of the square compared to the tetrahedron. In a simple point particle approximation

the ratio of the third components of the moment of inertia tensor would be

$$\frac{V_{33}^{\text{square}}}{V_{33}^{tet}} \approx 3 \, , \qquad (4.1)$$

which seems unreasonably large; a flat square configuration of this size would likely be unbound. In addition, the lattice ab initio method requires large amounts of computation time, especially as energies get large. Negative parity also appears to pose a problem; only positive parity states up to 7 MeV have been discovered in the model.

Other modern models such as the antisymmetrised molecular dynamics model [50] also find these geometric cluster configurations arising from a more fundamental starting point. This fact, and the work discussed so far, suggests that the $\alpha$-cluster model is an essential tool for describing the $^{16}$O nucleus. As such, we shall now review the topic in more detail.

Dennison built on the pioneering work of Wheeler. In [51] he still describes the nucleus in a simple point particle model and considers harmonic oscillations around the tetrahedral configuration. In this work the $0_e^+$ state is identified as a breathing configuration – a vibrational mode which symmetrically stretches the tetrahedron. It also considers tunnelling energy - this is a contribution caused by a single $\alpha$-particle passing through the other three to form the dual tetrahedron. Sensibly, Dennison ignores the tunneling energy as the corresponding path in configuration space is of very high energy. However, we will show that a much shallower path to the dual tetrahedron exists. This will have a large effect on the low lying energy spectrum so should not be ignored. Later, Robson [52] confirmed that the $3^-$ state is a rotational excitation of the ground $0^+$ state by looking at electron scattering off the nucleus. Form factors between states in a rotational band are simply related, and Robson showed that the relation holds for these states.

Bauhoff et al. [10] used the cluster model to study the configuration space of four $\alpha$-particles. Using a variety of different forces between the particles, they looked for configurations which minimise the static energy of the system. This, alongside other calculations [53, 54], found several important configurations besides the tetrahedron. Namely, the flat square (as rediscovered by Epelbaum et al.), the bent square and the chain. The Skyrme model also reproduces these configurations [55]. Importantly, since a range of models and forces were used, the existence of these configurations appears robust. Bauhoff then quantised the

different configurations as rigid rotors, as was also done in the Skyrme model [56]. This method of quantisation works provided that the shapes are well separated in configuration space. But this is not true, explaining the poor match with experimental data found in these works. Further searches of $\alpha$-cluster configurations took place for nuclei with baryon number $4N$ [57, 58] showing that these methods are relevant for a wide range of nuclei.

Some authors attempted to improve the quantisation method described above. Bertsch and Bertozzi [59] included a one-dimensional family of deformed tetrahedra in their quantisation scheme - finding the $0_e^+$ state to be an admixture of configurations. Onishi and Sheline [60] considered a modified shell model with a tetrahedral potential, taking the structure of the ground state seriously. Bijker and Iachello showed that Wheeler and Dennison's simple model is a particular limit of the algebraic cluster model [66]. Like Dennison, they suggest the $0_e^+$ state is of a breathing nature. They also found an analytic expression for the transition rates between states [62]. The results are promising along the tetrahedral band, although they struggle to explain the transitions between states of different kinds, such as the spin 4 state (which is concentrated around the tetrahedron) and the spin 2 state (a vibrational excitation).

The Oxygen-16 nucleus has been examined by many theorists over the years. It appears evident that the $\alpha$-cluster model is vital to describe the nucleus and that the ground state is tetrahedral in nature. Excited states have been described by vibrations around the tetrahedron and alternatively as different shapes in the configuration space, such as the square. There is clear disagreement between the models. For example, Epelbaum et al. believe the $0_e^+$ state comes from a square configuration while Bijker and Iachello believe it is of a breathing nature. Our analysis will take account of vibrations around the tetrahedron and also include other important configurations such as the square. By including the important aspects of each model, we hope to clarify the nature of the $0_e^+$ state - and others.

## 4.1 The $B = 16$ sector of the Skyrme model

All known Skyrmions in the $B = 16$ sector can be described as a composition of four $B = 4$ Skyrmions. Due to its high classical binding energy, the cubic $B = 4$ Skyrmion can be used as a building block for larger Skyrmions [55], just as $\alpha$-

particles are used to construct large nuclei. Some important Skyrme configurations have the symmetries of a tetrahedron ($T_d$), square ($D_4$) and bent square ($D_2$). There is also a chain-like Skyrmion. These four configurations are displayed in Figure 4.1. In the standard Skyrme model the minimum energy configuration is the bent square, while the flat square is a local minumum and the tetrahedron is unstable. However, one may modify the model in a number of ways [15, 16] which may alter the energies of the configurations.
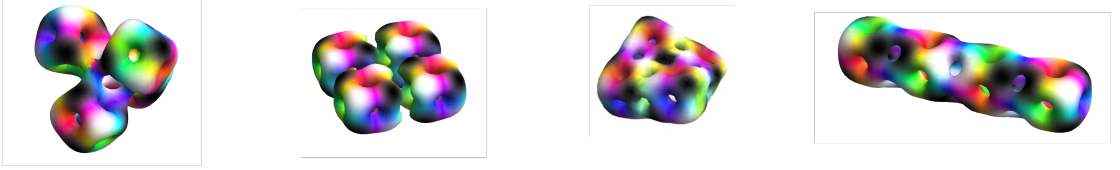


Figure 4.1: Four low energy configurations in the $B = 16$ sector.

The symmetries of each configuration give rise to constraints on the allowed quantum states of the system. In particular, the tetrahedral symmetry leads to the constraints

$$e^{\frac{2i\pi}{3\sqrt{3}}\left(\hat{L}_1+\hat{L}_2+\hat{L}_3\right)}e^{\frac{2i\pi}{3\sqrt{3}}\left(\hat{K}_1+\hat{K}_2+\hat{K}_3\right)}\Psi = \Psi \tag{4.2}$$

$$e^{i\pi\hat{L}_3}\Psi = \Psi\,, \tag{4.3}$$

where $\Psi$ is the wavefunction on some configuration space. The flat square has $D_4$ symmetry resulting in

$$e^{\frac{i\pi}{2}\hat{L}_3}e^{i\pi\hat{K}_1}\Psi = \Psi \tag{4.4}$$

$$e^{i\pi\hat{L}_1}\Psi = \Psi\,. \tag{4.5}$$

The chain also obeys these constraints when aligned appropriately. Finally, the bent square is the least restrictive shape with constraints encoding the $D_2$ symmetry as follows

$$e^{i\pi\hat{L}_3}\Psi = \Psi \tag{4.6}$$

$$e^{i\pi\hat{L}_1}\Psi = \Psi\,. \tag{4.7}$$

If one were to apply rigid body quantisation to each of these configurations, the constraints would give rise to a set of allowed spin states. These states, for each

| $J$ | Tetrahedron | Square | Bent Square |
|---|---|---|---|
| 0 | $\lvert 0,0\rangle$ | $\lvert 0,0\rangle$ | $\lvert 0,0\rangle$ |
| 2 | | $\lvert 2,0\rangle$ | $\lvert 2,0\rangle$ |
| | | | $\lvert 2,2\rangle + \lvert 2,-2\rangle$ |
| 3 | $\lvert 3,2\rangle - \lvert 3,-2\rangle$ | | $\lvert 3,2\rangle - \lvert 3,-2\rangle$ |
| 4 | | $\lvert 4,0\rangle$ | $\lvert 4,0\rangle$ |
| | $\lvert 4,4\rangle + \sqrt{\frac{14}{5}}\,\lvert 4,0\rangle + \lvert 4,-4\rangle$ | $\lvert 4,4\rangle + \lvert 4,-4\rangle$ | $\lvert 4,2\rangle + \lvert 4,-2\rangle$ |
| | | | $\lvert 4,4\rangle + \lvert 4,-4\rangle$ |
| 5 | | $\lvert 5,4\rangle - \lvert 5,-4\rangle$ | $\lvert 5,2\rangle - \lvert 5,2\rangle$ |
| | | | $\lvert 5,4\rangle - \lvert 5,-4\rangle$ |
| 6 | | | $\lvert 6,0\rangle$ |
| | $\lvert 6,4\rangle - \sqrt{\frac{2}{7}}\,\lvert 6,0\rangle + \lvert 6,-4\rangle$ | $\lvert 6,0\rangle$ | $\lvert 6,2\rangle + \lvert 6,-2\rangle$ |
| | $\sqrt{\frac{5}{11}}\,\lvert 6,6\rangle - \lvert 6,2\rangle - \lvert 6,-2\rangle + \sqrt{\frac{5}{11}}\,\lvert 6,-6\rangle$ | $\lvert 6,4\rangle + \lvert 6,-4\rangle$ | $\lvert 6,4\rangle + \lvert 6,-4\rangle$ |
| | | | $\lvert 6,6\rangle + \lvert 6,-6\rangle$ |

Table 4.1: The allowed rigid body spin states at each $B = 16$ Skyrmion for isospin 0.

shape, are given in Table 4.1 up to spin 6. We have set isospin equal to zero for now.

We shall not use rigid body quantisation in this Chapter but whatever we do must still be consistent with a rigid body analysis. Note that the tetrahedral Skyrme configuration does not allow a spin 2 state while the square Skyrmion does not allow a spin 3 state. Hence the wavefunctions describing these states will have different structures and to compare them, one must consider a configuration space which contains both the tetrahedral and square configurations. This is why rigid body quantisation is not sufficient to describe the low-lying energy spectrum in the $B = 16$ sector.

## 4.2 The vibrational manifold

We will consider the vibrational manifold containing the configurations described by four $B = 4$ Skyrmions. We do not take account of the internal structure of each cube. So, given the positions of the four particles, they are each rotated to minimise energy. Physically, we assume the $\alpha$-particles are in their ground states. The analysis ignores single particle excitations and will not be able to describe physical states which arise from these. Single particle excitations of the $\alpha$-particle are of order 20 MeV which is higher energy than the states we consider in this model.

The degrees of freedom of the vibrational manifold are the positions of the clusters along with the global isorotations of the overall Skyrme configuration, giving a 15-dimensional manifold. We cannot hope to quantise the system exactly on such a large space. Instead we concentrate mostly on the configurations near the tetrahedron. Here, the vibrational manifold separates into three submanifolds labelled by the irreducible representations (irreps) of the tetrahedral group: the $A$, $E$ and $F$ representations. These can be physically realised as follows:

- The $A$ vibration. All particles move in or out symmetrically, stretching the tetrahedron but keeping its symmetry. This is often referred to as the breathing mode.

- The $E$ vibration. This two-dimensional manifold includes a mode where the two uppermost particles move down while the other two move up, making a deformed tetrahedron with $D_2$ symmetry. There are three of these modes, since there are three ways to pair the $\alpha$-particles, but exciting all three modes equally leaves the original configuration unchanged. Hence the manifold is two-dimensional. We will study the vibration far beyond the local analysis discussed here.

- The $F$ vibration. The final irrep is three-dimensional and its manifold includes a mode where one particle moves away from the other three while the overall configuration retains $C_3$ symmetry. A thorough study of this vibration could lead to an understanding of the decay process

$$^{16}\mathrm{O} \rightarrow {}^{12}\mathrm{C} + \alpha\,. \tag{4.8}$$

The union of these three submanifolds gives a six-dimensional space. The remaining nine dimensions are simply the zero modes: global translations, rotations and isorotations.

Labelling the submanifolds by their representations the total vibrational manifold decomposes into

$$\mathcal{M} = \mathcal{M}_A \times \mathcal{M}_E \times \mathcal{M}_F \,, \tag{4.9}$$

which is valid near the tetrahedron, where the problem is linear. The global structure of $\mathcal{M}$ is more complicated. The total space is a principle bundle with base space $\mathcal{M}$, fibred by $SO(3)_J \times SO(3)_I \times \mathbb{R}^3$. From now on, translations are neglected. We study each of the submanifolds in turn. The most novel aspect of the work is contained in our description of the $E$ vibration. We begin with this.

## 4.3   The $E$ vibration

The global structure of $\mathcal{M}_E$ is studied by considering a special dynamical mode which connects the tetrahedron, bent square and flat square. It is shown in Figure 4.2. Initially, two $B = 8$ Skyrmions are boosted towards each other in an attractive channel. They deform as they approach and briefly form the tetrahedron which then flattens out. The Skyrmions scatter through the bent square and the flat square before continuing on to form the dual bent square and dual tetrahedron. Finally, the two $B = 8$ Skyrmions emerge, rotated 90° compared to the initial configuration. It is somewhat analogous to the twisted line scattering in the $B = 3$ sector [28] with the flat square playing the role of the $B = 3$ torus.
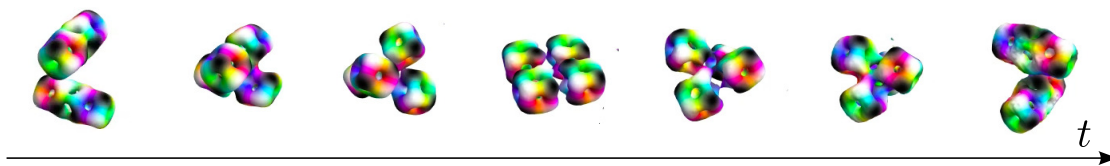


Figure 4.2: The dynamical mode used to construct $\mathcal{M}_E$.

The full dynamical mode displayed in Figure 4.2 describes the extension of the small-amplitude mode of the $E$ vibration described in [42, 51]. Thus, the manifold $\mathcal{M}_E$, which should contain configurations beyond local perturbations, should contain this full dynamical mode, including the asymptotics. One may pull the

tetrahedron into two $B = 8$ Skyrmions in three different ways. Hence $\mathcal{M}_E$ is a surface which stretches out in six directions, like the surface displayed in Figure 4.3. Each configuration on this surface has $D_2$ symmetry meaning that if one $\alpha$-particle is at $\boldsymbol{x} = (x, y, z)$, the others are at $(x, -y, -z), (-x, y, -z)$ and $(-x, -y, z)$. The total space we study in this section is $\mathcal{M}_E$ fibred by $SO(3)_J \times SO(3)_I$. There are certain transformations which leave the total space invariant. These are made from two individual transformations; one on the base space $\mathcal{M}_E$ and one which is a rotation-isorotation pair acting on the Skyrme configuration. For example, one may apply the transformation $(x, y, z) \to (y, -x, z)$ to the particles on $\mathcal{M}_E$. This is undone by a $\frac{\pi}{2}$ rotation around the $z$-axis followed by a $\pi$ isorotation applied to the Skyrme configuration. The wavefunctions we consider must transform trivially under the combined action, these will satisfy the FR constraints everywhere on $\mathcal{M}_E$. The $D_2$ symmetries are simply actions on $\mathcal{M}_E$ and do not require a rotation-isorotation transformation to undo. Moreover the wavefunctions transform trivially under the $D_2$ symmetries. Hence we may focus on one quarter of the surface which we denote $\mathcal{M}_q$.
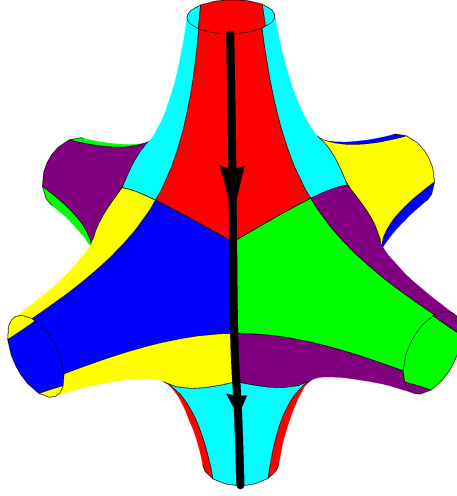


Figure 4.3: A candidate manifold to describe $\mathcal{M}_E$. Regions of the same colour are related by $D_2$ symmetry. The scattering mode displayed in Figure (4.2) is represented by the thick black line.

To calculate physical observables of the system we must first solve the Schrödinger

equation

$$\left(-\frac{\hbar^2}{2}\Delta + V(\boldsymbol{x})\right)\Psi = E\Psi\,, \tag{4.10}$$

where $\Delta$ is the kinetic operator on $\mathcal{M}_q \times SO(3)_J \times SO(3)_I$ and $V(\boldsymbol{x})$ is the potential energy on $\mathcal{M}_q$, equal to the static energy of the Skyrme configuration at $\boldsymbol{x}$. To solve (4.10), a better understanding of $\Delta$ and $V(\boldsymbol{x})$ is required.

## 4.3.1 The kinetic operator

The kinetic operator can be understood in terms of the metric on the total space. The classical kinetic energy must respect the symmetries of the problem which helps to simplify the metric. The $D_2$ symmetry implies that the kinetic energy cannot be linear in $\boldsymbol{x}$. Thus, the metric must be block diagonal and the operator $\Delta$ separates into two parts: one which acts only via vibrational coordinates and another which acts only via rotational and isorotational coordinates. We denote this as

$$\Delta = \Delta_{\boldsymbol{x}} + \nabla^2\,, \tag{4.11}$$

where $\Delta_{\boldsymbol{x}}$ is the operator on $\mathcal{M}_q$ while $\nabla^2$ is the usual Laplacian on the combined rotational and isorotational space. We model the metric on the manifold by approximating $\mathcal{M}_E$ as the 6-punctured sphere with constant negative curvature. This captures several important physical features such as the fact that the manifold should stretch to infinity asymptotically in six directions and that the curvature is non-positive everywhere on $\mathcal{M}_E$.

An $n$-punctured sphere, with $n \geq 3$ is conformally equivalent to a subset of the complex upper half plane (UHP). Often the mapping is highly complicated and analytically intractable. However, the large amount of symmetry in our problem allows us to find the map explicitly. Defining the complex coordinate on the subset $\mathcal{F} \in \mathbb{C}$ as $\zeta = \eta + i\epsilon$, we can write the map from $\mathcal{F}$ to the Riemann sphere, with coordinates $\hat{\boldsymbol{x}} = (\hat{x}, \hat{y}, \hat{z})$, as

$$(\hat{x}, \hat{y}, \hat{z}) = |H(\zeta)|^{-2}\left(2\mathrm{Re}\left[H(\zeta)\right], 2\mathrm{Im}\left[H(\zeta)\right], 1 - |H(\zeta)|^2\right)\,, \tag{4.12}$$

where

$$H(\zeta) = \left(\frac{\Theta(0,3,\zeta)}{\Theta(1,3,\zeta)}\right) \tag{4.13}$$

67

and

$$\Theta(a, n, \zeta) = \exp\left(2\pi i\left(\frac{1}{8}a^2\zeta + \frac{1}{8}a\right)\right)\tilde{\theta}_n\left(\pi\left(\frac{1}{4} + \frac{a\zeta}{2}\right), \exp\left(i\pi\zeta\right)\right) \qquad (4.14)$$

and $\tilde{\theta}_n$ are the Jacobi theta functions [63]. There is then a bijection between the Riemann sphere and $\mathcal{M}_E$. The conformal equivalence between $\mathcal{M}_q$ and $\mathcal{F}$ is shown graphically in Figure 4.4. We have chosen a particular fundamental domain of the complex plane. There are infinitely many other choices but the wavefunctions will satisfy certain constraints along the boundaries of the domain. Hence, it is helpful to make a choice with as simple boundaries as possible.
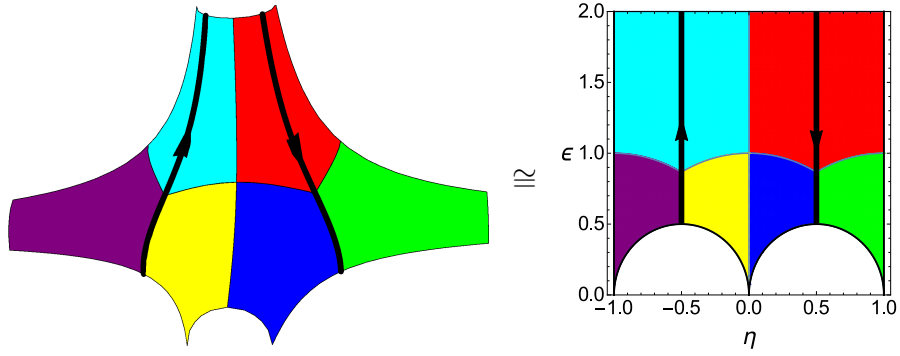


Figure 4.4: The relation between $\mathcal{M}_q$ (left) and $\mathcal{F}$ (right). Tetrahedral configurations are at the points where three coloured regions meet while the square configurations are at points where four coloured regions meet. The scattering mode from Figure 4.2 is represented by the thick black lines.

In terms of the coordinates on $\mathcal{F}$, the metric simplifies considerably. The kinetic operator is

$$-\Delta_{\boldsymbol{x}} = -\epsilon^2\left(\frac{\partial^2}{\partial\eta^2} + \frac{\partial^2}{\partial\epsilon^2}\right), \qquad (4.15)$$

which is invariant under any Möbius transformation of $\zeta$. The Schrödinger equation becomes

$$\left(-\frac{\hbar^2}{2}\epsilon^2\left(\frac{\partial^2}{\partial\eta^2} + \frac{\partial^2}{\partial\epsilon^2}\right) - \frac{\hbar^2}{2}\nabla^2 + V(\epsilon, \eta)\right)\Psi = E\Psi. \qquad (4.16)$$

The problem is separable into vibrational and rotational parts. The rotational wavefunctions are solutions to the rigid body problem. Hence we may write the

68

total wavefunction as

$$\Psi = \sum_{L_3, K_3} \phi_{L_3, K_3}(\zeta) \left| J, L_3 \right\rangle \left| I, K_3 \right\rangle , \tag{4.17}$$

where the $J_3$ and $I_3$ labels have been suppressed since they do not affect the energy of the state. The vibrational wavefunctions $\phi$ satisfy

$$\left( -\frac{\hbar^2}{2} \epsilon^2 \left( \frac{\partial^2}{\partial \eta^2} + \frac{\partial^2}{\partial \epsilon^2} \right) + E_{L_3, K_3}(\epsilon, \eta) + V(\epsilon, \eta) \right) \phi_{L_3, K_3} = E \phi_{L_3, K_3} , \tag{4.18}$$

where $E_{L_3, K_3}(\epsilon, \eta)$ satisfies

$$-\frac{\hbar^2}{2} \nabla^2 \left| J, L_3 \right\rangle \left| I, K_3 \right\rangle = E_{L_3, K_3}(\epsilon, \eta) \left| J, L_3 \right\rangle \left| I, K_3 \right\rangle . \tag{4.19}$$

The $E_{L_3, K_3}$ contribution is difficult to include in full. Instead we write

$$E_J(s) = \frac{\hbar^2}{2 \Lambda_{\text{tet}}} J(J+1) + E_J^{(1)}(\epsilon, \eta) , \tag{4.20}$$

and neglect $E_J^{(1)}$ for now. We will reinstate it later using perturbation theory, which relies on $E_J^{(1)}$ being small. It is zero at the tetrahedron and small nearby. Hence we have more confidence in this approximation for vibrational wavefunctions which are concentrated near the tetrahedron. With this approximation, the vibrational problem becomes

$$\left( -\frac{\hbar^2}{2} \epsilon^2 \left( \frac{\partial^2}{\partial \eta^2} + \frac{\partial^2}{\partial \epsilon^2} \right) + V(\epsilon, \eta) \right) \phi = \lambda \phi , \tag{4.21}$$

where we have defined the vibrational energy $\lambda$. To solve (4.21) we must find boundary conditions for $\phi$; these depend on the representation that $\phi$ falls into. To understand the representations we must first understand the symmetries of $\mathcal{F}$ in more detail.

## 4.3.2 Symmetries of $\mathcal{F}$ and $\mathcal{M}_q$

The six-punctured sphere has the symmetry group of an octahedron, $O$. Hence the quarter sphere $\mathcal{M}_q$ has the symmetry group $O/D_2 \cong S_3$, the permutation group of three objects: in this case the unorientated $x$, $y$ and $z$ axes. The elements of $S_3$ can act on the positions of the $\alpha$-particles, $\boldsymbol{x} \in \mathcal{M}_q$. These descend to

transformations on $\mathcal{F}$ which are Möbius maps. Each of these transformations on the base space $\mathcal{M}_q$ has an equivalent description as a transformation on the fibre. These are rotation-isorotation pairs which act on the Skyrme configurations. The explicit rotation-isorotation pairs and Möbius maps are displayed in Table 4.2 for each element of $S_3$. Note that the rotations are not unique since the system is invariant under rotations by $\pi$ about each axis. The isorotations depend on the Skyrme configuration's internal structure and how this changes over the manifold. For example, the flat square at $\eta = \epsilon = \frac{1}{2}$ lies in the $x$-$y$ plane. It has red on the face perpendicular to the $C_4$ symmetry axis. In contrast, the flat square at $\eta = 0$, $\epsilon = 1$ lies in the $y$-$z$ plane and has green on the $C_4$ symmetry face.

In addition, inversion corresponds to the operation $\boldsymbol{x} \to -\boldsymbol{x}$ on $\mathcal{M}_E$ followed by a $\pi$ iso-rotation about $(0, 0, 1)$. In terms of the coordinates on $\mathcal{F}$ this inversion is equal to the transformation $\zeta \to -\zeta^\dagger$, which is equivalent to $\eta \to -\eta$. The inversion operator allows us to calculate the parity of a vibrational wavefunction

$$\hat{\mathcal{P}}\phi(\zeta) = \phi(-\zeta^\dagger) = P\phi(\zeta)\,, \tag{4.22}$$

where we call $\hat{\mathcal{P}}$ the parity operator on the vibrational space and $P$ the parity.

The group $S_3$ has three irreps called the trivial, sign and standard irreps. Provided the potential is invariant under all elements of $S_3$, as it should be physically, the vibrational wavefunctions can be labelled by the representation that they fall into, as well as parity. Depending on its representation and parity, the vibrational wavefunctions will have different boundary conditions.

Vibrational wavefunctions in the trivial irrep, denoted $\phi_t$, are invariant under any element of $S_3$. Hence for any Möbius transformation $M$ listed in the third column of Table 4.2, we have that

$$\phi_t(\zeta) = \phi_t(M(\zeta))\,. \tag{4.23}$$

This relationship can be used to find boundary conditions for $\phi_t$. Consider the points $\zeta_+$ and $\zeta_-$, lying either side of the curve $C$ as in Figure 4.5. These are related by a Möbius transformation followed by a parity operation. Explicitly

$$\zeta_+ = M_{(1,3)}(\zeta_0) = -\frac{1}{\zeta_0} = -\frac{1}{\left(-\zeta_-^\dagger\right)} = \frac{1}{\zeta_-^\dagger}\,. \tag{4.24}$$

| $S_3$ element | Rotation and isorotation pair | Möbius map |
|---|---|---|
| $(1,2)$ | $\frac{\pi}{2}$ about $(0,0,1)$<br>$\pi$ about $(1,0,0)$ | $\zeta \to \zeta - 1$ |
| $(1,3)$ | $\frac{\pi}{2}$ about $(0,1,0)$<br>$\pi$ about $(\cos(2\pi/3), \sin(2\pi/3), 0)$ | $\zeta \to -\frac{1}{\zeta}$ |
| $(2,3)$ | $\frac{\pi}{2}$ about $(1,0,0)$<br>$\pi$ about $(0,0,1)$ | $\zeta \to \frac{\zeta}{1-\zeta}$ |
| $(1,2,3)$ | $\frac{2\pi}{3}$ about $(1,1,1)$<br>$\frac{2\pi}{3}$ about $(0,0,1)$ | $\zeta \to \frac{1}{1-\zeta}$ |
| $(1,3,2)$ | $\frac{4\pi}{3}$ about $(1,1,1)$<br>$\frac{4\pi}{3}$ about $(0,0,1)$ | $\zeta \to \frac{\zeta-1}{\zeta}$ |

Table 4.2: The elements of the symmetry group $S_3$ and how they act on $\mathcal{M}_q$ and $\mathcal{F}$.

These relations are detailed graphically in Figure 4.5. From this we deduce that the wavefunction at these points is related by

$$\phi_t(\zeta_+) = \phi_t\left(\frac{1}{\zeta_0}\right) = \phi_t(\zeta_0) = \phi_t(-\zeta_-^\dagger) = P\phi_t(\zeta_-) , \qquad (4.25)$$

where we have used the fact that $\phi_t$ is in the trivial irrep in the second equality and applied the parity operator in the fourth equality. Taking the limit where the points $\zeta_+$ and $\zeta_-$ tend towards the curve $C$, we find that

$$\partial_\perp \phi_t(\zeta_c) = 0 \text{ for positive parity} \qquad (4.26)$$
$$\phi_t(\zeta_c) = 0 \text{ for negative parity,} \qquad (4.27)$$

where $\zeta_c \in C$ and $\partial_\perp$ means the derivative perpendicular to $C$.

The analysis is similar for wavefunctions in the sign irrep, which are denoted $\phi_s$. Here, the wavefunction is invariant under 3-cycles but changes sign under transpositions. Hence (4.25) becomes

$$\phi_s(\zeta_+) = \phi_s\left(\frac{1}{\zeta_0}\right) = -\phi_s(\zeta_0) = -\phi_s(-\zeta_-^\dagger) = -P\phi_s(\zeta_-) , \qquad (4.28)$$
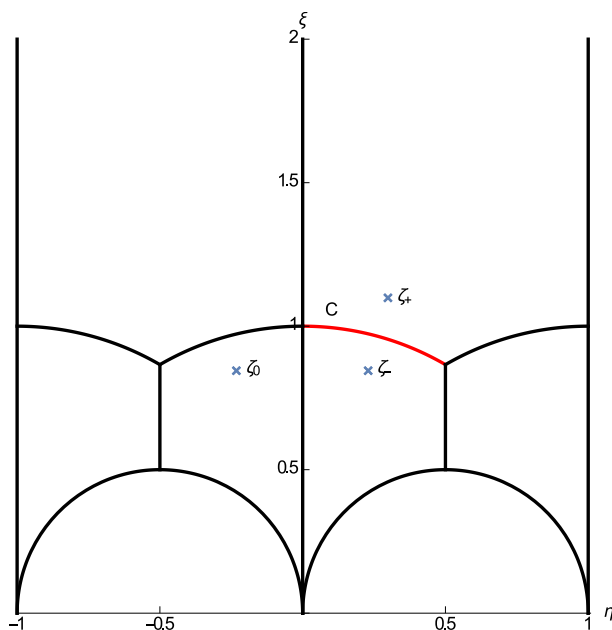
Figure 4.5: The points $\zeta_+$, $\zeta_-$ and $\zeta_0$ which are related by Möbius maps and the parity transform. The curve $C$ is drawn in red.

and the boundary conditions are

$$\phi_s(\zeta_c) = 0 \text{ for positive parity} \tag{4.29}$$
$$\partial_\perp \phi_s(\zeta_c) = 0 \text{ for negative parity.}$$

The standard irrep is two-dimensional and hence more complicated. It is most easily viewed using the three-dimensional natural representation. Here, the three objects permuted by $S_3$ are the wavefunctions, which are labelled $u$, $v$ and $w$. For example, the wavefunctions cycle as

$$u \to v \to w \to u. \tag{4.30}$$

under the transformation $(123)$. This three-dimensional basis of wavefunctions contains a trivial one-dimensional subspace since $u + v + w$ transforms trivially under all elements of $S_3$. We may recover the two-dimensional standard irrep by fixing the constraint

$$u + v + w = 0. \tag{4.31}$$

The boundary conditions are simplest for certain combinations of the wavefunctions. For example

$$(u + w)(\zeta_+) = (u + w)\left(\frac{1}{\zeta_0}\right) = (w + u)(\zeta_0) = \hat{P}(w + u)(\zeta_-) , \qquad (4.32)$$

and

$$(u - w)(\zeta_+) = (u - w)\left(\frac{1}{\zeta_0}\right) = (w - u)(\zeta_0) = -\hat{P}(u - w)(\zeta_-) . \qquad (4.33)$$

These two boundary conditions are enough to find all solutions of (4.21) which transform as the standard irrep. Note that knowing $u + w$ and $u - w$ is enough to reconstruct $u$, $v$ and $w$. The boundary conditions for each representation are summarised in Table 4.3. In addition, a wavefunction with negative parity must vanish along the boundary lines $\eta = -1, 0, 1$ while a positive parity wavefunction has vanishing derivative along these. Overall there are six different types of solution and searching for wavefunctions obeying each of these boundary conditions generates all possible vibrational wavefunctions.

| Representation | Parity | Boundary condition on $\mathcal{C}$ |
|---|---|---|
| Trivial | $+$ | $\partial_\perp \phi_t = 0$ |
| Trivial | $-$ | $\phi_t = 0$ |
| Sign | $+$ | $\phi_s = 0$ |
| Sign | $-$ | $\partial_\perp \phi_s = 0$ |
| Standard | $+$ | $\partial_\perp (u + w) = 0$ |
| | | $u - w = 0$ |
| Standard | $-$ | $u + w = 0$ |
| | | $\partial_\perp (u - w) = 0$ |

Table 4.3: A summary of the possible boundary conditions for the vibrational wavefunctions.

### 4.3.3 The potential

The representation theory and boundary conditions discussed so far do not depend on a choice of potential. To calculate an energy spectrum of the model, we must

choose a specific potential. One approach would be to take the static Skyrme configuration energy at each point on $\mathcal{M}_E$. There are two problems with this approach. First, it is only known how to generate certain Skyrme configurations such as the tetrahedron. The approach requires an ansatz on the whole of $\mathcal{M}_E$, which does not currently exist. Secondly, the basic Skyrme model can be modified in many ways. For example, by including a $6^{\text{th}}$ order term in the Lagrangian [15], altering the Skyrme potential [16] or including Coulomb effects. All these modifications will lead to changes in the energy of each configuration. So, even if we could generate all Skyrme configurations on $\mathcal{M}_E$, their energies are not robust to changes in the model. However, the discrete symmetries of the Skyrmions and their dynamics will not change provided the modifications are modest. Hence we trust the broad ideas from the Skyrme model, such as the symmetries and structure of $\mathcal{M}_E$, but not the details of the potential on the space of configurations.

Instead, we choose a potential which can be solved easily. Cluster models [10] suggest the tetrahedral configuration should have the lowest energy and so we put the minimum of the potential there. The square has higher energy and the asymptotic configurations higher still. A potential which captures these features is

$$V(\epsilon, \eta) = \epsilon^2 \left( \frac{1}{2}\omega^2 \left( \eta - \frac{1}{2} \right)^2 + \mu^2 \right) , \tag{4.34}$$

where $\omega$ and $\mu$ are parameters. The expression is only valid in the red region of $\mathcal{F}$, as displayed in Figure 4.4. The potential is extended into the other regions by applying the appropriate Möbius maps detailed in Table 4.2. We choose $\omega = \sqrt{6}$ and $\mu = 8\sqrt{2}$ which gives an energy gap between the tetrahedral and square configurations of 6.55 MeV, close to the values in [10]. However, note that the potential is not smooth at the boundaries between coloured regions. Further, it diverges asymptotically while it should actually flatten out. Our focus is on the low lying states of $^{16}$O which will be concentrated near the low energy configurations. The asymptotic divergence is a bigger problem if one were to study scattering states.

### 4.3.4 Finding solutions

With the choice of potential (4.34) the Schrödinger equation (4.21) becomes

$$-\frac{\hbar^2}{2}\epsilon^2\left(\frac{\partial^2}{\partial\eta^2}+\frac{\partial^2}{\partial\epsilon^2}\right)\phi+\epsilon^2\left(\frac{1}{2}\omega^2\left(\eta-\frac{1}{2}\right)^2+\mu^2\right)\phi=\lambda\phi\,,\qquad(4.35)$$

which can be solved using separation of variables

$$\phi(\eta,\epsilon)=\sum_n X_n(\eta)Y_n(\epsilon)\sqrt{\epsilon}\,.\qquad(4.36)$$

The problem only needs to be solved in one region of $\mathcal{F}$, such as the red region, and then the maps of Table 4.2 may be used to extrapolate the solution to the other regions. We do the calculation on the red region. For $\eta\in[0,1]$, the $X_n$ satisfy

$$\left(-\frac{\hbar^2}{2}\frac{d^2}{d\eta^2}+\frac{1}{2}\omega^2\left(\eta-\frac{1}{2}\right)^2+\mu^2\right)X_n(\eta)=e_nX_n(\eta)\,,\qquad(4.37)$$

with $X'_n(0)=X'_n(1)=0$ or $X_n(0)=X_n(1)=0$ for even and odd parity respectively. The boundary conditions give a constraint on $e_n$, leading to a discrete spectrum. The solutions are known analytically and can be expressed in terms of confluent hypergeometric functions. For $\omega,\mu=0$ the solutions simplify to $\cos\left(n\pi\left(\eta-\frac{1}{2}\right)\right)$ and $\sin\left(n\pi\left(\eta-\frac{1}{2}\right)\right)$ with $e_n=\frac{\hbar^2 n^2\pi^2}{2}$. We can substitute the $X_n$ into (4.35) to find an equation for the $Y_n$,

$$\left(-\epsilon'^2\frac{d^2}{d\epsilon'^2}-\epsilon'\frac{d}{d\epsilon'}+\left(\epsilon'^2+R^2\right)\right)Y_n(\epsilon')=0\,.\qquad(4.38)$$

This is a modified Bessel equation with $\epsilon'=\sqrt{e_n}\epsilon$. We have introduced $R$ which is related to the total eigenvalue as

$$\lambda=\frac{1}{4}+R^2\,.\qquad(4.39)$$

Overall, solutions to the Schrödinger equation (4.35) take the form

$$\phi\left(\eta+\frac{1}{2},\epsilon\right)=\sum_n^\infty a_{2n}\,_1F_1\left(\frac{1-(e_{2n}-\mu^2)/\omega}{4};\frac{1}{2};\omega\eta^2\right)e^{-\frac{1}{2}\omega\eta^2}K_{iR}\left(\sqrt{e_{2n}}\epsilon\right)\sqrt{\epsilon}$$

$$+\sum_n^\infty a_{2n+1}\eta\,_1F_1\left(\frac{3-(e_{2n+1}-\mu^2)/\omega}{4};\frac{3}{2};\omega\eta^2\right)e^{-\frac{1}{2}\omega\eta^2}K_{iR}\left(\sqrt{e_{2n+1}}\epsilon\right)\sqrt{\epsilon}\,,$$

$$(4.40)$$

where $_1F_1(a;b;z)$ is a confluent hypergeometric function and $K_\alpha(x)$ is the exponentially decaying modified Bessel function. The first sum contains even parity solutions while the second contains the odd parity ones.

Ignoring the boundary conditions derived in Section 4.3.2, the wavefunction (4.40) is a solution for all coefficients $a_n$ and all eigenvalues $R$. However, the boundary conditions restrict the allowed values. In practice, one chooses a value of $R$ and then tries to satisfy the boundary condition by adjusting the coefficients. This is done by enforcing the constraint on a finite number of points along the curve $C$. This gives a set of test coefficients. The same calculation is repeated using a different set of points. If the newly derived coefficients are different to the test ones then neither set enforces the boundary condition across the whole of $C$ and this value of $R$ is discarded. Numerically we restrict the upper limit of the series to some integer $N$ which is valid because $K_{iR}\left(\sqrt{e_n}\epsilon\right) \sim e^{-\sqrt{e_n}\epsilon}$ as $\epsilon \to \infty$ and $e_n \to \infty$ as $n \to \infty$. We then enforce the constraint at two sets of $N$ points along the boundary curve $C$, which reduces the problem to finding two null eigenvectors of two $N \times N$ matrices. A true eigenvalue $R$ occurs if these eigenvectors are equal.

The lowest energy numerically generated vibrational wavefunctions are displayed in Figure 4.6.

**Parity**

Parity on the vibrational manifold corresponds to the transformation $\zeta \to -\zeta^\dagger$, as previously discussed. There is also a way to calculate parity in a rigid body analysis. There, the parity operator for a Skyrme field configuration $\boldsymbol{\pi}(\boldsymbol{x})$ is

$$\hat{\mathcal{P}}_{\mathrm{RB}} : \boldsymbol{\pi}(\boldsymbol{x}) \to -\boldsymbol{\pi}(-\boldsymbol{x}). \tag{4.41}$$

If the Skyrme configuration has a reflection symmetry, the parity operator is equivalent to some rotation-isorotation operator $\hat{R}_p$. One can then find the parity of the state by applying $\hat{R}_p$ to the rigid body wavefunction. We call this the intrinsic parity of a Skyrme configuration for a given spin. For example, the tetrahedron has positive intrinsic parity for spin 0 and negative intrinsic parity for spin 3. The flat square has positive intrinsic parity for all even spins. Note that states with no reflection symmetry have no intrinsic parity. We shall make sure that our notion of parity on the vibrational manifold is consistent with the intrinsic parity while we construct the rovibrational states.

$\phi^{(a)}$     $\phi^{(b)}$     $\phi^{(c)}$     $\phi^{(d)}$

$\phi^{(e)}$     $\phi^{(f)}$     $\phi^{(g)}$     $\phi^{(h)}$

$u^{(i)} - v^{(i)}$ and $u^{(i)} + v^{(i)}$    $u^{(j)} - v^{(j)}$ and $u^{(j)} + v^{(j)}$    $u^{(k)} - v^{(k)}$ and $u^{(k)} + v^{(k)}$

$u^{(l)} - v^{(l)}$ and $u^{(l)} + v^{(l)}$    $u^{(m)} - v^{(m)}$ and $u^{(m)} + v^{(m)}$    $u^{(n)} - v^{(n)}$ and $u^{(n)} + v^{(n)}$
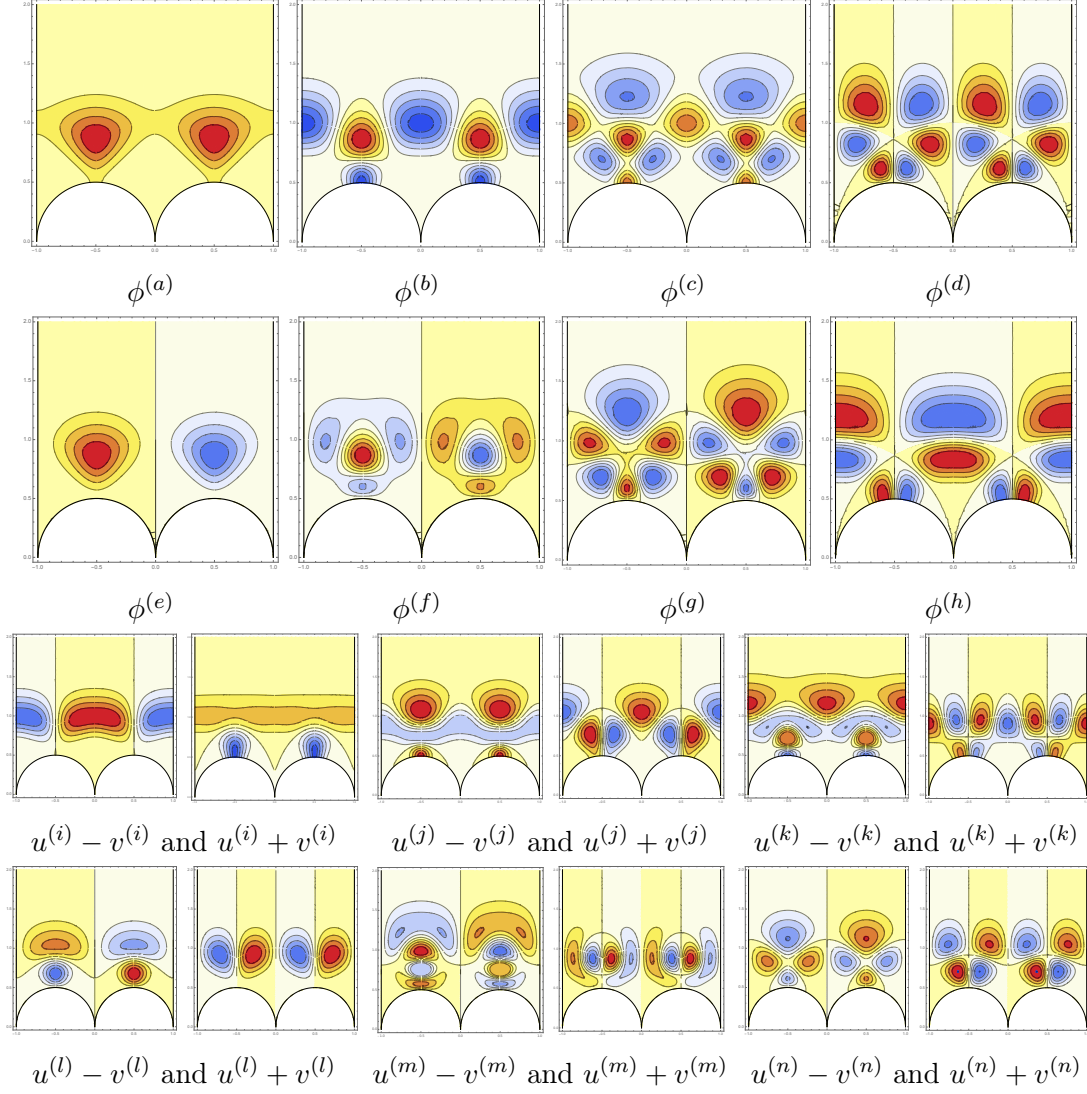
Figure 4.6: The vibrational wavefunctions on $\mathcal{F}$. The plots show the wavefunction contours from -1 (blue) to +1 (red). Each row contains a different type of vibrational wavefunction. From top to bottom the wavefunctions fall into the trivial, sign, standard with positive parity and standard with negative parity irreps. The wavefunctions are scaled for clarity.

### 4.3.5 Rovibrational wavefunctions

We now have enough information to construct rovibrational states. The symmetries of $\mathcal{M}_q$ each have an equivalent rotation-isorotation transformation, as was displayed in Table 4.2. The rovibrational states should transform in the same way under either transformation. This restriction provides constraints on the allowed spin states for a given vibrational wavefunction. Specifically, the constraints depend on the representation of the wavefunction.

Rovibrational states in the trivial or sign representation are rather simple. For vibrational wavefunctions in the trivial irrep the corresponding spin states must transform trivially under all rotations detailed in Table 4.2. These are the states which transform trivially under all elements of the tetrahedral group. The spin states which can be combined with sign irrep vibrational wavefunctions pick up a sign under transposition. Overall, these two possibilities include all tetrahedrally symmetric spin states, which were calculated and displayed in Table 4.1. States with positive (negative) intrinsic parity can be combined with trivial (sign) irrep vibrational wavefunctions. The lowest energy rovibrational states of this kind have zero isospin; the first three are

$$
\begin{aligned}
&\phi^{(a)} \left| 0, 0 \right\rangle \\
&\phi^{(e)} \left( \left| 3, 2 \right\rangle - \left| 3, -2 \right\rangle \right) \\
&\phi^{(a)} \left( \left| 4, 4 \right\rangle + \sqrt{\frac{14}{5}} \left| 4, 0 \right\rangle + \left| 4, -4 \right\rangle \right),
\end{aligned} \tag{4.42}
$$

where we have neglected to write the isospin part of the wavefunction, since it is trivial in this case. The index of the vibrational wavefunctions refer to the specific solutions displayed in Figure 4.6. The three wavefunctions (4.42) are concentrated around the tetrahedron and hence are analogous to the states obtained in rigid body quantisation. In the rigid body case, the states form an exact rotational band. In the vibrational scheme, the odd parity vibrational wavefunction $\phi^{(e)}$ has slightly higher energy than its even parity counterpart $\phi^{(a)}$ as it is more constrained. Hence in our model the states will only form an approximate rotational band. Note that $\phi^{(e)}$ vanishes at all flat square configurations. It must do so, as the flat square does not allow for a spin 3 state. We can construct states with arbitrarily high spin though we do not, since there is little experimental data known beyond spin 6.

The first excited state in the trivial rep $\phi^{(b)}$ is equally concentrated around the tetrahedral and square configurations. We identify this, when combined with the spin 0 rotational state, with the first excited state of the experimental spectrum, $0_e^+$, at 6.05 MeV. This vibrational wavefunction also gives rise to a spin 4 state with 16.44 MeV and a high energy spin 6 state. Further excited states of the trivial rep such as $\phi^{(c)}$ give rise to more $0^+, 4^+, 6^+, \ldots$ bands. These states all have positive parity but there are also vibrational wavefunctions in the trivial rep with negative parity such as $\phi^{(d)}$. It might be thought that one cannot combine the state $|0,0\rangle$ with a negative parity vibrational wavefunction since $|0,0\rangle$ has positive intrinsic parity. However, $\phi^{(d)}$ vanishes at all configurations with intrinsic parity: precisely those with a reflection symmetry. Hence the wavefunction

$$\phi^{(d)} |0,0\rangle \tag{4.43}$$

is allowed and has spin-parity $0^-$. This is the first time such a state has been accommodated in the Skyrme model. Although it appears fortuitous that $\phi^{(d)}$ vanishes at all configurations with a reflection symmetry, it is simply a consequence of the combination of negative parity with the trivial representation. There are similar states with spin-parity $4^-$ and $6^-$. Since the wavefunction $\phi^{(d)}$ is heavily constrained, it has very high energy. Similarly the vibrational wavefunction $\phi^{(h)}$, which lies in the sign rep and has positive parity, may be combined with the spin state $|3,2\rangle - |3,-2\rangle$ which has spin-parity $3^+$. A state with this spin-parity cannot be obtained in a rigid body analysis. More states, with spin-parity $6^+, 7^+, \ldots$ may also be constructed using $\phi^{(h)}$.

The lowest energy state with non-zero isospin is

$$\phi^{(e)} |0,0\rangle |1,0\rangle . \tag{4.44}$$

This isospin 1 wavefunction gives rise to a triplet of states for Oxygen-16, Fluorine-16 and Nitrogen-16 all with spin-parity $0^-$. There are then two spin 2, isospin 1 states which take the form

$$\phi^{(a)} \left( |2,2\rangle - i\sqrt{2}\,|2,0\rangle + |2,-2\rangle \right) \left( |1,1\rangle + |1,-1\rangle \right) \tag{4.45}$$

$$\text{and } \phi^{(e)} \left( |2,2\rangle - i\sqrt{2}\,|2,0\rangle + |2,-2\rangle \right) \left( |1,1\rangle - |1,-1\rangle \right) .$$

There are further states with higher isospin and higher spin, though these have a rather large energy.

79

Rovibrational states in the standard two-dimensional representation are most easily presented using a three-dimensional set of spin states $|\Theta\rangle_i$. These are chosen to transform into each other under the action of $S_3$. We demand they transform inversely compared to the objects of $S_3$ so that under the element (123) the spin states permute as

$$|\Theta\rangle_1 \to |\Theta\rangle_3 \to |\Theta_2\rangle \; .$$

For spin 2, $|\Theta\rangle_i$ are the states with zero projection on the $i^{\text{th}}$ axis. They satisfy

$$\hat{L}_i |\Theta\rangle_i = 0 \; \text{ and } \; |\Theta\rangle_1 + |\Theta\rangle_2 + |\Theta\rangle_3 = 0 \, . \tag{4.46}$$

These are the rotational states required to construct a consistent rovibrational state from standard irrep vibrational wavefunctions. The lowest energy rovibrational state of this kind is

$$
\begin{aligned}
|\Psi\rangle &= u^{(i)} |\Theta\rangle_1 + v^{(i)} |\Theta\rangle_2 + w^{(i)} |\Theta\rangle_3 \\
&= \frac{\sqrt{3}}{2\sqrt{2}} (u^{(i)} - v^{(i)}) \left( |2,2\rangle + |2,-2\rangle \right) - \frac{3}{2} (u^{(i)} + v^{(i)}) |2,0\rangle \, ,
\end{aligned}
\tag{4.47}
$$

where we have rewritten the expression in terms of the usual spin states which have definite $L_3$ eigenvalues, in the second line. Notice that the rovibrational state can be expressed in terms of a two-dimensional basis of spin states as would be expected for the standard irrep. The total wavefunction (4.47) is concentrated at the flat square configurations. At the flat square which lies in the $x$-$y$ plane ($\zeta = \frac{1}{2} + i\frac{1}{2}$), the vibrational wavefunctions $u^{(i)}$ and $v^{(i)}$ are equal. Hence at this point the first term in (4.47) vanishes and the total wavefunction is proportional to $|2,0\rangle$. This must occur since in rigid body quantisation, $|2,2\rangle + |2,-2\rangle$ is not allowed by the flat square while $|2,0\rangle$ is. The rovibrational state (4.47) is analogous to the known rigid body wavefunction of the flat square with spin 2. Although some spin 0 rovibrational states, such as the one which includes the vibrational wavefunction $\phi^{(b)}$, contain contributions from the flat square configuration, there are no spin 0 states which are dominated by the square. Hence, there is no state in our model analogous to a rigid body state of the square with spin 0. This highlights a key difference between rigid body quantisation and our scheme; here, the rotational band of the square only begins at spin 2.

The rotational states $|\Theta\rangle_i$ can also be paired with the vibrational wavefunctions $\{u^{(l)}, v^{(l)}, w^{(l)}\}$ which have negative parity and vanish at all the flat squares. Being

more constrained, the negative parity vibrational wavefunctions have higher energy than the positive parity ones. Hence there is an energetic splitting between the two lowest spin 2 states due to their different vibrational wavefunctions.

There are similar states for spin-parity $J^P = 4^\pm, 5^\pm, 6^\pm, \ldots$. The lowest energy spin 4 state is

$$|\Psi\rangle = \sqrt{\frac{7}{32}}(u^{(i)} + v^{(i)})\left(|4, 4\rangle + |4, -4\rangle\right) - \sqrt{\frac{1}{8}}(u^{(i)} - v^{(i)})\left(|4, 2\rangle + |4, -2\rangle\right)$$
$$- \sqrt{\frac{5}{16}}(u^{(i)} + v^{(i)})|4, 0\rangle . \tag{4.48}$$

At the flat square which lies in the $x$-$y$ plane the wavefunction becomes

$$|\Psi\rangle = \sqrt{\frac{7}{32}}(u^{(i)} + v^{(i)})\left(|4, 4\rangle - \sqrt{\frac{10}{7}}|4, 0\rangle + |4, -4\rangle\right) . \tag{4.49}$$

This is different than what one would obtain from a rigid body analysis where there would be two distinct states. In fact, the wavefunction (4.49) is not an eigenfunction of the rotational operator, $\nabla^2$ at the flat square. This is because the rotational term $E_{L_3,K_3}^{(1)}(\zeta)$ was neglected in the Schrödinger equation (4.21).

The higher energy vibrational wavefunctions of the standard irrep, such as $u^{(j)}$, can also be combined with spin states. In addition there are non-zero isospin states that fall into the standard irrep such as the spin 0, isospin 1 state

$$\left(u + e^{\frac{2\pi i}{3}}v + e^{\frac{4\pi i}{3}}w\right)|0, 0\rangle|1, 1\rangle + \left(e^{\frac{5\pi i}{3}}u - v + e^{\frac{\pi i}{3}}w\right)|0, 0\rangle|1, -1\rangle . \tag{4.50}$$

There are many more states with higher isospin and spin.

### 4.3.6  Energy spectrum from the $E$ vibration

To find the energy spectrum of our model the rotational energy term $E_J^{(1)}$ must be reintroduced. To do so, we calculate the correction

$$E_1 = -\frac{\hbar^2}{2}\int \langle\Psi|\nabla^2|\Psi\rangle \, d\zeta - \hbar^2\frac{J(J+1)}{2\Lambda_{\text{tet}}} , \tag{4.51}$$

for a given rovibrational wavefunction $|\Psi\rangle$. The energy $E_1$ is the correction to the rotational energy due to the fact that the Skyrme configurations on $\mathcal{M}_E$ do not all have an isotropic inertia tensor. To calculate (4.51) we need an ansatz for the

spatial moment of inertia tensor $\Lambda_J(\zeta)$. We approximate $\Lambda_J$ by taking each $B = 4$ Skyrmion to be an extended but localised particle. If their positions $\tilde{\boldsymbol{x}}$ are known, the moment of inertia tensor may be calculated using the parallel axis theorem. The mapping (4.12) from $\mathcal{F}$ to the Riemann sphere gives a coordinate $\hat{\boldsymbol{x}}(\zeta)$ on the sphere. We then divide by an appropriate factor to describe the asymptotic behaviour of $\mathcal{M}_E$, giving a coordinate $\tilde{\boldsymbol{x}}$ on $\mathcal{M}_E$. The $D_2$ symmetry of $\mathcal{M}_E$ implies that $\Lambda_J$ is diagonal giving three independent components. For this approximation, their values in the red region of Figure 4.4 are

$$
\begin{aligned}
\Lambda_{11}(\zeta) &= \left( 6586 \, \frac{\hat{y}(\zeta)^2 + \hat{z}(\zeta)^2}{1 - \hat{z}(\zeta)^2} + 2562 \right) \\
\Lambda_{22}(\zeta) &= \left( 6586 \, \frac{x'(\zeta)^2 + z'(\zeta)^2}{1 - z'(\zeta)^2} + 2562 \right) \\
\Lambda_{33}(\zeta) &= \left( 6586 \, \frac{x'(\zeta)^2 + y'(\zeta)^2}{1 - z'(\zeta)^2} + 2562 \right) = 9148 \, .
\end{aligned}
\tag{4.52}
$$

The third component is constant, consistent with the fact that the Skyrme configurations have approximately equal extent around the $z$-axis, along the scattering line seen in Figure 4.2. To find the moment of inertia tensor in the other regions, one should permute the denominators in (4.52). The ansatz is measured in Skyrme length units and matches the moments of inertia of the standard Skyrme model at the tetrahedral, square and asymptotic configurations.

The low lying rovibrational wavefunctions and their energies are displayed in Table 4.4. Here, we separate the energy contribution from the vibrational wavefunction, the zeroth order rotational energy and the rotational correction $E_1$. If we are confident that a state in our model describes an experimentally observed state we also include this identification in the table. The vibrational and rotational units are calibrated using the first excited $0^+$ and the lowest energy $4^+$ states respectively.

The data from Table 4.4 is displayed again in graph form in Figure 4.7. This helps identify the approximate rotational bands that are instructive in interpreting the results. Note that the gradient of the rotational bands are inversely proportional to the moment of inertia of the configuration where the wavefunction is concentrated. This means that the tetrahedral rotational band (which connects the lowest lying $0^+$, $3^-$, $4^+$ states) is steeper than the flat square band (which connects the lowest $2^+$ state and the first excited $4^+$ state).

| $J^P$ | $I$ | Wavefunction | $E_\text{vib}$ | $E_0$ | $E_1$ | $E$ | Exp. |
|---|---|---|---|---|---|---|---|
| $0^+$ | 0 | $(a)$ | 0 | 0 | 0 | 0 | 0 |
| $0^+$ | 0 | $(b)$ | 6.05 | 0 | 0 | 6.05 | 6.05 |
| $3^-$ | 0 | $(e)$ | 0.18 | 7.53 | -1.24 | 6.47 | 6.13 |
| $2^+$ | 0 | $(i)$ | 3.45 | 3.77 | -0.58 | 6.66 | 6.92 |
| $2^-$ | 0 | $(l)$ | 5.27 | 3.77 | -0.60 | 8.43 | 8.87 |
| $4^+$ | 0 | $(a)$ | 0 | 12.55 | -2.20 | 10.35 | 10.35 |
| $2^+$ | 0 | $(j)$ | 8.72 | 3.77 | -1.21 | 11.28 | 11.52 |
| $4^+$ | 0 | $(i)$ | 3.45 | 12.55 | -3.38 | 12.62 | 11.10 |
| $2^-$ | 0 | $(m)$ | 11.05 | 3.77 | -1.03 | 13.78 | 12.53 |
| $2^+$ | 0 | $(k)$ | 12.22 | 3.77 | -1.28 | 14.70 | – |
| $4^-$ | 0 | $(l)$ | 5.27 | 12.55 | -3.11 | 14.71 | 14.3 |
| $0^+$ | 0 | $(c)$ | 14.89 | 0 | 0 | 14.89 | – |
| $0^-$ | 1 | $(e)$ | 0.18 | 15.61 | 0 | 15.79 | 12.80 |
| $0^-$ | 0 | $(d)$ | 16.35 | 0 | 0 | 16.35 | 10.96 |
| $4^+$ | 0 | $(b)$ | 6.05 | 12.55 | -3.24 | 16.44 | – |
| $3^-$ | 0 | $(f)$ | 10.67 | 7.53 | -1.68 | 16.52 | – |
| $5^+$ | 0 | $(i)$ | 3.45 | 18.83 | -5.39 | 16.89 | – |
| $2^+$ | 1 | $(a)$ | 0 | 18.20 | -0.61 | 17.58 | – |
| $4^+$ | 0 | $(j)$ | 8.72 | 12.55 | -3.34 | 17.94 | – |
| $3^+$ | 0 | $(h)$ | 12.57 | 7.53 | -2.71 | 17.39 | 15.79 |
| $0^+$ | 1 | $(i)$ | 3.45 | 14.43 | 0 | 17.89 | – |
| $0^+$ | 0 | *Not displayed* | 18.78 | 0 | 0 | 18.78 | – |
| $5^-$ | 0 | $(l)$ | 5.27 | 18.83 | -4.91 | 19.19 | – |
| $2^-$ | 0 | $(n)$ | 16.92 | 3.77 | -1.22 | 19.47 | – |
| $2^+$ | 0 | *Not displayed* | 17.10 | 3.77 | -1.25 | 19.63 | – |
| $0^-$ | 1 | $(l)$ | 5.27 | 14.43 | 0 | 19.71 | – |
| $4^-$ | 0 | $(m)$ | 11.05 | 12.55 | -3.85 | 19.75 | – |
| $6^+$ | 0 | $(a)$ | 0 | 26.36 | -5.45 | 20.91 | 21.05 |
| $6^-$ | 0 | $(e)$ | 0.18 | 26.36 | -4.34 | 22.20 | – |
| $6^+$ | 0 | $(i)$ | 3.45 | 26.36 | -4.34 | 25.47 | – |
| $6^-$ | 0 | $(l)$ | 5.27 | 26.36 | -4.48 | 27.15 | – |

Table 4.4: The low energy states of our system. We list the spin-parity, isospin, the
vibrational wavefunction used in the construction of the rovbirational

Table 4.4: state (the labels refer to specific wavefunctions, displayed in Figure 4.6), vibrational energy $E_{\text{vib}}$, $0^{\text{th}}$ order rotational term $E_0$, rotational correction $E_1$ and total energy $E$ for each state. When an identification with an experimental state is clear, we also list this. The experimental data is taken from [64].
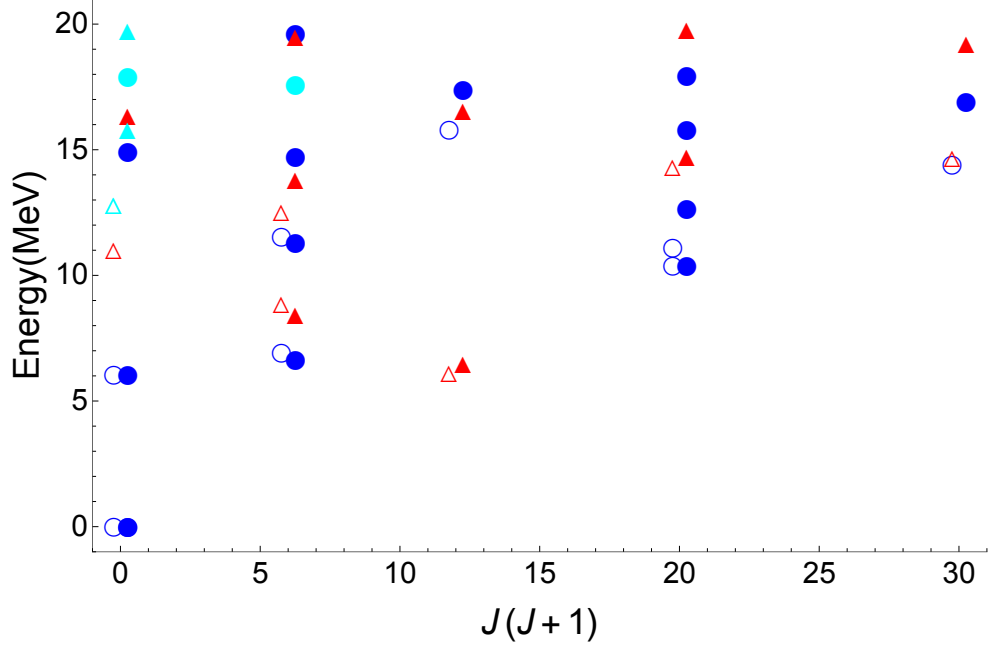


Figure 4.7: The energy spectrum of our model. Calculated states of positive parity (solid circles) and negative parity (solid triangles) are plotted. Isospin 0 states are coloured red and blue for positive parity and negative parity respectively while isospin 1 states are coloured cyan. Where the identification with an experimentally observed state [64] is clear, we also plot these (hollow symbols).

The lowest lying $0^+, 3^-, 4^+$ band is analogous to the tetrahedral band in rigid body quantisation. The $3^-$ state lies slightly above the band in our model since $\phi^{(e)}$ has more vibrational energy than $\phi^{(a)}$. The first excited state of the spectrum $0_e^+$ is identified with the $\phi^{(b)}$ wavefunction. This is equally concentrated around the tetrahedral and square configurations. Our interpretation of the $0_e^+$ state, as an admixture of configurations, is novel and stands in contrast with other descriptions

84

of the nucleus. The work of Epelbaum et al. claims that the state comes just from a flat square configuration [49]. However, this information is extracted indirectly from their wavefunction and we are unsure if their analysis would differentiate between our interpretation and theirs. Hence we do not consider our analysis to be in conflict with theirs.

The gap between the lowest energy $2^+/2^-$ states is 1.77 MeV, close to the experimental value of 1.96 MeV. The gap is mostly due to the different energies of the vibrational wavefunctions. In the analysis of [66] the spin 2 states are both local excitations around the tetrahedron, giving them the same energy. The energy gap between the states is attributed to a splitting of the rotational energy at a higher order. However, the gap is $\sim 2$ MeV which is rather large for a rotational perturbation. Instead, we believe that to describe the gap, one must include the square configuration in the quantisation procedure as we have done.

The first excited state with spin $4^+$, denoted $4_e^+$, was given in (4.48). It lies at 12.62 MeV, 1.52 MeV above the experimental state that it should describe. The $E_1$ contribution to the state is large, though this correction is meant to be perturbative. A more careful calculation may improve the result. A model where the flat square is wider would have a shallower rotational band between the $2^+$ and $4_e^+$ states, leading to a decrease in energy of the $4_e^+$ state. The lowest energy $4^-$ state is in good agreement with the first experimental $4^-$ state.

There are numerous states with large vibrational but low rotational energies. The choice of potential (4.34) is only suitable near the low energy configurations and not appropriate further away – where the excited states are partially concentrated. Because of this, the energies of the highly excited states should be treated with caution. A more realistic potential would flatten out asymptotically, reducing the energy of all the vibrational wavefunctions though having the biggest effect on the highly excited ones. With this in mind we have identified the $0^-$ state at 16.35 MeV with the experimentally observed state at 11.0 MeV and hope that a realistic potential would remedy the large discrepancy in energies. We have some confidence in our identification as there are few alternative descriptions. It is not an isospin 1 state, as can be seen by considering the spectra of $^{16}$F and $^{16}$N. In general, the shell model struggles to describe $0^-$ states while a local vibrational analysis gives rise to a state with very high energy [62].

There are many excited spin 2 states in our model. There are also many

85

experimentally observed spin 2 states, 27 with energies below 20 MeV. The large number of states makes it impossible to identify which states from our model describe which experimentally observed states without further information such as electromagnetic transition rates. In contrast, there are only three $3^+$ states which lie below 20 MeV. The lowest is likely due to the $F$ vibration which we shall study in the next section. The first excited $3^+$ state, at 15.79 MeV, is identified with the state arising from $\phi^{(g)}$ which lies at 17.39 MeV. The energy of the state would be lower if a more realistic potential was used. We previously noted that the $3^+$ state was unusual, impossible to find in a rigid body quantisation.

There are many allowed states with high spin. The lowest energy $5^+$ state comes from the standard representation wavefunctions $\{u^{(i)}, v^{(i)}, w^{(i)}\}$. As such, it is an approximate rotational excitation of the flat square. It has an energy of 16.89 MeV, to be compared with the experimental low lying $5^+$ state at 14.40 MeV. Although the energy is too large, we have not yet taken account of rotational deformations. When a Skyrme configuration acquires spin it naturally deforms. The effect is more pronounced for larger spins. We can estimate how much deformation is required to lower the energy of the spin 5 state so that it matches the experimental data by using the parallel axis theorem. The flat square is made from $B = 4$ Skyrmions at the points $(\pm d_0, \pm d_0, 0)$. To reduce the rotational energy of the spin 5 state by 2.5 MeV, the deformed square would have to lie at approximately $1.2(\pm d_0, \pm d_0, 0)$. To see if this is reasonable one can study the deformation numerically, as has been done for isospin deformations [29]. The same effect would lower the energy of the spin $4^+$ state at 12.62 MeV which is also too large in our model. Already, it is clear that rotational deformation is important for states with spin 5 and so we do not have much confidence in our analysis for states with even higher spin. We do find two $6^-$ states at 22.20 MeV and 27.15 MeV. No $6^-$ states have been observed experimentally.

There are also states with non-zero isospin such as (4.50). To calculate their energy we must estimate the isorotational moment of inertia tensor $\Lambda_I$. The contribution from each $B = 4$ cube is approximately additive, regardless of their position. Hence we take $\Lambda_I$ to be constant everywhere and equal to its value at the tetrahedron in the Skyrme model. This approximation gives rise to an isospin 1, spin 0 state at 15.79 MeV which overestimates the energy of the first experimental state with isospin 1, which lies at 12.80 MeV. A modification to the Skyrme

model such as the inclusion of the $6^{\text{th}}$ order term [15] may change the value of $\Lambda_I$. In addition, no one has studied the effect of vibrational quantisation on the iso-moments of inertia. The other isospin states have higher energy and are hard to identify with experimental states.

In conclusion, our model of the $E$ vibration provides a good description of many of the low lying states of $^{16}$O. We struggle with highly vibrationally excited states since our potential is not appropriate for them. In addition, it appears that we must include rotational deformations in the description of states with large spin. Hence to describe the spectrum at higher energies we must make some improvements to the model presented in this chapter.

## 4.4 The other vibrational modes

### 4.4.1 The $A$ vibration

The $A$ vibration is one-dimensional and physically represents the symmetric stretching of the tetrahedron. It is often referred to as the breather mode. The vibrational manifold $\mathcal{M}_A$ is the half-line with parameter $r$ measuring the distance of the $\alpha$-particles from the origin. Let $r = r_t$ be the configuration at the energy minimising tetrahedron. The Finkelstein-Rubinstein constraints at $r = r_t$ must apply everywhere on the manifold since every configuration on $\mathcal{M}_A$ has tetrahedral symmetry. Hence the wavefunctions are of the form

$$|\Psi_A\rangle = \chi_A(r)\,|\psi\rangle\;, \tag{4.53}$$

where $\chi_A(r)$ is the vibrational wavefunction on $\mathcal{M}_A$ and $|\psi\rangle$ is any rotational state allowed by the tetrahedron as listed in Table 4.1. There are no cross terms in the metric as the manifold is one-dimensional. The wavefunction $\chi_A(r)$ satisfies the Schrödinger equation

$$-\frac{\hbar^2}{2}\chi_A''(r) + V(r)\chi_A(r) = E\chi(r)\,. \tag{4.54}$$

The simplest way to model the potential is to treat it as a harmonic well around $r_t$ with frequency $\omega_A$. We may find the frequency directly from the Skyrme model or set it empirically. We do the latter since the Skyrme model can be modified in

many ways and assume that the first excited state of (4.54) is responsible for the lowest energy $0^+$ state not yet described by our model which lies at 12.0 MeV. To see if this is reasonable, we can consider the energy of the Carbon-12 breathing mode. This nucleus is described in the Skyrme model as three $\alpha$-particles arranged in a triangle [30]. The breathing mode corresponds to the three particles moving in and out while keeping triangular symmetry. By treating each nucleus as a set of point particles on springs, we can estimate the energy of this mode for $^{12}$C. The frequency of its breathing mode in this approximation is given by $\sqrt{3}/2\,\omega_A$ which gives rise to a state with energy 10.4 MeV. This matches the second experimentally observed excited state of $^{12}$C with spin 0, which lies at 10.3 MeV. This gives us confidence in the identification of the 12.0 MeV state as a breathing mode of the tetrahedron.

The rotational energy for a wavefunction with spin $J$ is

$$\langle \Psi_A | \hat{\mathcal{H}} | \Psi_A \rangle = \int \frac{\hbar^2 \chi_A(r)^2}{2\Lambda(r)} J(J+1) dr \, , \qquad (4.55)$$

where $\Lambda(r)$ is the moment of inertia. The expression is simple due to the tetrahedral symmetry of the configurations on $\mathcal{M}_A$. Each vibrational wavefunction $\chi_A(r)$ gives rise to an approximate rotational band with spins $0^+, 3^-, 4^+, \ldots$. The ground state is focused around $r = r_t$, giving a rotational band with slope approximately equal to the slope of the lowest lying band. The excited wavefunctions are concentrated away from $r = r_t$ and so the configurations have larger moments of inertia. These give rise to rotational bands with slightly shallower slopes. We do not calculate the slopes in detail. There are sufficiently many states in the experimental spectrum to accommodate the excited states of the breathing mode. However, the large number of excited states makes it difficult to decipher which experimental state corresponds to which model state.

## 4.4.2 The $F$ vibration

The $F$ vibration generates a three-dimensional manifold of configurations. These include the modes where one $\alpha$-cluster separates from the other three, preserving $C_3$ symmetry. The manifold $\mathcal{M}_F$ has $A_4$ symmetry, the alternating group of four objects. Here the objects are the individual $\alpha$-particles. The manifold is significantly more difficult to deal with beyond a harmonic approximation, as was

done with the $E$ vibration. The main difficulty is that the kinetic operator does not separate as it does in (4.21). The effect of this is hard to measure. We shall assume that the cross terms are small and that the potential is harmonic with frequency $\omega_F$ as is done in [66]. Other work such as [51] suggests that the cross terms have a large effect on the energies of the states.

With these approximations the excited wavefunctions on $\mathcal{M}_F$ are harmonic oscillator wavefunctions. There is a basis for the first excited states $\{\psi^{(i)}\}$ with $i = 1, 2, 3$, where the wavefunctions transform in the same way as the spatial axes. Given this basis, a $\pi/2$ rotation on the Skyrme configuration is equivalent to the transformation

$$\left(\psi^{(1)}, \psi^{(2)}, \psi^{(3)}\right) \rightarrow \left(\psi^{(2)}, -\psi^{(1)}, \psi^{(3)}\right). \tag{4.56}$$

The rovibrational wavefunctions can be found using relations such as these. The lowest energy state has spin $1^-$ and takes the form

$$\left(\psi^{(1)} + i\psi^{(2)}\right)|1, 1\rangle - i\sqrt{2}\psi^{(3)}|1, 0\rangle + \left(\psi^{(1)} - i\psi^{(2)}\right)|1, -1\rangle. \tag{4.57}$$

Note the connection between the structure of the vibrational wavefunctions and the spin 1 spherical harmonics. There are further states of this kind with spin $2^+, 3^\pm, 4^\pm, \ldots$ .

The vibrational energy is estimated using a harmonic approximation while the moments of inertia are set empirically based on the energy spectrum. These are crude approximations, owing to our poor understanding of the manifold $\mathcal{M}_F$. There is an approximate rotational band in the energy spectrum which contains states with the spins matching those above. It includes an almost degenerate spin 3 pair which matches the degenerate $3^+$ and $3^-$ states in our simple model. Dealing with $\mathcal{M}_F$ more thoroughly will break the degeneracy. For example, one may reach the dual tetrahedron by taking one $\alpha$-particle through the other three, always preserving $C_3$ symmetry. This will favour positive parity states compared to negative parity ones, which also happened in the $E$ vibration.

### 4.4.3 Combining vibrations

Although the analysis so far has focused on each vibrational manifold separately, the vibrational wavefunctions actually lie on the total space. The ground state

wavefunction is

$$|\Psi\rangle = \phi^{(a)} \chi_A \psi_0 |0,0\rangle |0,0\rangle \; , \tag{4.58}$$

where the vibrational wavefunctions lie in the $E$, $A$ and $F$ manifolds respectively. The expression (4.58) is only true if the metric has no cross terms between the submanifolds. The individual wavefunctions may be excited in multiple manifolds at once. To construct such wavefunctions we assume that the metric on our total space is separable and further, that there are no cross terms between each vibrational manifold. One can find which spins are allowed by looking at the irreducible decompositions of the product spaces. For example, combining the $E$ and $F$ vibrations means looking at vibrational wavefunctions which fall into the $E \times F$ representation. The product space has the irreducible decomposition

$$E \times F = F + F \; . \tag{4.59}$$

Hence, wavefunctions which are excited in both the $E$ and $F$ vibrations have the same spins as wavefunctions excited in just the $F$ vibration, but here there are twice as many of them. In fact, there is parity doubling. The lowest energy combined state has spin $1^{\pm}$ and takes the form

$$\left( u\psi^{(1)} + iv\psi^{(2)} \right) \left( |1,1\rangle + |1,-1\rangle \right) + i\sqrt{2}w\psi^{(3)} |1,0\rangle \; , \tag{4.60}$$

where $\{u, v, w\}$ are the vibrational wavefunctions in the standard irrep on $\mathcal{M}_E$ and $\psi^{(i)}$ are the vibrational wavefunctions on $\mathcal{M}_F$ described in the previous section. The wavefunction (4.60) is a particularly simple combined state since the wavefunctions on $\mathcal{M}_E$, the wavefunctions on $\mathcal{M}_F$ and the spin states all transform in a similar way. The vibrational energy of the state is simply the sum of the vibrational energies of the composite wavefunctions. The rotational energy is taken to be equal to the rotational energy of the $F$ vibration states. We list the allowed states up to 18 MeV in Table 4.5. All states have zero isospin. Note that our approximations, especially regarding the structure of the metric, are crude. The combined rovibrational wavefunctions are best thought of as a good starting point for further work.

| $J^P$ | Rep. | E wvfn | $E_{\mathrm{vib}}$ | $E_{\mathrm{rot}}$ | $E$ | Exp. |
|---|---|---|---|---|---|---|
| $1^-$ | F | $(a)$ | 6.07 | 0.86 | 7.12 | 7.12 |
| $2^+$ | F | $(e)$ | 6.26 | 2.58 | 8.84 | 9.84 |
| $1^-$ | E × F | $(i)$ | 9.52 | 0.86 | 10.39 | 9.59 |
| $3^-$ | F | $(a)$ | 6.07 | 5.16 | 11.26 | 11.60 |
| $3^+$ | F | $(e)$ | 6.26 | 5.16 | 11.42 | 11.08 |
| $0^+$ | A | $(a)$ | 12.05 | 0 | 12.05 | 12.05 |
| $2^-$ | E × F | $(i)$ | 9.53 | 2.58 | 12.11 | – |
| $0^+$ | F × F | $(a)$ | 12.14 | 0 | 12.14 | – |
| $1^+$ | E × F | $(j)$ | 11.68 | 0.86 | 12.54 | 13.66 |
| $1^-$ | F | $(b)$ | 12.13 | 0.86 | 12.81 | 12.44 |
| $1^-$ | F × F | $(e)$ | 12.32 | 0.86 | 13.18 | 13.01 |
| $2^+$ | E × F | $(j)$ | 11.68 | 2.58 | 14.26 | – |
| $4^-$ | F | $(a)$ | 6.07 | 8.60 | 14.67 | – |
| $3^+/3^-$ | E × F | $(i)$ | 9.53 | 5.16 | 14.69 | – |
| $2^+$ | F × F | $(a)$ | 12.14 | 2.58 | 14.72 | – |
| $4^+$ | F | $(b)$ | 6.26 | 8.60 | 14.86 | – |
| $2^-$ | F × F | $(b)$ | 12.32 | 2.58 | 14.90 | – |
| $1^+$ | E × F | $(l)$ | 14.79 | 0.86 | 15.65 | – |
| $3^+/3^-$ | E × F | $(j)$ | 11.68 | 5.16 | 16.84 | – |
| $3^-$ | F × F | $(e)$ | 12.32 | 5.16 | 17.3 | – |
| $2^+$ | E × F | $(e)$ | 14.80 | 2.58 | 17.38 | – |
| $3^+$ | F × F | $(a)$ | 12.14 | 5.16 | 17.48 | – |

Table 4.5: The allowed spin states which arise from the $F$ and $A$ vibrations and their estimated energies. We display the spin-parity, representation that the total wavefunction falls into, vibrational wavefunction from the $E$ vibration which is used to make the state (the labels refer to the specific wavefunctions shown in Figure 4.6), vibrational energy $E_{\mathrm{vib}}$, $0^{\mathrm{th}}$ order rotational term $E_0$, rotational correction $E_1$ and total energy $E$ for each state. When an identification with an experimental state is clear, we also list this.

## 4.5 The full energy spectrum

The full energy spectrum of our model up to spin 4, alongside all experimentally known states up to 18 MeV are displayed in Figure 4.8. Further details of these states can be found in Tables 4.4 and 4.5.
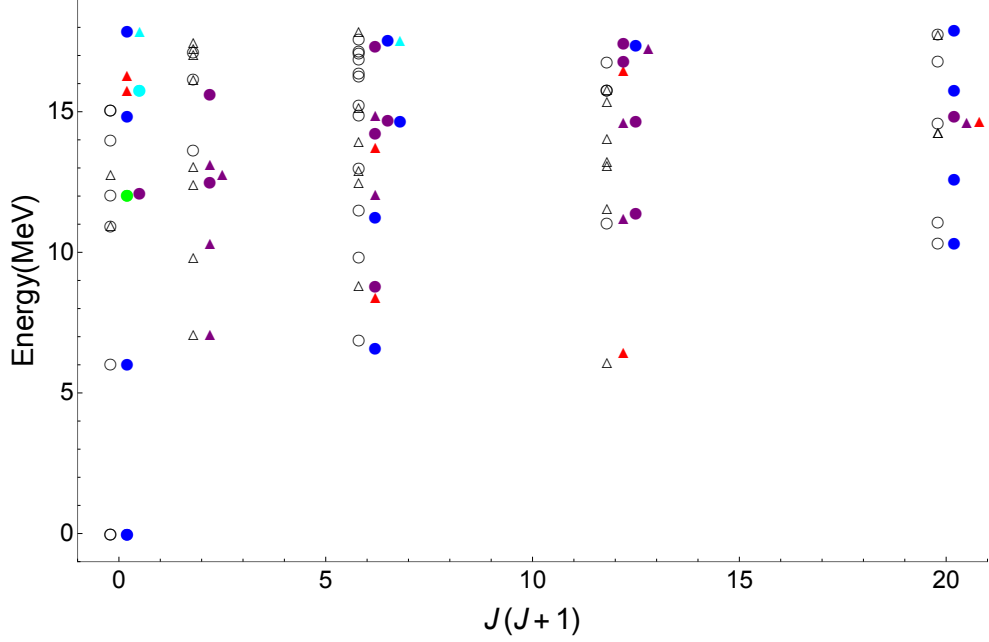


Figure 4.8: The energy spectrum of the full model. Calculated states of positive parity (solid circles) and negative parity (solid triangles) are plotted. Blue and red states arise from our detailed calculation in the $E$ vibration while purple and green states arise from the $F$ and $A$ vibrations respectively. Combined state are also coloured purple and isospin 1 states are coloured cyan. Where our model states overlap, we have shifted some data points to the right. In reality, all points should lie on the integer valued $J(J+1)$. The entire experimental spectrum up to 18 MeV is represented by hollow black symbols, circles have positive parity while triangles have negative parity.

We discussed the energy spectrum arising from the $E$ vibration in some detail. Here, we speak more broadly. The model contains more low energy spin 2 states than any other spin, in agreement with the experimental data. It also contains several other features seen experimentally: a large gap between the lowest energy

spin 3 states and the fact that there are few spin $1^+$ states. The most obvious contradiction between data and the model is that we predict two low energy spin $4^-$ states while there is only one seen experimentally. It is experimentally challenging to separate overlapping states with equal spin and parity, so this may not be a contradiction. Overall, the results are promising with no serious contradictions with experimental data. The analysis of this chapter shows that the vibrational model gives a good description of $^{16}$O and serves as an excellent foundation for further work on the nucleus.

## 4.6 Electromagnetic transition rates

Electromagnetic transitions measure the rate of $\gamma$-ray emissions between states. Their strength depends on the structure of the nucleus and the nature of its excited states. A large transition rate indicates collective motion of the nucleus, making it a good test of models with collective features, such as ours. In the long wavelength (or low energy of radiation) limit, the reduced transition probability for electric multipole radiation can be calculated from the expression

$$B(El, J_i \rightarrow J_f) = \frac{2J_f + 1}{2J_i + 1} \left| \int d^3r \, \langle \Psi_f | \, | \rho(\zeta, \boldsymbol{r}, \boldsymbol{\alpha}) r^l Y_l(\Omega) | \, | \Psi_i \rangle \right|^2, \qquad (4.61)$$

where $\boldsymbol{r}$ and $\Omega$ are space fixed coordinates, $\langle | \, |$ means we take the reduced matrix elements and $\rho$ is the charge density of the Skyrme configuration on $\mathcal{M}$. The coordinates $\boldsymbol{\alpha}$ are the Euler angles, which live on the fibre of the vibrational manifold. The configurations defined in Section 4.3 all have $\boldsymbol{\alpha} = \boldsymbol{0}$. Note that the spin states are functions of the Euler angles. The reduced matrix elements take account of the fact that we must average over all space-fixed angular momenta projections.

To calculate (4.61) we simplify the formula using the relation

$$\frac{2J' + 1}{2J + 1} \left| \int d^3r \, \langle J_f L_3 | \, | \rho(\zeta, \boldsymbol{r}, \boldsymbol{\alpha}) Y^l(\Omega) | \, | J_i L_3' \rangle \right|^2 = \left| \sum_{m'} \langle J' L_3' l m' | J L_3 \rangle \, \tilde{Q}_{lm'}(\zeta) \right|^2.$$
$$(4.62)$$

where $\langle J' L_3' l m' | J L_3 \rangle$ is a Clebsch-Gordon coefficient and

$$\tilde{Q}_{lm}(\zeta) = \int \rho(\zeta, \boldsymbol{r}, \boldsymbol{0}) r^l Y_{lm}(\Omega) \, d^3r \,. \qquad (4.63)$$

We prove this formula in Appendix B. The transition rates can then be expressed solely in terms of the modified multipole functions $\tilde{Q}_{lm}(\zeta)$ and the vibrational wavefunctions. To demonstrate how the formalism works we now calculate two transition rates, focusing on wavefunctions in the $E$ vibration since we understand these the best.

### E4: Trivial to trivial

The simplest transitions are those between states in the trivial representation. Consider the transition between the states

$$|\Psi_i\rangle = \phi^{(a)}(\zeta)\sqrt{\frac{5}{24}}\left(|4,4\rangle + \sqrt{\frac{14}{5}}\,|4,0\rangle + |4,-4\rangle\right) \tag{4.64}$$

$$\text{and}\quad |\Psi_f\rangle = \phi^{(a)}(\zeta)\,|0,0\rangle\ ,$$

where $\phi^{(a)}$ is normalised so that $\langle\Psi|\Psi\rangle = 1$. The index $(a)$ refers to the specific vibrational wavefunction displayed in Figure 4.6. In this case the matrix element (4.61) is

$$B(\text{E4},4^+ \to 0^+) = \frac{5}{24}\left|\int d\zeta\,\phi^{(a)}(\zeta)^2 \sum_{m'}\left(\langle 444m'|00\rangle + \sqrt{\frac{14}{5}}\,\langle 404m'|00\rangle\right.\right.$$

$$\left.\left. + \langle 4-44m'|00\rangle\right)\tilde{Q}_{4m'}\right|^2$$

$$= \frac{5}{24\times 9}\left|\int d\zeta\,\phi^{(a)}(\zeta)^2\left(\tilde{Q}_{44} + \sqrt{\frac{14}{5}}\tilde{Q}_{40} + \tilde{Q}_{4-4}\right)\right|^2 , \tag{4.65}$$

a rather simple expression. Note that in the rigid body limit, the transition rate becomes

$$B(E4,4^+ \to 0^+) = \frac{5}{24\times 9}\left(\tilde{Q}_{44} + \sqrt{\frac{14}{5}}\tilde{Q}_{40} + \tilde{Q}_{4-4}\right). \tag{4.66}$$

### E2: Doublet to trivial

The transition between the $2^+$ state at 6.66 MeV and the ground state is more complicated, since the spin 2 state falls into the standard representation. The

relevant states for this transition are

$$|\Psi_i\rangle = \frac{1}{\sqrt{3}}\left(u^{(i)}|2,0\rangle_x + v^{(i)}|2,0\rangle_y + w^{(i)}|2,0\rangle\right)$$

$$= \frac{1}{2\sqrt{2}}(u^{(i)} - v^{(i)})\left(|2,2\rangle + |2,-2\rangle\right) - \frac{\sqrt{3}}{2}(u^{(i)} + v^{(i)})|2,0\rangle$$

and $\quad |\Psi_f\rangle = \phi^{(a)}(\zeta)|0,0\rangle$,

where the vibrational wavefunctions are normalised so that $\langle\Psi|\Psi\rangle = 1$. The transition is

$$B(\text{E2}, 2^+ \to 0^+) = \left| \int d\zeta \frac{u^{(i)} - v^{(i)}}{2\sqrt{2}}\phi^{(a)} \sum_{m'}\left(\langle 222m'|00\rangle \tilde{Q}_{2m'} + \langle 2-22m'|00\rangle \tilde{Q}_{2m'}\right) \right.$$

$$\left. - \frac{\sqrt{3}}{2}(u^{(i)} + v^{(i)})\phi^{(a)} \sum_{m'}\langle 202m'|00\rangle \tilde{Q}_{2m'} \right|^2$$

$$= \left| \int d\zeta \left(\frac{1}{2\sqrt{10}}(u^{(i)} - v^{(i)})\left(\tilde{Q}_{22} + \tilde{Q}_{2-2}\right) \right.\right.$$

$$\left.\left. - \frac{\sqrt{3}}{2\sqrt{5}}(u^{(i)} + v^{(i)})\tilde{Q}_{20}\right)\phi^{(a)} \right|^2.$$

Note that this formula also holds for the $0_e^+$ state, if $\phi^{(a)}$ is replaced with $\phi^{(b)}$.

A similar calculation gives the transition between the first $4^+$ and $2^+$ states. We suppress the index of the vibrational wavefunctions in this calculation. Now

$$|\Psi_i\rangle = \phi(\zeta)\sqrt{\frac{5}{24}}\left(|4,4\rangle + \sqrt{\frac{14}{5}}|4,0\rangle + |4,-4\rangle\right)$$

$$|\Psi_f\rangle = \frac{1}{2\sqrt{2}}(u - v)\left(|2,2\rangle + |2,-2\rangle\right) - \frac{\sqrt{3}}{2}(u + v)|2,0\rangle,$$

and the transition is

$$B(\text{E2}, 4^+ \rightarrow 2^+)$$

$$= \frac{5}{24} \left| \int \phi \left( -\frac{\sqrt{3}}{2}(u+v) \sum_{m'} \left( \langle 442m'|20 \rangle + \sqrt{\frac{14}{5}} \langle 402m'|20 \rangle + \langle 4-42m'|20 \rangle \right) \tilde{Q}_{2m'} \right. \right.$$

$$+ \frac{1}{2\sqrt{2}}(u-v) \sum_{m'} \left( \langle 442m'|22 \rangle + \langle 442m'|2-2 \rangle + \langle 4-42m'|22 \rangle + \langle 4-42m'|2-2 \rangle \right.$$

$$\left. \left. + \sqrt{\frac{14}{5}} \left( \langle 402m'|22 \rangle + \langle 402m'|2-2 \rangle \right) \right) \tilde{Q}_{2m'} \right) d\zeta \right|^2$$

$$= \frac{5}{24} \left| \int \phi \left( -\frac{\sqrt{3}}{\sqrt{5}}(u+v)\tilde{Q}_{20} + \frac{1}{\sqrt{10}}(u-v)\left( \tilde{Q}_{22} + \tilde{Q}_{2-2} \right) \right) d\zeta \right|^2$$

$$= \frac{5}{6} B(E2, 2^+ \rightarrow 0^+) \,,$$

which gives a relationship between the transitions. Several more transition rates are expressed in this form in Appendix B.

### 4.6.1 Estimating $\tilde{Q}$

The expressions in the previous section depend on the tensor components $\tilde{Q}_{lm}$ which in turn depends on the charge density $\rho$. To do actual calculations, an approximate expression for the baryon density is needed since

$$\rho(\boldsymbol{x}, \zeta) = \frac{1}{2} \mathcal{B}_0(\boldsymbol{x}, \zeta) \,,$$

for zero isospin. We estimate the baryon density $\mathcal{B}_0(\boldsymbol{x}, \zeta)$ by treating each $B = 4$ cube as a point particle. For a single cube, the baryon density takes the form

$$\mathcal{B}_0(\zeta, \boldsymbol{x}) = 4\, \delta^{(3)} \left( \tilde{\boldsymbol{x}}\,(\zeta) - \boldsymbol{x} \right) \,, \tag{4.67}$$

where $\tilde{\boldsymbol{x}}$ is the coordinate on $\mathcal{M}_E$ defined implicitly in (4.52). With this approximation, the modified multipole tensor takes the form

$$\tilde{Q}_{lm}(\zeta) = \kappa^l 8\, \tilde{r}^l Y_{lm}\left( \tilde{x}(\zeta), \tilde{y}(\zeta), \tilde{z}(\zeta) \right) \,. \tag{4.68}$$

We have introduced a length scale $\kappa$ which converts $\tilde{\boldsymbol{x}}$ to Skyrme units. This is fixed by calculating the quadrupole at the flat square

$$\tilde{Q}_{20}\left(\zeta = \frac{1}{2} + i\frac{1}{2}\right) = \kappa^2 \frac{1}{2} \sum_i 4\sqrt{\frac{5}{16\pi}} \left(2\tilde{z}(\zeta_i)^2 - \tilde{x}(\zeta_i)^2 - \tilde{y}(\zeta_i)^2\right)$$

$$= -\sqrt{\frac{80}{\pi}}\kappa^2 \,,$$

where $i$ labels the positions of the $B = 4$ cubes which form the square. In the Skyrme model, this quadrupole is equal to $-42.5$, giving $\kappa^2 \approx 2.66$. To test our ansatz, the following multipole at the tetrahedron is calculated

$$\tilde{Q}_{44} + \sqrt{\frac{14}{5}}\tilde{Q}_{40} + \tilde{Q}_{4-4} = 3\kappa^4 \sqrt{\frac{7}{10\pi}} \sum_{i=\text{tet}} \frac{1}{2}\mathcal{B}_0(\zeta_i, \boldsymbol{x}) \approx -120 \,. \tag{4.69}$$

This is to be compared to the result in the Skyrme model: $-114.2$. The approximation (4.67) is somewhat crude and the quantity (4.69) scales as the fourth power of length. Despite this, the value $-120$ is close to the true answer, giving us confidence in the approximation. Overall, the ansatz for the modified multipole tensors is

$$\tilde{Q}_{lm}(\zeta) = \left(\frac{42.5}{16}\right)^l 8\tilde{r}^l Y_{lm}\left(\tilde{x}(\zeta), \tilde{y}(\zeta), \tilde{z}(\zeta)\right) \,. \tag{4.70}$$

We can evaluate this expression analytically at any point on $\mathcal{M}_E$.

## 4.6.2 Results

The calculated transition rates are displayed in Table 4.6, alongside the experimental data where known. We convert from Skyrme length units to physical units by fixing the E4 transition to its experimental value.

The strength of the transition rates partially depend on how much the incoming and outgoing vibrational wavefunctions overlap. Hence the transition between the $4^+$ and $0^+$ states is large. However, they also depend on the structure of the operator and of the rotational part of the wavefunction. For example, the E1 transition between the lowest lying $4^+$ and $3^-$ states is zero. While their vibrational wavefunctions do overlap significantly, the structure of the rotational states forbid the transition. In detail, a term (4.62) is only non-zero if $L_3$ and $L_3'$ are at most $l$ apart. In the case mentioned above $l = 1$, but the $L_3$ and $L_3'$ values are all at least

| E$l$ | Transition | Our model $(e^2\mathrm{fm}^2)^l$ | Experiment $(e^2\mathrm{fm}^2)^l$ |
|---|---|---|---|
| E3 | $3^- \to 0^+$ | 230 | 205 |
| E4 | $4^+ \to 0^+$ | 378 | 378 |
| E6 | $6^+ \to 0^+$ | 8914 | – |
| E2 | $2^+ \to 0^+$ | 16.4 | 7.4 |
| E2 | $2^+ \to 0_e^+$ | 23.3 | 65 |
| E2 | $4^+ \to 2^+$ | 13.6 | 156 |
| E2 | $4_e^+ \to 2^+$ | 7.7 | 2.4 |
| E4 | $4^+ \to 0_e^+$ | 9.6 | – |
| E4 | $4_e^+ \to 0^+$ | 609 | – |
| E4 | $4_e^+ \to 0_e^+$ | 1614 | – |
| E1 | $4^+ \to 3^-$ | 0 | $< 1.2 \times 10^{-5}$ |
| E1 | $4_e^+ \to 3^-$ | 0 | $< 2.4 \times 10^{-5}$ |
| E1 | $2^+ \to 3^-$ | 0 | $< 1.6 \times 10^{-5}$ |

Table 4.6: A comparison of the transition rates of our model and experimental data. States with no subscript refer to the ground state of that spin. State with the subscript $J_e$ are the first excited state for the given spin. All experimental data is taken from [64].

two units apart. Due to results such as this, one cannot rely heavily on intuition to estimate the transition rates and instead needs a thorough understanding of the rovibrational wavefunctions' structure.

The transition rates along the lowest-lying band are in good agreement with the experimental data. The E6 transition is close to the result obtained in [66] which is expected since these states have similar descriptions in both models. These results support the idea that a tetrahedral arrangement of $\alpha$-particles does indeed produce the lowest rotational band in the $^{16}$O spectrum.

The transition $B(\mathrm{E2}; 2^+ \to 0_e^+)$ is larger than the transition $B(\mathrm{E2}; 2^+ \to 0^+)$ since the $0_e^+$ vibrational wavefunction overlaps more with the spin $2^+$ wavefunction, both being large at the flat square configurations. In the experimental data, the transitions obey this ordering, though the actual values are far from the experimental results. We cannot describe the large experimental transition $B(\mathrm{E2}; 4^+ \to 2^+)$, though we do get a reasonable result for $B(\mathrm{E2}; 4_e^+ \to 2^+)$. Naively one might

assume the second transition rate is very large as both states share the same vibrational wavefunction. However, a careful study of the structure of the states explains why it is small. These mixed results suggest something could be wrong with the identification of our states, possibly of the spin 4 states. As such, it seems important to gain more information about these. Hence we have calculated several E4 transitions involving the spin 4 states. These have not been measured experimentally as E4 transitions are highly suppressed compared to E2 transitions.

All the E1 transitions which have been calculated are zero. $B(\mathrm{E1}; 4^+ \rightarrow 3^-)$ is zero because of the structure of the rotational states and the other E1 transitions are zero because the total matrix element is odd around $\eta = \frac{1}{2}$. Their experimental counterparts are also small and so do not contradict our results.

We have only described transitions between wavefunctions which lie in the $E$ vibration of the tetrahedron. To include the other vibrations we must estimate the baryon density in the other manifolds and find concrete expressions for the wavefunctions on the total space. Once this is done, the formalism is essentially the same. We have focused on E transitions but M transitions are also seen experimentally. The M transitions depend on a current $\boldsymbol{j}$ which satisfies

$$\frac{\partial \rho}{\partial t} + \boldsymbol{\nabla} \cdot \boldsymbol{j} = 0 \, . \tag{4.71}$$

The obvious candidate for zero isospin is $\boldsymbol{j} = \boldsymbol{B}$, the spatial component of the topological current. Though its value can be calculated at static configurations such as the tetrahedron and flat square, how it varies over $\mathcal{M}$ is unclear. If one can calculate $\boldsymbol{B}(\zeta)$, the formalism for M transitions is similar to the formalism laid out in this section. Finally, we have not calculated the E0 transition between the first excited $0^+$ state and the ground state. Physically, the transition occurs due to the emission of two photons and hence the formalism is more complicated than for the examples in this section, where only one photon was emitted.

## 4.7 Conclusions and further work

In conclusion, we have studied a model of Oxygen-16 which describes the nucleus as four $\alpha$-particles which are centered around a tetrahedral configuration. The main novelty in the work is our Skyrme-inspired description of the $E$ vibrational manifold as the 6-punctured sphere. This goes beyond a local analysis near the

tetrahedron and includes the flat square configuration in the quantisation procedure. Its inclusion explains the large gap between the lowest energy spin 2 states which has never been explained in other cluster model calculations. The other cluster models also have a tendency to have too many states. The algebraic cluster model of [66] describes the $0^+$ state at 6.05 MeV as a breathing mode but there is then another $0^+$ state at roughly 7 MeV, arising from a doubly excited $E$ vibrational wavefunction. This is not seen in the spectrum. The model also contains three spin 3 states at around 10 MeV while there are actually only two. Our model does not have the same problem and so appears to most accurately describe the $^{16}$O energy spectrum with much of its success owing to the inclusion of the square configuration. A comparison to other models is harder to make. The lattice ab initio model has garnered the most attention in the literature, though it has only obtained states up to 7 MeV so far. Our model is attractive in comparison as we can extrapolate to large energies.

We studied states with large amounts of vibrational energy, high spin and composite states which lie in multiple vibrational manifolds. These three calculations were limited by our non-physical potential, the lack of rotational deformation and our poor understanding of cross-terms in the metric respectively. However, the way to deal with each of these contributions is known and we hope these issues can be overcome in future work. In addition we have found the first ever spin-parity $0^-$, isospin 0 state in the Skyrme model. Finally, we developed a method to calculate the electromagnetic transition rates for rovibrational wavefunctions and these transitions were calculated in our model, with mixed results.

The Skyrme model supports a stable chain-like configuration of $\alpha$-particles as seen in Figure 4.1. This is far away from the tetrahedron and flat square in configuration space and so the rigid body approximation can be used to study the chain's quantum states. This gives rise to a rotational band with spins $0^+, 2^+, 4^+, 6^+, \ldots$ . The chain has a very large moment of inertia and hence can produce states with high spin and low energy. There is a low-lying spin 6 state at 14.8 MeV which we fail to explain within our model. It has been suggested that the state comes from the chain configuration. If this were true, there would be a $0^+, 2^+, 4^+$ band leading up to the state in the experimental data. There is not, which casts doubt upon the idea. However, rotational deformations may be important for the calculation, given the large extent of the chain.

The potential (4.34) diverges asymptotically and is only appropriate near the low energy configurations. We chose it to make the Schrödinger equation easy to solve. Physically, the potential should flatten out asymptotically. One can keep the Schrödinger equation (4.21) separable and model the correct asymptotic behaviour by using a step potential such as

$$
V(\epsilon, \eta) = \begin{cases} 0 & \epsilon < \epsilon_0 \\ V_0 & \epsilon \geq \epsilon_0 \,, \end{cases} \tag{4.72}
$$

valid in the red region of $\mathcal{F}$. The Schrödinger equation with this potential can be solved in a similar way to the Schrödinger equation discussed in Section 4.3.4. We display the low lying spectrum for the parameters $\epsilon_0 = 1.5$ and $V_0 = 100$ in Figure 4.9. Compared to the spectrum of the system with potential (4.34) as seen in Figure 4.7, the spin $3^-$ state has more energy relative to the spin $4^+$ state. This is because the step potential gives the tetrahedral and square configurations the same energy. Hence the spin $3^-$ state, having to vanish at all flat square configurations, gains energy. The spin $2^+$ state, which is concentrated at the flat squares, becomes energetically favoured for the same reason. The highly vibrationally excited $0^-$ state has decreased its energy considerably, as claimed in Section 4.3.6. It now has energy 13.81 MeV, down from 15.79 MeV, and is much closer to the experimental $0^-$ state at 11.0 MeV.

Ideally the potential should favour the tetrahedron over the flat square configuration and flatten out asymptotically as well. It may be impossible to write down such a potential and keep the Schrödinger equation separable. Hence one would need to solve the full $2D$ equation numerically which is certainly within current computational limits. One could attempt to generate the potential from a more fundamental point of view. A possibility is to take configuration energies from an $\alpha$-cluster model such as the one studied in [10]. Another is to find a way to generate all the Skyrme configurations on $\mathcal{M}$, which requires a fuller understanding of the vibrational space of Skyrmions. However, if it were possible, the moments of inertia, metric on $\mathcal{M}$ and potential would all come from a single Lagrangian, making the proposition very attractive.
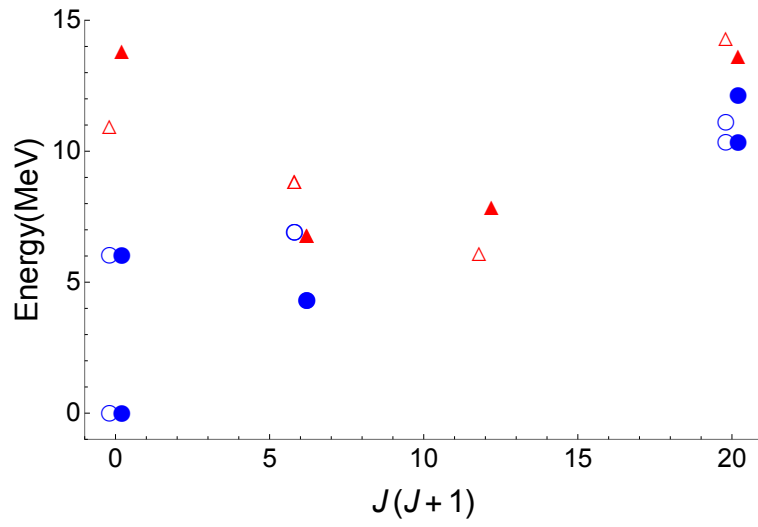
Figure 4.9: The low energy spectrum using the step potential (4.72). Calculated states of positive (solid circles) and negative (solid triangles) parity are plotted, alongside the experimental states (hollow shapes) that they describe.

# Chapter 5

# A Skyrme model approach to the spin-orbit force

*This chapter is based on the joint paper with N. S. Manton [67].*

## 5.1 Introduction

The spin-orbit force is a crucial ingredient in many parts of nuclear physics [68]. In the elementary shell model, nuclei are described as a collection of nucleons which do not directly interact. They only interact indirectly through an effective potential which gives rise to a one-particle Hamiltonian and consequently an energy spectrum. By the Pauli exclusion principle, levels of this energy spectrum are filled as the baryon number $B$ is increased. For special values of $B$, the spectrum hits a gap and the corresponding nucleus is tightly bound and very stable. These special values are called magic numbers and give rise to magic nuclei. The shell model works well near these. To obtain the correct magic numbers one must include a spin-orbit term in the single particle Hamiltonian [69, 70]. This couples the spin of a nucleon to its orbital angular momentum $l$. The inclusion of this term breaks the degeneracy between states with the same value of $|l|$. States with spin and orbital angular momentum aligned are energetically favoured.

For a nucleus with a few more nucleons than a magic number we can interpret its structure physically: a core made from a magic nucleus is surrounded by the

other nucleons orbiting it. If there is one orbiting nucleon, its spin and orbital angular momentum are aligned in all but two cases, Antimony-133 and Bismuth-209. As more nucleons are added, other factors such as pairing make the interpretation more complicated. The spin-orbit force is strongest near the surface of the core and its physical meaning is lost within the core.

Analogy with atomic physics points to an electromagnetic origin of the spin-orbit coupling but this turns out to have the wrong magnitude. The correct magnitude can be obtained by considering relativistic effects. They lead to a field theory where nucleons interact via mesons. The system can be solved approximately by neglecting quantum fluctuations of certain terms [71]. While this technique is successful, it ignores the structure of nucleons and requires one to fit several parameters. Ideally these parameters would come from experiment but as the theory is phenomenological, effective masses and coupling constants must be used [72].

The spin-orbit force is also present in nucleon-nucleon interactions. It couples the orbital angular momentum to the sum of the spins of the nucleons, and can also be thought of as coming from meson interactions. The asymptotic form of the force has been successfully reproduced in the Skyrme model using a product ansatz which is valid only when the Skyrmions are widely separated [73].

In this chapter we develop an idea in [74] which provides an explanation for the spin-orbit force at shorter separations, inspired by the Skyrme model. When two $B = 1$ Skyrmions are widely separated we can approximate their interaction using an asymptotic expansion. One finds that among all configurations there is a special submanifold of maximal attraction between the Skyrmions called the attractive channel [12]. This is easiest to interpret pictorially: in the attractive channel the separated Skyrmions have matching colours at the point of closest contact. Conversely, if the closest colours are opposite the Skyrmions repel.

Configurations tend to line up in the attractive channel in order to minimise potential energy. This concept remains useful for larger Skyrmions. In fact, in all of the dynamical modes discussed in this thesis, the Skyrmions remain in the attractive channel. This can be seen in Figures 3.4 and 4.2. As another example, consider the configuration in Figure 5.1. Here, a $B = 1$ Skyrmion is orbiting a $B = 6$ Skyrmion. The system is shown in the attractive channel with red on both Skyrmions at their contact point. To stay in the attractive channel as it orbits, the $B = 1$ Skyrmion must take a special orbital path. Specifically, it rolls around

the equator of the larger solution completing three full rotations on its axis before returning to the initial position. The key observation is that the $B = 1$ Skyrmions' orbital angular momentum is aligned with its spin. This is exactly what is required for the spin-orbit force in nuclei with $B$ one more than a magic number, except in the cases of Antimony-133 and Bismuth-209. It is the classical pion field structure of Skyrmions that provides the microscopic origin for the coupling. Many other Skyrmion pairs have paths like this which encourage spin-orbit coupling. The effect becomes stronger when the Skyrmions are closer together but loses meaning if they were to merge fully. This is consistent with the fact that the traditional spin-orbit force is strongest near the surface of the core nucleus.
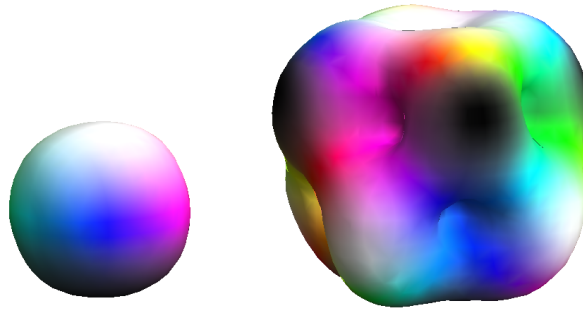


Figure 5.1: A $B = 1$ Skyrmion close to a $B = 6$ Skyrmion. The colours of closest contact are both red (unseen on the $B = 1$ solution from this viewpoint) so the configuration is in the attractive channel.

We will now try to work out the consequences of this classical spin-orbit coupling when the system is quantised. The usual procedure for quantising one Skyrmion is to apply rigid body quantisation to the classical minimal energy configuration, as seen in Chapter 2. Quantising the interaction between separated Skyrmions is more difficult and little progress has been possible on a larger vibrational manifold, apart from the work in this thesis and [32]. Thus, we will only consider a toy model in two dimensions where we treat the Skyrmions as rigid discs. This can be thought of in terms of the vibrational manifold picture as follows: we postulate there is a low energy valley in the vibrational manifold, away from the energy minimising Skyrmion itself. In this valley, the Skyrme configuration looks like a $B = 1$ Skyrmion orbiting a larger Skyrmion. The one-dimensional set of configurations in this valley are local minima of the vibrational manifold. We will

begin by carefully considering the simplest system possible: the interaction of two $B = 1$ Skyrmions.

## 5.2 Discs interacting through a contact potential

### 5.2.1 Two discs of equal size

Our model is based on taking 2D slices of 3D Skyrme configurations, taking our inspiration from $B = 1$ Skyrmion interactions. Figure 5.2a shows separated $B = 1$ solutions in the attractive channel. We can take a 2D slice of this parallel to the $y$-$z$ plane and parallel to the $x$-$y$ plane to give us the systems in Figures 5.2b and 5.2c. We now treat these 2D objects as rigid discs, at fixed separation, interacting through a potential which depends only on their colouring.
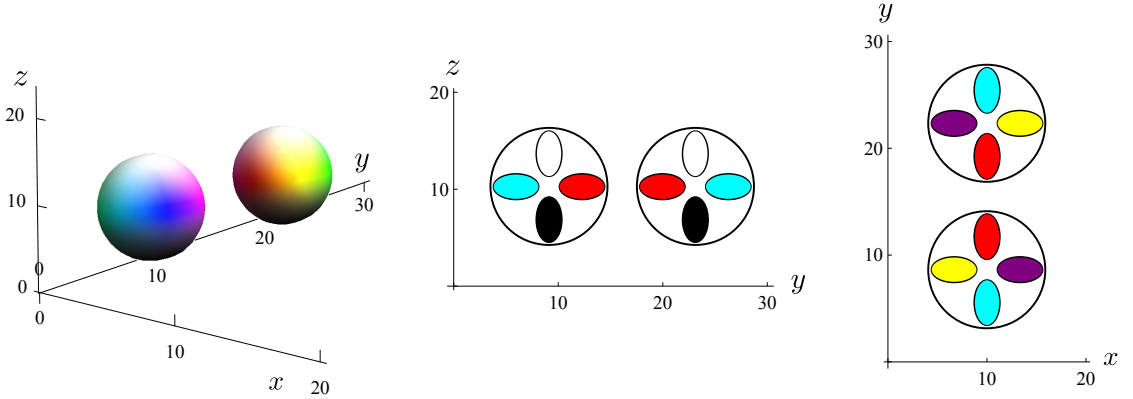


Figure 5.2: (a) Two $B = 1$ Skyrmions in the attractive channel. (b) The rolling configuration. (c) The sliding configuration

To remain in the attractive channel the discs in Figures 5.2b and 5.2c must roll and slide around each other respectively. For now, we will consider the rolling configuration. Labelling the discs as 1 and 2 we introduce the angular coordinates as in Figure 5.3. The angles $\alpha_1$ and $\alpha_2$ represent the orientation of the discs with respect to their own axes. These are measured anti-clockwise and are zero when white points up, as in Figure 5.2b. The coordinate $\beta$ labels the orbital orientation of the discs while $r$ is the (fixed) distance between the disc centres.

Each of the coordinates has range $2\pi$ but $\beta \to \beta + \pi$ also returns the system to the attractive channel. As such, the potential must be periodic under full rotations

106
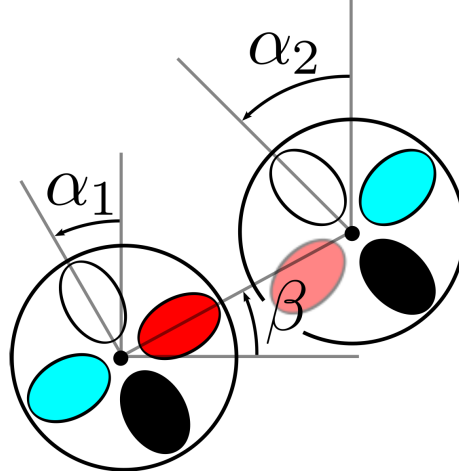
Figure 5.3: The angles $\alpha_1$, $\alpha_2$ and $\beta$.

of either disc and under half an orbital rotation. It should also only depend on the colouring: the simplest choice is a cosine potential. Thus, a classical Lagrangian which describes the system is

$$L = \frac{1}{2}I_1\dot{\alpha}_1^2 + \frac{1}{2}I_2\dot{\alpha}_2^2 + \frac{1}{2}\mu r^2\dot{\beta}^2 + k\cos(2\beta - \alpha_1 - \alpha_2) \tag{5.1}$$

where $I_1$, $I_2$ are the disc moments of inertia, $\mu$ is the reduced mass of the system and $k > 0$ is the strength of the potential. The argument of the potential measures the difference in colour at the closest points. The discs are identical so $I_1 = I_2 = I$ and we may write $\mu r^2$ in terms of $I$ by introducing a dimensionless separation parameter $d$ and setting $\mu r^2 = 4d^2 I$. This simplifies the Lagrangian to

$$L = \frac{1}{2}I\left(\dot{\alpha}_1^2 + \dot{\alpha}_2^2 + 4d^2\dot{\beta}^2\right) + k\cos(2\beta - \alpha_1 - \alpha_2). \tag{5.2}$$

Classically, the lowest energy solution satisfies $2\beta - \alpha_1 - \alpha_2 = 0$. This forces the discs into the attractive channel as if they were cogwheels; the first cog rolls around the second, fixed cog. If they stay in the attractive channel for all time, we can differentiate this condition to obtain a relation between velocities: $2\dot{\beta} - \dot{\alpha}_1 - \dot{\alpha}_2 = 0$. Introducing the classical conjugate momenta to the coordinates

$$s_1 = I\dot{\alpha}_1\,,\ s_2 = I\dot{\alpha}_2 \text{ and } l = 4d^2 I\dot{\beta}\,, \tag{5.3}$$

we can rewrite the above velocity relation as

$$l - 2d^2(s_1 + s_2) = 0\,. \tag{5.4}$$

107

Hence, the classical angular momentum and the sum of spins are aligned. Later we will see that this combination of spins and angular momentum has an important role to play in the quantum picture too.

The Lagrangian (5.2) has two linearly independent continuous symmetries. The first corresponds to all angles increasing by the same amount. This leads to conservation of total angular momentum

$$\mathcal{J} = I\left(\dot{\alpha}_1 + \dot{\alpha}_2 + 4d^2\dot{\beta}\right) = s_1 + s_2 + l\,. \tag{5.5}$$

The other conserved quantity is generated by one disc spinning at the same speed as the other but in the opposite direction. Since this quantity can be interpreted purely in terms of the colour fields moving, we label it as the total isospin in analogy with the full Skyrme model. It has the form

$$\mathcal{I} = I\left(\dot{\alpha}_1 - \dot{\alpha}_2\right) = s_1 - s_2\,. \tag{5.6}$$

We can take advantage of these symmetries by changing coordinates and reducing the problem's degrees of freedom from three to one. Before doing this, we should consider the discrete symmetries of the system which occur since the configuration space is a 3-torus. First let us solve the problem for $k = 0$ where the Hamiltonian becomes that of a free particle on a 3-torus. After canonical quantisation, the Hamiltonian has the form

$$\hat{\mathcal{H}} = -\frac{1}{2I}\left(\frac{\partial^2}{\partial\alpha_1^2} + \frac{\partial^2}{\partial\alpha_2^2} + \frac{1}{4d^2}\frac{\partial^2}{\partial\beta^2}\right)\,, \tag{5.7}$$

where we have set $\hbar = 1$. The wavefunction has the form

$$\psi_{\text{free}}\left(\alpha_1, \alpha_2, \beta\right) = e^{i(s_1\alpha_1 + s_2\alpha_2 + l\beta)}\,, \tag{5.8}$$

with corresponding energy

$$E_{\text{free}} = \frac{1}{2I}\left(s_1^2 + s_2^2 + \frac{1}{4d^2}l^2\right)\,. \tag{5.9}$$

The quantities $s_1$, $s_2$ and $l$ are the quantum numbers corresponding to the spins and orbital angular momentum of the free discs. As we are modelling Skyrmions, the discs are treated as fermions. Thus, the wavefunction picks up a minus sign under full disc rotations: $\alpha_1 \to \alpha_1 + 2\pi$ and $\alpha_2 \to \alpha_2 + 2\pi$. This means $s_1$ and

$s_2$ are both half-integers. The system is also invariant under $\beta \to \beta + 2\pi$ and as such $l$ must be an integer. While these quantities do not remain good quantum numbers when the potential is turned on, they do remain important due to Bloch's theorem. This says that there exists a basis of energy eigenstates of the form

$$\psi\left(\alpha_1, \alpha_2, \beta\right) = e^{i(s_1\alpha_1 + s_2\alpha_2 + l\beta)} u\left(\alpha_1, \alpha_2, \beta\right), \tag{5.10}$$

where $u$ is periodic on the 3-torus, and has the same periodicity as the potential. This theorem is generally used in an infinite lattice but we are on a torus. As such $s_1$, $s_2$ and $l$ have discrete allowed values instead of continuous ones. They are also usually defined up to a vector in the reciprocal lattice, a discrete lattice in 3D. However we fix their value by insisting that

$$u\left(\alpha_1, \alpha_2, \beta\right)|_{k=0} \equiv 1. \tag{5.11}$$

There is one state per cell in the reciprocal lattice. Thus we can understand $s_1$, $s_2$ and $l$ as labelling a particular lattice cell. We will see later that energy states from different cells do not cross when the potential is turned on and as such these labels are good for tracking the energy states as $k$ increases.

To make progress we must now change coordinates to take advantage of the continuous symmetries from earlier. We introduce new coordinates $(\gamma, \xi, \eta)$. Two of these should give rise to the conjugate momenta corresponding to $\mathcal{J}$ and $\mathcal{I}$. That is

$$-i\frac{\partial}{\partial \xi} = -i\left(\frac{\partial}{\partial \alpha_1} + \frac{\partial}{\partial \alpha_2} + \frac{\partial}{\partial \beta}\right) \tag{5.12}$$

$$-i\frac{\partial}{\partial \eta} = -i\left(\frac{\partial}{\partial \alpha_1} - \frac{\partial}{\partial \alpha_2}\right). \tag{5.13}$$

Note that these operators commute with the potential in (5.2). We may define $\gamma$ to be the coordinate in the potential. If we also insist on a diagonal quadratic kinetic term in the Hamiltonian we arrive at a unique coordinate transformation

$$\begin{pmatrix} \gamma \\ \xi \\ \eta \end{pmatrix} = \begin{pmatrix} -1 & -1 & 2 \\ \frac{1}{2+4d^2} & \frac{1}{2+4d^2} & \frac{4d^2}{2+4d^2} \\ \frac{1}{2} & -\frac{1}{2} & 0 \end{pmatrix} \begin{pmatrix} \alpha_1 \\ \alpha_2 \\ \beta \end{pmatrix}. \tag{5.14}$$

This transforms the Hamiltonian to

$$\hat{\mathcal{H}} = -\frac{1}{2I}\left(\frac{1+2d^2}{d^2}\frac{\partial^2}{\partial \gamma^2} + \frac{1}{2+4d^2}\frac{\partial^2}{\partial \xi^2} + \frac{1}{2}\frac{\partial^2}{\partial \eta^2}\right) - k\cos\gamma. \tag{5.15}$$

Since the $\xi$ and $\eta$ contributions are purely kinetic, the wavefunction has the form

$$\psi(\gamma, \eta, \xi) = e^{i\mathcal{J}\xi} e^{i\mathcal{I}\eta} \chi(\gamma). \tag{5.16}$$

Moreover, after applying the coordinate transformation, comparison with (5.8) and (5.10) tells us that

$$\mathcal{J} = s_1 + s_2 + l, \tag{5.17}$$

$$\mathcal{I} = s_1 - s_2 \tag{5.18}$$

as in the classical equations (5.5) and (5.6), and that

$$\chi(\gamma) = e^{iq_\gamma \gamma} \tilde{u}(\gamma), \tag{5.19}$$

where

$$q_\gamma = \frac{1}{2 + 4d^2} \left( l - 2d^2(s_1 + s_2) \right) \tag{5.20}$$

and $\tilde{u}(\gamma)$ has period $2\pi$. Once again, we fix $q_\gamma$ so that $\tilde{u}|_{k=0} \equiv 1$. From earlier, we find that $\mathcal{I}$ and $\mathcal{J}$ can take any integer values. The free system now has the wavefunction

$$\psi_{\text{free}}(\gamma, \eta, \xi) = e^{i\mathcal{J}\xi} e^{i\mathcal{I}\eta} e^{iq_\gamma \gamma}, \tag{5.21}$$

with corresponding energy

$$E_{\text{free}} = \frac{1 + 2d^2}{2d^2 I} q_\gamma^2 + \frac{1}{(4 + 8d^2)I} \mathcal{J}^2 + \frac{1}{4I} \mathcal{I}^2. \tag{5.22}$$

For fixed $\mathcal{J}$ and $\mathcal{I}$, the allowed values of $q_\gamma$ are separated by integers, though the fractional part of $q_\gamma$ depends on $d$ and $\mathcal{J}$. Combining everything, the problem reduces to the Schrödinger equation

$$-\frac{1 + 2d^2}{2d^2 I} \frac{d^2}{d\gamma^2} \left( e^{iq_\gamma \gamma} \tilde{u} \right) - k \cos\gamma\, e^{iq_\gamma \gamma} \tilde{u} = \left( E - \frac{\mathcal{J}^2}{(4 + 8d^2)I} - \frac{\mathcal{I}^2}{4I} \right) e^{iq_\gamma \gamma} \tilde{u} \tag{5.23}$$

$$\equiv E_\gamma e^{iq_\gamma \gamma} \tilde{u}. \tag{5.24}$$

This is the Mathieu equation, which has been extensively studied [76]. We will now consider it with our physical picture in mind. The energy has separated into two parts – one depends on $\mathcal{J}$ and $\mathcal{I}$ and has no $k$ dependence. The other only depends on the $\gamma$ sector. The potential does not mix states with different $\mathcal{I}$ and $\mathcal{J}$. Thus, we can fix these values and focus on calculating $E_\gamma$.

We can understand the system when $k$ is small by using perturbation theory. Note that the dimensionless small quantity is really $kI$. The energy, to second order in $kI$ is

$$E_{\gamma,\text{pert}} = \frac{1 + 2d^2}{2d^2 I} q_\gamma^2 + (kI)^2 \frac{d^2}{(1 + 2d^2)I} \frac{1}{4q_\gamma^2 - 1} \ . \tag{5.25}$$

The most important thing to note is that for fixed $\mathcal{J}$ and $\mathcal{I}$, since the allowed values of $q_\gamma$ are separated by integers, there is a unique state which satisfies $4q_\gamma^2 - 1 < 0$. Thus there is one state whose energy decreases after perturbation, with $|q_\gamma| \leq \frac{1}{2}$. We call states which satisfy this condition energetically favourable. At $|q_\gamma| = \frac{1}{2}$ equation (5.25) breaks down and degenerate perturbation theory must be used. It tells us that the energy spectrum develops a gap at each of these points leaving a separated energy band for $|q_\gamma| < \frac{1}{2}$ which does not touch the rest of the spectrum.

The other degenerate points ($|q_\gamma| = 1, \frac{3}{2}, 2...$) lead to singularities in the perturbative energy spectrum at higher orders. Degenerate perturbation theory tells us, once again, that a gap occurs at each of these points. Thus after perturbation we are left with an energy spectrum divided into non-touching bands as seen in Figure 5.4. Degenerate points are identified and as such each band is an integer long. For example, one of the bands is $q_\gamma \in [-1, -\frac{1}{2}] \cup [\frac{1}{2}, 1]$. Since the allowed values of $q_\gamma$ are separated by an integer there is exactly one state per band. This explains why $q_\gamma$ is a good label: due to the gaps in the spectrum we can follow a free state as $k$ increases without having to worry about crossing except at degenerate points. Even there, the uncertainty is only between two states and most degeneracies only occur for special values of $d$. As such, we won't consider them carefully.

For large $k$ we may use a tight binding (tb) limit. This approximation relies on the wavefunction being concentrated within each unit cell in $\gamma$ with negligible overlap. Then the total wavefunction can be written as a sum of isolated wavefunctions which solve Schrödinger's equation within the unit cell. These isolated wavefunctions must be the same at each site due to the periodicity of $\tilde{u}$. Bloch's theorem allows for the total wavefunction to pick up a phase between cells meaning the solution of (5.23) is of the form

$$e^{iq_\gamma \gamma} \tilde{u}_{\text{tb}}(\gamma) = \sum_{m \in \mathbb{Z}} \phi(\gamma - 2\pi m) e^{2\pi i L m} \ , \tag{5.26}$$
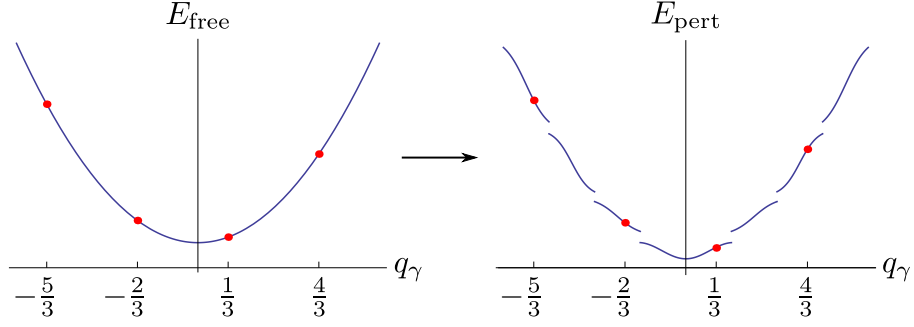
Figure 5.4: How the energy spectrum changes after perturbation. $E_{\text{free}}$ is the spectrum for $k = 0$; $E_{\text{pert}}$ is the spectrum for small $kI$. The dots represent an example of an allowed value of $q_\gamma$. In this case we take $(\mathcal{I}, \mathcal{J}) = (0, 1)$ and $d = 1$ which gives $q_\gamma \equiv \frac{1}{3} (\text{mod } 1)$. Note that there is one allowed state per separated band.

where $\phi$ is the isolated wavefunction and $L$ is some constant. The periodicity of $\tilde{u}$ fixes $L$ to be $q_\gamma$. Thus our total, tight binding wavefunction is

$$\psi_{\text{tb}}(\gamma, \xi, \eta) = e^{i\mathcal{J}\xi} e^{i\mathcal{I}\eta} \sum_{m \in \mathbb{Z}} \phi(\gamma - 2\pi m) e^{2\pi i m q_\gamma} \,. \tag{5.27}$$

We are left to find $\phi$. Since $k$ is large, we assume that the wavefunction is concentrated near the minimum of the potential. We can expand the potential near this point, which gives

$$- k \cos \gamma \approx -k \left( 1 - \frac{\gamma^2}{2} + \frac{\gamma^4}{4!} \right) \tag{5.28}$$

and reduces the Schrödinger equation (5.23) to

$$- \frac{1 + 2d^2}{2d^2 I} \frac{d^2 \phi}{d\gamma^2} - k \left( 1 - \frac{\gamma^2}{2} + \frac{\gamma^4}{24} \right) \phi = E_\gamma \phi \,, \tag{5.29}$$

where $kI$ is large. If we temporarily ignore the $\gamma^4$ term in the potential then this truncated Schrödinger equation is just a simple harmonic oscillator which can be solved by standard methods. The non-normalised eigenstates are given by

$$\phi_N(\gamma) = H_N \left( \left( \frac{kd^2 I}{1 + 2d^2} \right)^{\frac{1}{4}} \gamma \right) \exp \left( - \left( \frac{kd^2 I}{4 + 8d^2} \right)^{\frac{1}{2}} \gamma^2 \right) , \tag{5.30}$$

where $H_N$ are the Hermite polynomials. We can then use these to find the energies to $O(1)$ in $k$. They are

$$E_{\gamma,n} = -k + \sqrt{k}\sqrt{\frac{1+2d^2}{d^2 I}}\left(N + \frac{1}{2}\right) - \frac{1+2d^2}{32d^2 I}\left(2N^2 + 2N + 1\right) + O\left(\frac{1}{\sqrt{k}}\right).$$

$$(5.31)$$

The $O(k)$ term is from the constant in the potential. The $O(\sqrt{k})$ term is the usual harmonic oscillator energy, and the $O(1)$ term is the contribution from the $\gamma^4$ term in the potential, evaluated by first order perturbation theory. We have ignored all overlap terms between cells, but these are exponentially suppressed for large enough $k$.

Due to the lattice structure, the labels we used for the free states continue to label the states in the tight binding limit. Since there is no crossing for fixed $\mathcal{I}$ and $\mathcal{J}$, the $N^{\text{th}}$ excited free state (which has the label $q_\gamma$ where $q_\gamma \in [-\frac{N+1}{2}, -\frac{N}{2}] \cup [\frac{N}{2}, \frac{N+1}{2}]$) flows smoothly to the state labelled by $N$ in the tight binding limit. This is confirmed by numerical calculations as seen in Figure 5.5, which shows the analytic and numerical energies as a function of $k$ for the four lowest energy states for fixed $(\mathcal{I}, \mathcal{J}) = (0, 1)$. The eigenvalues $E_\gamma$ are found using a shooting method.

From the numerical data in Figure 5.5 we see that the analytic expressions (5.25) and (5.31) have different regions of validity depending on which state we examine. We can explain this as follows. The large $k$ calculation relied on two approximations: that the wavefunction is concentrated within a unit cell and that it is concentrated within a region where we may expand the potential to quartic order. If we satisfy the second constraint we certainly satisfy the first so we shall examine the second. The expansion (5.28) is, very roughly, good for $|\gamma| < 2$. Thus, we need the wavefunction to be decaying exponentially there. For large $\gamma$, $\phi_n$ is of the form

$$\phi_N \sim \gamma^N \kappa^{\frac{N}{4}} \exp\left(-\frac{\gamma^2}{2}\kappa^{\frac{1}{2}}\right)$$

$$= \exp\left(N\log\gamma + \frac{N}{4}\log\kappa - \frac{\gamma^2 \kappa^{\frac{1}{2}}}{2}\right), \qquad (5.32)$$

where we have defined $\kappa = \frac{kd^2 I}{1+2d^2}$. For the wavefunction to be concentrated within $-2 < \gamma < 2$ we require

$$N\log 2 + \frac{N}{4}\log\kappa - 2\kappa^{\frac{1}{2}} < -c, \qquad (5.33)$$

113
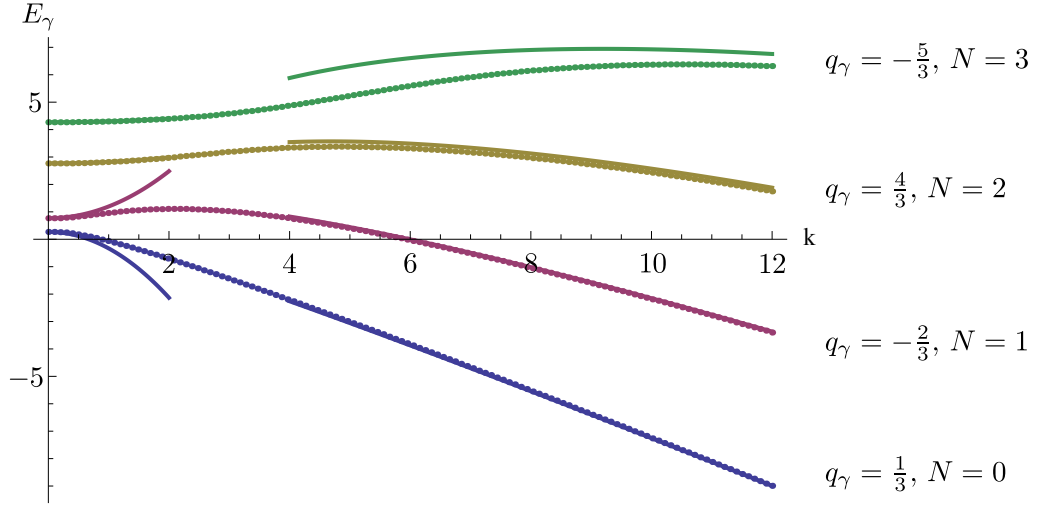
Figure 5.5: The energy spectrum for $(\mathcal{I}, \mathcal{J}) = (0, 1)$ and $d = 1$ as $k$ varies. As in Figure 5.4, these values give $q_\gamma \equiv \frac{1}{3}(\text{mod } 1)$. Our analytic expressions are represented by the bold lines while numerical results are displayed as dots. The $N^{\text{th}}$ excited free state (and thus the free state in the $N^{\text{th}}$ band) flows to the $N^{\text{th}}$ excited state of the tight binding limit.

where $c$ is some positive constant. We see that as $N$ increases we need a larger $\kappa$, and hence $kI$, for our approximation to be valid, as the numerical results confirm.

The regions of validity of the small $k$ perturbative energy expansion (5.25) can be explained by calculating the next non-trivial term. It is

$$k^4 \frac{(d^2 I)^3}{(1 + 2d^2)^3} \frac{20q_\gamma^2 + 7}{(4q_\gamma^2 - 1)^3(4q_\gamma^2 - 4)} . \tag{5.34}$$

Away from degenerate points, this goes as $k^4 q_\gamma^{-6}$ and as such is small for states with large $q_\gamma$. This explains why the perturbative energy calculation works for a larger range of $k$ for states with larger $q_\gamma$.

The problem has now been solved in both small and large $k$ limits. Thanks to the lattice structure we can extrapolate the free states to the large $k$ states without fear of crossing between states. We have found that the energetically favourable states in the large $k$ limit come from free states which satisfy

$$|q_\gamma| = \frac{1}{2 + 4d^2} \left| l - 2d^2 \left( s_1 + s_2 \right) \right| \leq \frac{1}{2} . \tag{5.35}$$

This is our form of spin-orbit coupling. States with orbital angular momentum

and spins aligned are more likely to satisfy the inequality while they are less likely to if they are anti-aligned. Note the connection between the classical minimum energy condition (5.4) and our energetically favourable state condition (5.35). To be more definite let us fix the spins of the discs to be $\pm\frac{1}{2}$. Then $s_1 + s_2$ can be $1, 0$ or $-1$. Take $s_1 + s_2 = 1$ first. Energetically favoured states satisfy

$$|l - 2d^2| \leq 1 + 2d^2 . \tag{5.36}$$

Thus these states have orbital angular momentum $l \in [-1, 1 + 4d^2]$. As $l$ is usually positive, spin and orbital angular momentum are usually aligned. The extreme case, $l = -1$, corresponds to a degenerate point in the energy spectrum. Here, our labels lose meaning and we cannot distinguish between the free states $(s_1, s_2, l) = (\frac{1}{2}, \frac{1}{2}, -1)$ and $(s_1, s_2, l) = (-\frac{1}{2}, -\frac{1}{2}, 1)$ as the potential is turned on. Both of these have spin and orbital angular momentum anti-aligned. The result is essentially the same for $s_1 + s_2 = -1$. Here $l$ is always non-positive, except for the degenerate state. As this example demonstrates, the direction of the spins is correlated with the direction of the orbital angular momentum for most of the energetically favoured states. When $s_1 + s_2 = 0$ the condition (5.35) reduces to

$$|l| \leq 1 + 2d^2 . \tag{5.37}$$

This time there is no spin-orbit coupling as the orbital angular momentum has no preferred direction. Figure 5.6 displays how the energy spectrum changes as $k$ is turned on for the lowest energy states which satisfy $\mathcal{I} = 0$ and $s_1 = \frac{1}{2}$. We focus on these states as this is where the spin-orbit force is present in our model. Note that states with equal $|l|$ in the free case become non-degenerate for positive $k$, just as they do in traditional spin-orbit coupling. For this figure, we take $I = 1$, $d = 0.9$, with $d$ not equal to 1 so that we avoid certain degeneracies.

In the large $k$ limit only those states which came from free states with $|q_\gamma| \leq \frac{1}{2}$ are contenders for the ground state. These are then ordered by the $\mathcal{I}, \mathcal{J}$ energy contribution. This limit is exactly rigid body quantisation and in the strict limit the wavefunction is a delta function, the system completely fixed in the attractive channel. Physically, we expect the true strength of $k$ to be between the two limits we understand analytically. This is also seen in the traditional spin-orbit force: the coupling is strong enough that it has an effect on the energy spectrum but weak enough that an understanding of the spectrum without the force is vital too.
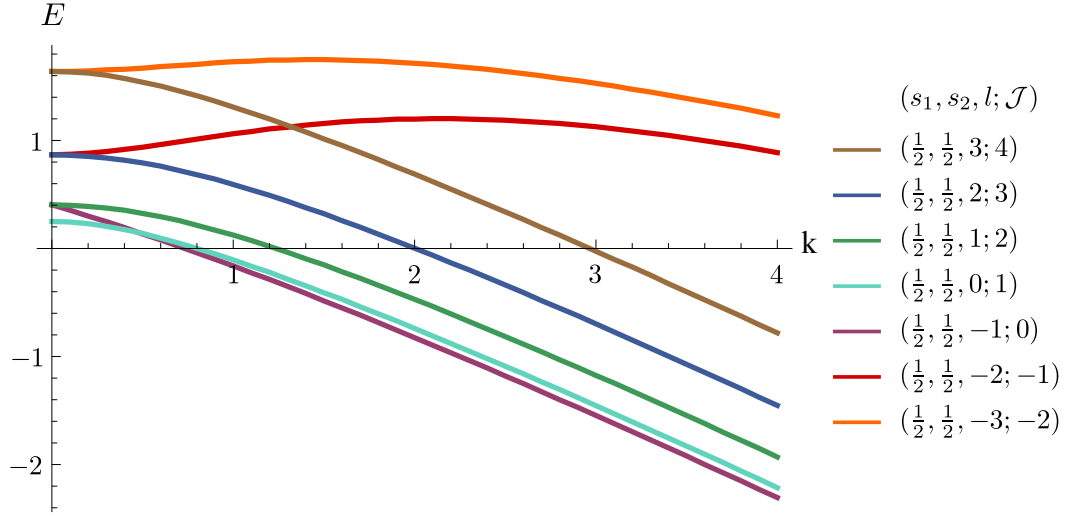
Figure 5.6: The energy spectrum for some low lying states with various values of $\mathcal{J}$, with $\mathcal{I} = 0$ and $s_1 = \frac{1}{2}$. Each is labelled by their $(s_1, s_2, l; \mathcal{J})$ value at $k = 0$. In all but the extreme case, $l = -1$, the energetically favoured states have spin and orbital angular momentum aligned.

We may do an analogous calculation for the sliding configuration from Figure 5.2c. The calculation is very similar to the one above and the main physical consequence is that the energetically favoured states come from free states with small $s_1 - s_2$. Thus, the sliding configuration couples the spins. This is what is required for the tensor force – another key ingredient in nucleon-nucleon interactions. Thus, our model unifies the spin-orbit force and the tensor force while giving them both a classical microscopic origin. In the full 3D model both sliding and rolling motion can occur simultaneously and both need to be taken into account at the same time.

## 5.2.2 Unequal discs

Consider a generalisation of the system. Now a small disc orbits a larger one as seen in Figure 5.7, with small and large discs labelled 1 and 2 respectively. Let the colour field repeat $n$ times along the edge of the large disc. This is a model for a nucleus with baryon number one more than a magic number, with a single nucleon orbiting the core. The core is generally a boson and this is how we treat the large disc. Defining our variables analogously to the variables in the previous

section and using the initial configuration as in Figure 5.7, the Lagrangian (5.2) is modified to

$$L = \frac{1}{2}I_1\dot{\alpha}_1^2 + \frac{1}{2}I_2\dot{\alpha}_2^2 + \frac{1}{2}\mu r^2\dot{\beta}^2 + k\cos\left((n+1)\beta - \alpha_1 - n\alpha_2\right) . \qquad (5.38)$$
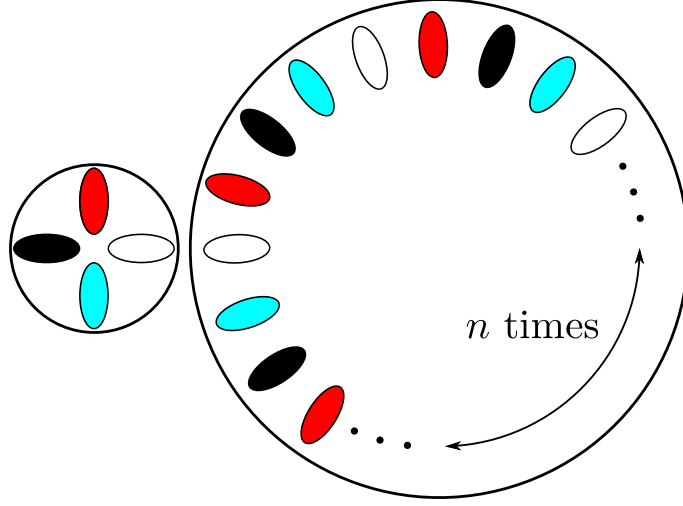


Figure 5.7: A small disc orbiting a large disc.

The classical conserved quantities are now

$$\mathcal{J} = I_1\dot{\alpha}_1 + I_2\dot{\alpha}_2 + \mu r^2\dot{\beta} = s_1 + s_2 + l\,, \qquad (5.39)$$

$$\mathcal{I} = nI_1\dot{\alpha}_1 - I_2\dot{\alpha}_2 = ns_1 - s_2\,. \qquad (5.40)$$

We are using the same notation as before: $l$ is the orbital angular momentum while $s_i$ is the spin of disc $i$. The classical minimum energy solution is when the discs are locked in the attractive channel and thus act like cogwheels. This gives a condition on the classical momenta of the system as follows

$$I_1I_2(n+1)l - I_2\mu r^2 s_1 - I_1\mu r^2 n s_2 = 0\,. \qquad (5.41)$$

We can change coordinates so that the potential depends on one angle, $\gamma$, while the others are conjugate to $\mathcal{J}$ and $\mathcal{I}$. Further, we can insist that the Hamiltonian splits into two independent sectors (one depending only on $\mathcal{J}$ and $\mathcal{I}$, the other

determined purely by the $\gamma$ sector) as we did in the previous section. Once again, this gives a unique coordinate transformation

$$\begin{pmatrix} \gamma \\ \xi \\ \eta \end{pmatrix} = \begin{pmatrix} -1 & -n & n+1 \\ \frac{I_1 I_2 (n+1)}{C} & \frac{I_1 I_2 n(n+1)}{C} & \frac{\mu r^2 (I_2 + I_1 n^2)}{C} \\ \frac{I_1 (I_2 + I_2 n + \mu r^2 n)}{C} & -\frac{I_2 (I_1 + I_1 n + \mu r^2)}{C} & \frac{\mu r^2 (I_2 - I_1 n)}{C} \end{pmatrix} \begin{pmatrix} \alpha_1 \\ \alpha_2 \\ \beta \end{pmatrix}, \tag{5.42}$$

where $C = I_1 I_2 (n+1)^2 + I_1 \mu r^2 n^2 + I_2 \mu r^2$. This, combined with Bloch's theorem gives us the form of the wavefunction after canonical quantisation. It is

$$\psi(\gamma, \eta, \xi) = e^{i\mathcal{J}\xi} e^{i\mathcal{I}\eta} e^{i q_\gamma \gamma} \tilde{w}(\gamma). \tag{5.43}$$

where $\tilde{w}$ has period $2\pi$ and $q_\gamma = (I_1 I_2 (n+1)l - I_2 \mu r^2 s_1 - I_1 \mu r^2 n s_2) C^{-1}$. Since the small disc is a fermion, $s_1$ must be a half-integer while $s_2$ and $l$ are both integers. Once again, the allowed values of $q_\gamma$ are separated by an integer. The Schrödinger equation is now

$$-\frac{C}{2 I_1 I_2 \mu r^2} \frac{d^2}{d\gamma^2} \left( e^{i q_\gamma \gamma} \tilde{w} \right) - k \cos \gamma \, e^{i q_\gamma \gamma} \tilde{w} = E_\gamma e^{i q_\gamma \gamma} \tilde{w}, \tag{5.44}$$

where the energy of the system is

$$E = E_\gamma + \frac{I_1 n^2 + I_2}{2C} \mathcal{J}^2 + \frac{I_2 - I_1 n}{C} \mathcal{I}\mathcal{J} + \frac{I_1 + I_2 + \mu r^2}{2C} \mathcal{I}^2 \tag{5.45}$$

$$\equiv E_\gamma + E_{\mathcal{I}, \mathcal{J}}. \tag{5.46}$$

This is simply equation (5.23) with an adjusted mass. Thus we may apply all our analysis from the previous section to this problem; namely we can reuse the equations (5.25) to (5.31) with the replacement

$$\frac{1 + 2d^2}{d^2 I} \to \frac{C}{I_1 I_2 \mu r^2}. \tag{5.47}$$

The physical consequence is that when $k$ is increased, the energetically favourable states have small

$$q_\gamma = \frac{1}{I_1 I_2 (n+1)^2 + I_1 \mu r^2 n^2 + I_2 \mu r^2} \left( I_1 I_2 (n+1)l - I_2 \mu r^2 s_1 - I_1 \mu r^2 n s_2 \right). \tag{5.48}$$

Note the relationship between this and the classical condition (5.41).

To gain more insight we must estimate the moments of inertia. First we assume that the circumference of the large disc is $n$ times the circumference of the small one. Then we use the Skyrmion inspired approximation that the radius of a disc with baryon number $B$ scales as $B^{\frac{1}{3}}$ and that its mass scales linearly with $B$. Finally, we assume that the discs are touching. These give us $I_2$ and $\mu r^2$ in terms of $I_1$ as follows

$$I_2 = n^5 I_1 \,, \quad \mu r^2 = \frac{2n^3}{n^3+1}(n+1)^2 I_1 \,. \tag{5.49}$$

It follows that

$$\frac{C}{I_1 I_2 \mu r^2} = \frac{3}{2I_1}\frac{n^3+1}{n^3} \tag{5.50}$$

and

$$q_\gamma = \frac{1}{3(n+1)}\left(l - \frac{2n^3}{n^2-n+1}s_1 - \frac{2}{n(n^2-n+1)}s_2\right) \,. \tag{5.51}$$

In (5.41) we saw that the classical minimum energy solution obeyed $q_\gamma = 0$. Consider spin/orbital angular momentum states which obey this. If we also demand that the core is inert ($s_2 = 0$) then $l$ scales as $2ns_1$ for large $n$. This gives a natural explanation why orbital angular momentum increases as the size of the core increases, a relationship obeyed by the first few magic nuclei.

We also see that if $s_2$ is non-zero, its contribution does not have much effect on the value of $q_\gamma$; the most important contribution is from the first two terms. Naively this looks promising: after quantisation, energetically favoured states obey $|q_\gamma| \leq \frac{1}{2}$ and this can be achieved by having $s_1$ and $l$ aligned. However, the number of energetically favoured states is rather large. To be concrete, let us fix $s_1 = \frac{1}{2}$ and $s_2 = 0$ from now on. Then

$$q_\gamma = \frac{1}{3(n+1)}\left(l - \frac{n^3}{n^2-n+1}\right) \,. \tag{5.52}$$

To satisfy $|q_\gamma| \leq \frac{1}{2}$ we require

$$l \in \left[-\frac{n^3+3}{2(n^2-n+1)}, \frac{5n^3+3}{2(n^2-n+1)}\right] \,. \tag{5.53}$$

Thus, the restriction to energetically favourable states is in fact not very limiting and the range of allowed values of $l$ grows with $n$. The centre of this range corresponds to the classical minimum energy solution, $q_\gamma = 0$. In the $k = 0$ limit the states are ordered by $|l|$. As $k$ increases we become more interested in

119

the energetically favoured states. These are ordered, in the extreme large $k$ limit, by $E_{\mathcal{I},\mathcal{J}}$. In terms of $l$ this quantity is

$$E_{\mathcal{I},\mathcal{J}} = \frac{1}{24 I_1 n^3 (n^3+1)} \left( 4l^2 \left(n^2 - n + 1\right)^2 + 4ln^3 \left(n^2 - n + 1\right) + n^3 \left(n^3 + 3\right) \right)$$

$$= \frac{1}{24 I_1 n^3 (n^3+1)} \left( 4(n^2 - n + 1)^2 \left( l + \frac{n^3}{2(n^2 - n + 1)} \right)^2 + 3n^3 \right) . \quad (5.54)$$

This means that the states are ordered energetically by the magnitude of $|l + \frac{n^3}{2(n^2-n+1)}|$. From comparison with (5.53) we see that the state with minimal $E_{\mathcal{I},\mathcal{J}}$ lies within the energetically favoured range of $l$ values. Thus the ground state of the system in the large $k$ limit has spin and orbital angular momentum anti-aligned as $l$ is negative, going against our classical intuition.
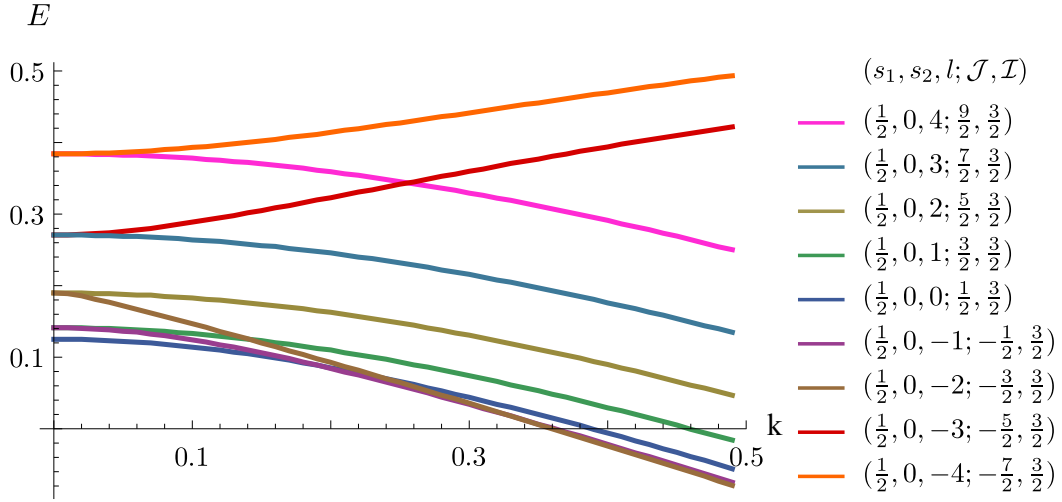


Figure 5.8: Energy for a variety of low lying states of unequal discs with $n = 3$, as a function of $k$. Here all states with $s_1 = \frac{1}{2}$, $s_2 = 0$ and $l \in [-4, 4]$ are shown. For large $|l|$ the states with $s_1$ and $l$ aligned are favoured. However for small $|l|$, the opposite is true.

Let us consider $n = 3$ in detail to illustrate these points more concretely. Here, there are twelve energetically favoured states, with $l \in [-2, 9]$. Two of these have $l$ and $s_1$ anti-aligned and these two are the lowest energy states in the large $k$ limit. However, most of the energetically favoured states do have spin and orbital angular momentum aligned. The energy, as a function of $k$, of the states with $l \in [-4, 4]$ is plotted in Figure 5.8.

## 5.3 Conclusions

The Skyrme model provides a classical microscopic origin for the spin-orbit force based on the classical pion field structure. In this paper, we have constructed a model of interacting Skyrmions based on discs interacting through a contact potential which depends only on their relative colouring. The classical behaviour resembles a pair of cogwheels and our quantisation of the model has shown that most low energy states have their spin and orbital angular momentum aligned. However, the ground state does not.

To make any real predictions from the model we must extend it to three dimensions. This is considerably more difficult as there will be three relative orientations on which the potential depends, instead of one. There is also work to be done in the Skyrme model itself. Dynamical solutions of the model which look like a $B = 1$ Skyrmion orbiting a core have not yet been found.

# Chapter 6

# Conclusions and outlook

In this thesis we considered the quantisation of the Skyrme model, beyond the rigid body approach. We introduced vibrational quantisation, where the Skyrmions are allowed to deform and the corresponding vibrational modes are quantised. We argued that vibrational quantisation could solve several long-standing problems in the Skyrme model. One is that the vibrational modes contribute to the zero-point energy of the Skyrmion, reducing its binding energy which is much too large when one uses rigid body quantisation. Another problem is the spin of the ground state of the $B = 5$ Skyrmion. The known enhanced symmetry in the $B = 5$ vibrational manifold could lead to a reordering of the energy spectrum, remedying this problem. Both of these were merely suggestions and deserve further investigation.

In Chapter 3 the $B = 7$ sector was studied and we showed that the inclusion of a vibrational mode leads to a correct value of the ground state spin of Lithium-7 in the Skyrme model. In addition, a robust prediction was made: the ground state of $^7$Li is *larger* than the second excited state of the nucleus. Unfortunately, the root mean square matter radius is very difficult to measure experimentally. Hence, it is worth considering if this fact has any other physical consequences, such as giving information about the electromagnetic transition rates. Several states, including the low lying spin $\frac{1}{2}$ state, are excited in a different vibrational mode. To obtain a complete picture of the nucleus, this mode should also be studied in detail. It has been looked at in the small oscillation limit in [35]. The $B = 7$ Skyrmion now has the correct ground state spin and we have suggested a resolution for the incorrect

ground state spin of the $B = 5$ Skyrmion. If this suggestion works out in detail, we will have resolved the two problems detailed in Table 2.1. Hence, the Skyrme model may soon be able to successfully describe nuclei for the first eight baryon numbers.

We then studied the $B = 16$ sector of the Skyrme model. The Skyrmions in this sector can be described in terms of composite $B = 4$ cubes. These are analogous to $\alpha$-particles. Using the dynamics of the Skyrme model, we constructed a manifold of configurations which included the important tetrahedral and square configurations in a consistent way. We argued that our results give the best match to data of any model. Further, our work serves as an excellent starting point for future calculations. Only the $E$ vibration was understood beyond the small amplitude approximation. Using similar methods to those presented in Chapter 3, the $A$ and $F$ vibrations may also be understood in a global way. We made several approximations, such as estimating the energy contribution using perturbation theory, which could be improved on. Ultimately, one would like an ansatz for Skyrme configurations on the full vibrational manifold. Given the difficulty of finding an ansatz for static Skyrmions, this goal will likely require a radical new idea.

We considered a more speculative idea in the final chapter of the thesis. Here, we proposed that there is a low energy manifold of Skyrme configurations which look like a single Skyrmion orbiting a large core. Dynamically, it is energetically favourable for a single Skyrmion to roll around the core which gives a classical explanation of the spin-orbit force. However, once we quantised the system, the lowest energy states were those with spin and orbital angular momentum anti-aligned; contradicting our classical intuition. We neglected the internal structure of the core, which may rule out certain spin states. Further, the model will change significantly in the full 3D case. These should both be considered in future work.

# Appendix A

# Numerical techniques

Several times during this thesis, the calculations depended on numerically gener-
ated Skyrme configurations. In this appendix we detail the numerical techniques
used and how they were checked. There were three main numerically challenging
calculations required. They were:

1. To minimise the Skyrme functional in order to find Skyrmions for a given
   baryon number, and then calculate properties such as their masses and mo-
   ments of inertia.

2. To find how properties such as mass and moments of inertia change as a
   Skyrmion deforms. This is needed to generate the metric and potential of
   $\mathcal{V}_5$, a vibrational manifold of the $B = 7$ Skyrmion studied in Chapter 3.

3. To generate approximate dynamics of Skyrmions. This is used to explore the
   structure of the vibrational manifolds. For example, the modes displayed in
   Figures 3.4 and 4.2 are dynamically generated. Since these are used as moti-
   vation rather than for explicit calculations, we only require an approximation
   to the full dynamics.

We can accomplish all these tasks through the use of gradient flow. This generates
a path in configuration space. One begins with an initial configuration $\boldsymbol{\pi}_0$ and
evolves it according to

$$(\dot{\sigma}, \dot{\boldsymbol{\pi}}) = -\left( \frac{\delta \mathbb{M}_B}{\delta \sigma}, \frac{\delta \mathbb{M}_B}{\delta \boldsymbol{\pi}} \right) . \tag{A.1}$$

where $\mathbb{M}_B$ is the static energy functional (1.7). The energy of the Skyrme config-uration decreases along this path and the evolution ends at a stationery point in configuration space. Hence we can find Skyrmions by evolving this flow for a long time. Low energy dynamics can be approximated by

$$(\ddot{\sigma}, \ddot{\boldsymbol{\pi}}) = -\left(\frac{\delta\mathbb{M}}{\delta\sigma}, \frac{\delta\mathbb{M}}{\delta\boldsymbol{\pi}}\right), \tag{A.2}$$

where the fields are renormalised after each time step. A more accurate evolution would include a Lagrange multiplier term. However, since we only require the qualitative features of the scattering process, this was neglected for simplicity. The numerical code we developed was able to simulate equations (A.1) and (A.2) and to calculate static properties of the Skyrme configurations at each point.

To do the numerical calculations, we discretised a cubic grid with a fixed lattice spacing (usually 0.2 Skyrme length units in this thesis) and calculated spatial derivatives using 6$^\text{th}$ order finite differences. We choose 6$^\text{th}$ order as this allows for larger lattice spacing and hence fewer lattice points, saving computation time. Our lattices tend to have around $40^3$ points. The calculations in [29] and [13] use fourth order derivatives and use lattices with $201^3$ and $101^3$ points respectively. These are much larger than our lattices. Note that 6$^\text{th}$ order differences are appropriate for systems whose solutions are rather smooth, such as the standard Skyrme model. The gradient flow time parameter of (A.1) is discretised using first order finite differences. For the second order time evolution we use a leapfrog method as described in [13]. A non-standard aspect of Skyrmion numerics is that the fields satisfy the constraint

$$\sigma^2 + \boldsymbol{\pi}.\boldsymbol{\pi} = 1. \tag{A.3}$$

There are a few ways to implement this. We choose the numerically simple, though mathematically inelegant, solution of projecting the fields onto the 3-sphere every few time steps. This is stable provided the fields stay near the 3-sphere which can be arranged by taking a suitably small time step. We use periodic boundary conditions whose effect can be reduced by using a large enough box.

Each process begins with an initial Skyrme configuration. These are either generated from the rational map approximation [7] or by using a symmetrised product ansatz of existing numerically generated configurations. If the existing $SU(2)$-valued configurations are $U_1$ and $U_2$ then the new, composite field is given

| | $V_{11}$ | $U_{11}$ | $U_{33}$ |
|---|---|---|---|
| Results from our numerical calculation | 665.7 | 147.7 | 176.9 |
| Results from [29] | 667.6 | 148.2 | 177.4 |

Table A.1: A comparison between the non-zero moments of inertia of the $B = 4$ Skyrmion from our numerical code and those of the code present in [29].

| | $V_{11}$ | $V_{33}$ | $U_{11}$ | $U_{33}$ |
|---|---|---|---|---|
| Results from our numerical calculation | 6165 | 1065.5 | 272 | 301 |
| Results from the parallel axis theorem | 6183 | 1067 | 271 | 301 |

Table A.2: A comparison between the numerically calculated moments of inertia for the cluster configuration seen in Figure 3.4 and the theoretical values of the moments of inertia based on the parallel axis theorem.

by

$$U = \frac{U_1 U_2 + U_2 U_1}{\sqrt{2 + U_1 U_2 U_1^\dagger U_2^\dagger + U_2 U_1^\dagger U_2^\dagger U_1}} . \tag{A.4}$$

This breaks down if the denominator is zero. It was shown in [77] that this does not occur provided the solutions are well separated.

To test that the code gives appropriate results, we can compare against previous calculations. The $B = 4$ Skyrmion's mass has been calculated in [29], [78] and [9]. These papers give the mass as 5.177, 5.2 and 5.18 respectively. Our numerical code gives a value of 5.1802. Further, the $B = 4$ moments of inertia were calculated in [29]. The values taken from this work and our own code are shown in Table A.1, terms which are zero or are trivially related to those displayed have been neglected from the table. The results are similar, giving us confidence in our numerical code.

A check of the product ansatz (A.4) is to calculate the moments of inertia of a configuration generated using the method. We consider the $3 + 4$ configurations from Figure 3.4. The parallel axis theorem tells us how to estimate the moments of inertia. This theoretical calculation is compared to the numerically generated values in Table A.2. The numerical results are in good agreement with the theoretical calculation.

Since the dynamics defined in (A.2) are an approximation, there is no obvious

way to check the dynamical evolution is correct. We do reproduce several well known Skyrmion scatterings such as the 90° scattering of $B = 1$ Skyrmions and the twisted line scattering seen in Figure 2.2.

# Appendix B

# Electromagnetic transition rates

In this appendix we derive some formula to simplify the calculation of the electromagnetic transitions. The aim is to calculate matrix elements of the form

$$B(\mathrm{E}l, J_i \to J_f) = \frac{2J_f + 1}{2J_i + 1} \left| \int d^3r \, \langle \Psi_f | \, |\rho(\zeta, \boldsymbol{r}, \boldsymbol{\alpha}) r^l Y_l(\Omega)| \, |\Psi_i\rangle \right|^2 , \qquad (\text{B.1})$$

where $\rho$ is the charge density of the Skyrme configuration at $\zeta \in \mathcal{M}$, orientated according to some Euler angles $\boldsymbol{\alpha} = (\alpha, \beta, \gamma)$. The Skyrme configurations on $\mathcal{M}_E$, orientated as described in the text occur when $\boldsymbol{\alpha} = \boldsymbol{0}$. The integral in (B.1) is taken over space with $\Omega$ being the angular coordinates. The rovibrational wavefunctions can be expressed as

$$|\Psi\rangle = \sum_i u_i(\zeta) \, |\Theta\rangle_i , \qquad (\text{B.2})$$

where $|\Theta\rangle_i$ are the standard spin states. Substituting (B.2) into (B.1), we find that we must evaluate terms of the form

$$\frac{2J_f + 1}{2J_i + 1} \left| \int d\zeta \int d^3r \, \langle J_f L_3| \, |u_f(\zeta)\rho(\zeta, \boldsymbol{r}, \boldsymbol{\alpha}) Y^l(\Omega) u_i(\zeta)| \, |J_i L_3'\rangle \right|^2 . \qquad (\text{B.3})$$

Note that (B.3) can be written as

$$\frac{2J_f + 1}{2J_i + 1} \left| \int u_i(\zeta) u_f(\zeta) \left( \int d^3r \, \langle J_f L_3| \, |\rho(\zeta, \boldsymbol{r}, \boldsymbol{\alpha}) Y^l(\Omega)| \, |J_i L_3'\rangle \right) d\zeta \right|^2 , \qquad (\text{B.4})$$

so that we can momentarily neglect the vibrational wavefunction contribution and focus on the rotational part. The Wigner-Eckart theorem gives that

$$\frac{2J+1}{2J'+1}\left|\int d^3r \left\langle JL_3\right| |\rho(\zeta,\boldsymbol{r},\boldsymbol{\alpha})Y^l(\Omega)| \left|J'L_3'\right\rangle\right|^2$$
$$= \frac{2J+1}{2J'+1}\left|\int d^3r \frac{1}{\langle J'J_3'lm|JJ_3\rangle}\left\langle JL_3J_3\right|\rho(\zeta,\boldsymbol{r},\boldsymbol{\alpha})Y_{lm}(\Omega)\left|J'L_3',J_3'\right\rangle\right|^2,$$

(B.5)

provided that the Clebsch-Gordon coefficients $\langle J'J_3'lm|JJ_3\rangle$ are non-zero.

The expression (B.5) is complicated due to the dependency of the charge density on $\boldsymbol{\alpha}$. This can be removed with the help of a useful identity that we shall now obtain. Consider the charge density, expanded in terms of the spherical harmonics

$$\rho(\zeta,\boldsymbol{r},\boldsymbol{0}) = \sum_l \left(\sum_{m=-l}^l c_{lm}(r)Y_{lm}(\theta,\phi)\right).$$

(B.6)

This is valid for Skyrme configurations orientated as defined in the text. The above expansion transforms simply under rotations. For a Skyrme configurations in an arbitrary orientation, the charge density is

$$\rho(\zeta,\boldsymbol{r},\boldsymbol{\alpha}) = \sum_{l=0}^\infty \left(\sum_{m=-l}^l c_{lm}(r)\sum_{m'=l}^l D_{mm'}^l(\alpha,\beta,\gamma)Y_{lm'}(\theta,\phi)\right).$$

(B.7)

Using the orthogonality of the spherical harmonics in (B.6) we find that

$$c_{lm}(r) = \int Y_{lm}(\Omega)\rho(\zeta,\boldsymbol{r},\boldsymbol{0})\,d\Omega.$$

(B.8)

This can then be used to simplify (B.5) as follows

$$\int d^3r \rho(\zeta,\boldsymbol{r},\boldsymbol{\alpha})Y_{lm}r^l = \int \sum_{m'=-l}^l r^l c_{lm'}(r)D_{mm'}^l(\alpha,\beta,\gamma)d^3r$$
$$= \sum_{m'=-l}^l \int r^l Y_{lm'}(\Omega)\rho(\zeta,\boldsymbol{r},\boldsymbol{0})\,d^3r\, D_{mm'}^l(\alpha,\beta,\gamma)$$
$$\equiv \sum_{m'} \tilde{Q}_{lm'}D_{mm'}^l(\alpha,\beta,\gamma).$$

(B.9)

where the modified multipole tensor is defined as

$$\tilde{Q}_{lm}(\zeta) = \int \rho(\zeta, \boldsymbol{r}, \boldsymbol{0}) r^l Y_{lm}(\Omega) \, d^3r \,. \tag{B.10}$$

With these expressions, we may factor out the Euler angle dependence in the transition rate formula. Equation (B.5) becomes

$$\frac{2J+1}{2J'+1} \left| \frac{1}{\langle J'L_3'lm|JL_3 \rangle} \sum_{m'} \langle JL_3J_3| \, \tilde{Q}_{lm'}(\zeta) D^l_{mm'} \, |J'L_3', J_3' \rangle \right|^2 \tag{B.11}$$

$$= \left| \frac{1}{\langle J'J_3'lm|JJ_3 \rangle} \sum_{m'} \langle J'J_3'lm|JJ_3 \rangle \langle J'L_3'lm'|JL_3 \rangle \, \tilde{Q}_{lm'}(\zeta) \right|^2 \tag{B.12}$$

$$= \left| \sum_{m'} \langle J'L_3'lm'|JL_3 \rangle \, \tilde{Q}_{lm'}(\zeta) \right|^2 \,, \tag{B.13}$$

which can then be used to evaluate specific transition rates. The vibrational wavefunctions are now reinstated and the final result is

$$\frac{2J_f+1}{2J_i+1} \left| \int d\zeta \int d^3r \, \langle J_f L_3| \, |u_f(\zeta)\rho(\zeta, \boldsymbol{r}, \boldsymbol{\alpha}) Y^l(\Omega) u_i(\zeta)| \, |J_i L_3' \rangle \right|^2 \tag{B.14}$$

$$= \left| \int u_i(\zeta) u_f(\zeta) \sum_{m'} \langle J'L_3'lm'|JL_3 \rangle \, \tilde{Q}_{lm'}(\zeta) d\zeta \right|^2 \,. \tag{B.15}$$

Using this result, we can find simple formulae for many transition rates. We will do so for five transitions. Two simple cases were studied in the main body of the text.

### E3: Sign to trivial

Consider the E3 transition from the spin $3^-$ state at 6.47 MeV to the ground state. The vibrational wavefunctions fall into the sign and trivial representations respectively. The relevant wavefunctions are

$$|\Psi_i\rangle = \phi^{(e)}(\zeta)\sqrt{\frac{1}{2}} \left(|3,2\rangle - |3,-2\rangle\right) \tag{B.16}$$

$$|\Psi_f\rangle = \phi^{(a)}(\zeta) |0,0\rangle \,, \tag{B.17}$$

where the $\phi$ are normalised so that $\langle \Psi | \Psi \rangle = 1$. The transition is

$$
\begin{aligned}
B(\text{E3}, 3^- \to 0^+) &= \frac{1}{2} \left| \int d\zeta \phi^{(e)}(\zeta) \phi^{(a)}(\zeta) \sum_{m'} \left( \langle 323m'|00 \rangle - \langle 3-23m'|00 \rangle \right) \tilde{Q}_{3m'} \right|^2 \\
&= \frac{1}{14} \left| \int d\zeta \phi^{(e)}(\zeta) \phi^{(a)}(\zeta) \left( \tilde{Q}_{32} - \tilde{Q}_{3-2} \right) \right|^2 .
\end{aligned} \tag{B.18}
$$

**E1: Trivial to Sign**

There is an E1 transition between the spin $4^+$ at 10.35 MeV and the spin $3^-$ state at 6.47 MeV. The relevant wavefunctions are

$$
|\Psi_i\rangle = \phi^{(a)}(\zeta) \sqrt{\frac{5}{24}} \left( |4, 4\rangle + \sqrt{\frac{14}{5}} |4, 0\rangle + |4, -4\rangle \right) \tag{B.19}
$$

$$
|\Psi_f\rangle = \phi^{(e)}(\zeta) \sqrt{\frac{1}{2}} \left( |3, 2\rangle - |3, -2\rangle \right) . \tag{B.20}
$$

The Clebsch-Gordon coefficients in the calculation take the form $\langle 441m'|32 \rangle$ or $\langle 401m'|32 \rangle$. Both of these are zero unless $m' = \pm 2$. However, $m'$ can only take values between $-1$ and $1$. So, the transition is zero due to the structure of the rotational states.

**E1: Sign to Doublet**

The E1 transition between the $3^-$ state at 6.47 MeV and the $2^+$ state at 6.66 MeV is also zero, but for a different reason. The relevant wavefunctions are

$$
|\Psi_i\rangle = \phi^{(e)}(\zeta) \sqrt{\frac{1}{2}} \left( |3, 2\rangle - |3, -2\rangle \right) \tag{B.21}
$$

$$
|\Psi_f\rangle = \frac{1}{2\sqrt{2}} (u^{(i)} - v^{(i)}) \left( |2, 2\rangle + |2, -2\rangle \right) - \frac{\sqrt{3}}{2} (u^{(i)} + v^{(i)}) |2, 0\rangle , \tag{B.22}
$$

giving the transition

$$
\begin{aligned}
B(\text{E1}, 3^- \to 2^+) &= \left| \int \sum_{m'} \frac{1}{4} (u^{(i)} - v^{(i)}) \phi^{(e)} \left( \langle 321m'|22 \rangle - \langle 3-21m'|2-2 \rangle \right) Q_{1m'} d\zeta \right| \\
&= \frac{5}{4 \times 21} \left| \int (u^{(i)} - v^{(i)}) \phi^{(b)} \tilde{Q}_{10} \, d\zeta \right|^2
\end{aligned} \tag{B.23}
$$

The operator inside the integral is antisymmetric around $\eta = \frac{1}{2}$, giving a zero result.

Similarly the E1 transition between the excited $4^+$ state at 12.62 MeV and the $3^-$ state at 6.47 MeV is

$$
\begin{aligned}
B(\text{E1}, 4_e^+ \to 3^-) &= \frac{1}{12} \left| \int (u - v) \phi^{(b)} \tilde{Q}_{10} \, d\zeta \right|^2 \\
&= \frac{7}{5} B(E1, 3^- \to 2^+) \\
&= B(E1, 2^+ \to 3^-) = 0 \,.
\end{aligned}
\tag{B.24}
$$

**E2: Doublet to Doublet**

The transition between two doublet states is slightly more complicated; consider the first excited $4^+$ state at 12.62 MeV and the lowest energy $2^+$ state at 6.66 MeV. These have wavefunctions

$$
\begin{aligned}
|\Psi_i\rangle &= \frac{2}{\sqrt{5}} (u \,|4, 0\rangle_x + v \,|4, 0\rangle_y + w \,|4, 0\rangle) \\
&= \sqrt{\frac{7}{32}} (u + v) \,(|4, 4\rangle + |4, -4\rangle) - \sqrt{\frac{1}{8}} (u - v) \,(|4, 2\rangle + |4, -2\rangle) - \sqrt{\frac{5}{16}} (u + v) \,|4, 0\rangle
\end{aligned}
\tag{B.25}
$$

$$
|\Psi_f\rangle = \frac{1}{2\sqrt{2}} (u - v) \,(|2, 2\rangle + |2, -2\rangle) - \frac{\sqrt{3}}{2} (u + v) \,|2, 0\rangle \,.
\tag{B.26}
$$

We neglect the vibrational superscript from now on, for ease of reading. The transition rate between these states is given by

$$B(\text{E2}, 4^+ \to 2^+)$$

$$= \left| \int \sum_{m'} \left( \frac{\sqrt{7}}{\sqrt{256}} (u^2 - v^2)(\langle 442m'|22\rangle + \langle 4-42m'|2-2\rangle) \right. \right.$$

$$- \frac{1}{8}(u-v)^2(\langle 422m'|22\rangle + \langle 4-22m'|2-2\rangle)$$

$$+ \sqrt{\frac{3}{32}}(u^2 - v^2)(\langle 422m'|20\rangle + \langle 4-22m'|20\rangle)$$

$$\left. \left. - \sqrt{\frac{5}{128}}(u^2 - v^2)(\langle 402m'|22\rangle + \langle 402m'|2-2\rangle + \frac{15}{64}(u+v)^2 \langle 402m'|20\rangle) \right) \tilde{Q}_{2m'} d\zeta \right|^2$$

$$= \left| \int \left( \frac{\sqrt{5}}{4\sqrt{7}}(u^2 - v^2)(\tilde{Q}_{22} + \tilde{Q}_{2-2}) - \frac{\sqrt{15}}{12\sqrt{14}}(u-v)^2 \tilde{Q}_{20} + \frac{\sqrt{15}}{3\sqrt{14}}(u+v)^2 \tilde{Q}_{20} \right) d\zeta \right|^2$$

$$= \left| \int \left( \frac{\sqrt{5}}{4\sqrt{7}}(u^2 - v^2)(\tilde{Q}_{22} + \tilde{Q}_{2-2}) + \sqrt{\frac{5}{14}}(2(u+v)^2 - u^2 - v^2)\tilde{Q}_{20} \right) d\zeta \right|^2 .$$

(B.27)

The final line is rewritten to show the link between the structure of the spherical harmonics and the structure of the vibrational wavefunctions.

### E4: Doublet to trivial

Finally, we calculate the transition between the excited $4^+$ state at 12.62 MeV and the ground state (or first excited state). The relevant states are

$$|\Psi_i\rangle = \sqrt{\frac{7}{32}}(u+v)(|4,4\rangle + |4,-4\rangle) - \sqrt{\frac{1}{8}}(u-v)(|4,2\rangle + |4,-2\rangle) - \sqrt{\frac{5}{16}}(u+v)|4,0\rangle$$

(B.28)

$$|\Psi_f\rangle = \phi|0,0\rangle ,$$

(B.29)

which leads to the transition

$$B(\text{E4},4_2^+ \to 0^+)$$

$$= \left| \int \sum_{m'} \phi \left( \sqrt{\frac{7}{32}}(u+v) \left( \langle 444m'|00 \rangle - \sqrt{\frac{10}{7}} \langle 404m'|00 \rangle + \langle 4-44m'|00 \rangle \right) \right. \right.$$

$$\left. \left. - \sqrt{\frac{1}{8}}(u-v)(\langle 424m'|00 \rangle + \langle 4-24m'|00 \rangle) \right) Q_{4m'} d\zeta \right|^2$$

$$= \left| \int \phi \left( \frac{\sqrt{7}}{12\sqrt{2}}(u+v) \left( \tilde{Q}_{44} - \sqrt{\frac{10}{7}} \tilde{Q}_{40} + \tilde{Q}_{4-4} \right) - \frac{1}{6\sqrt{2}}(u-v)(\tilde{Q}_{42} + \tilde{Q}_{4-2}) \right) \right|^2 .$$

$$\text{(B.30)}$$

# Bibliography

[1] T.H.R. Skyrme, A nonlinear field theory. *Proc. Roy. Soc.* **A260** (1961) 127.

[2] T. S. Walhout and J. Wambach, Nucleon-nucleon potential in the Skyrme model: beyond the product approximation. *Phys. Rev. Lett.* **67** (1991) 314.

[3] E. Witten, Baryons in the $1/N$ expansion. *Nucl. Phys.* **B160** (1979) 57.

[4] T. Sakai and S. Sugimoto, Low energy hadron physics in holographic QCD. *Prog. Theor. Phys.* **113** (2005) 843.

[5] L. Faddeev, Some comments on the many dimensional solitons. *Lett. Math. Phys.* **1** (1976) 289.

[6] A. P. Balachandran, G. Marmo, B. S. Skagerstam and A. Stern, Classical topology and quantum states. *World Scientific Publishing: Singapore* (1990).

[7] C. J. Houghton, N. S. Manton and P. M. Sutcliffe, Rational maps, monopoles and Skyrmions. *Nucl. Phys.* **B510** (1998) 507.

[8] M. F. Atiyah and N. S. Manton, Skyrmions from instantons. *Phys. Lett.* **B222** (1989) 438.

[9] D. T. J. Feist, P. H. C. Lau and N. S. Manton, Skyrmions up to baryon number 108. *Phys. Rev.* **D87** (2013) 085034.

[10] W. Bauhoff, H. Schultheis and R. Schultheis, Alpha cluster model and the spectrum of $^{16}$O. *Phys. Rev.* **C 29** (1984) 1046.

[11] S. G. Nelmes, Skyrmion stars. *Durham University, PhD thesis.* http://etheses.dur.ac.uk/5258 (2012).

[12] N. Manton and P. Sutcliffe, Topological Solitons. *Cambridge University Press: Cambridge* (2004).

[13] R. Battye and P. Sutcliffe, Skyrmions, fullerenes and rational maps. *Rev. Math. Phys.* **14** (2002) 29.

[14] O. Manko, N. S. Manton and S. Wood, Light nuclei as quantized Skyrmions. *Phys. Rev.* **C76** (2007) 055203.

[15] C. Adam, J. Sánchez-Guillén and A. Wereszczyński, A Skyrme-type proposal for baryonic matter. *Phys. Lett.* **B691** (2010) 105.

[16] M. Gillard, D. Harland and J. M. Speight, Skyrmions with low binding energies. *Nucl. Phys.* **B895** (2015) 272.

[17] M. Gillard, D. Harland, E. Kirk, B. Maybee and J. M. Speight, A point particle model of lightly bound skyrmions. *Nucl. Phys.* **B917** (2017) 286.

[18] P. M. Sutcliffe, Skyrmions, instantons and holography. *JHEP* **08:019** (2010).

[19] P. M. Sutcliffe, Skyrmions in a truncated BPS theory. *JHEP* **1104:045** (2011).

[20] N. S. Manton, A remark on the scattering of BPS monopoles. *Phys. Lett.* **B110** (1982) 54.

[21] G. S. Adkins, C. R. Nappi and E. Witten, Static properties of nucleons in the Skyrme model. *Nucl. Phys.* **B 228** (1983) 552.

[22] L. D. Landau and E. M. Lifshitz, Mechanics. *Pergamon Press Limited: Oxford* (1969).

[23] D. Finkelstein and J. Rubinstein, Connection between Spin, Statistics, and Kinks. *J. Math. Phys.* **9** (1968) 1762.

[24] D. Giulini, On the possibility of spinorial quantisation in the Skyrme model. *Mod. Phys. Lett.* **A8** (1993) 1917.

[25] E. Witten, Global aspect of current algebra. *Nucl. Phys.* **B223** (1983) 422.

[26] S. Krusch, Homotopy of Rational Maps and the Quantization of Skyrmions. *Ann. Phys.* **304** (2003) 103.

[27] P. Irwin, Zero mode quantization of multi-Skyrmions. *Phys. Rev.* **D61** (2000) 114024.

[28] R. A. Battye and P. M. Sutcliffe, Multi-soliton dynamics in the Skyrme model. *Phys. Lett.* **B391** (1997) 150.

[29] R. A. Battye, M. Haberichter and S. Krusch, Classically isospinning Skyrmion solutions. *Phys. Rev.* **D90** (2014) 125035.

[30] P. H. C. Lau and N. S. Manton, States of Carbon-12 in the Skyrme Model. *Phys. Rev. Lett.* **113** (2014) 232503.

[31] F. Meier and H. Walliser, Quantum Corrections to Baryon Properties in Chiral Soliton Models. *Phys. Rept.* **289** (1997) 383.

[32] R. Leese, N. S. Manton and B. Schroers, Attractive Channel Skyrmions and the Deuteron. *Nucl. Phys.* **B442** (1995) 228.

[33] C. J. Halcrow, Vibrational quantisation of the $B = 7$ Skyrmion. *Nucl. Phys.* **B904** (2016) 106.

[34] Y. C. Tang, K. Wildermuth and L. D. Pearlstein, Cluster Model Calculation on the Energy Levels of the Lithium Isotopes. *Phys. Rev.* **123** (1961) 548.

[35] W. K. Baskerville, Vibrational spectrum of the $B = 7$ Skyrme soliton. *arXiv:* (1999) hep-th/9906063.

[36] G. W. Gibbons and N. S. Manton, Classical and quantum dyanmics of BPS monopoles. *Nucl. Phys.* **B274** (1986) 183.

[37] E. Braaten and L. Carson, Deuteron as a Soliton in the Skyrme Model. *Phys. Rev. Lett.* **56** (1986) 3525.

[38] D. R. Tilley, C. M. Cheves, J. L. Godwin, G. M. Hale, H. M. Hofmann, J. H. Kelley, C. G. Sheu and H. R. Weller, Energy levels of light nuclei $A = 5, 6, 7$. *Nucl. Phys.* **A708** (2002) 3.

[39] S. Krusch and J. M. Speight, Quantum lump dynamics on the two-sphere. *Comm. Math. Phys.* **322** (2013) 95.

[40] I. Floratos, Multi-skyrmion solutions of a sixth order skyrme model. *Durham University, PhD thesis.* http://etheses.dur.ac.uk/3988 (2001).

[41] C. J. Halcrow, C. King and N. S. Manton, A dynamical $\alpha$-cluster model of $^{16}O$. *Phys. Rev.* **C95** (2017) 031303.

[42] J. A. Wheeler, Molecular viewpoints in nuclear structure. *Phys. Rev.* **52** (1937) 1083.

[43] J. K. Perring and T. H. R. Skyrme, The alpha-particle and shell models of the nucleus. *Proc. Phys. Soc. Lond.* **A69** (1956) 600.

[44] W. H. Bassichis and G. Ripka, A Hartree-Fock calculation of excited states of $O^{16}$. *Phys. Lett.* **15** (1965) 320.

[45] J. M. Irvine, C. D. Latorre and V. F. E. Pucknell, The structure of $^{16}O$; a review of the theory. *Adv. in Phys.* **20:88** (1971) 661.

[46] J. P. Elliott and B. H. Flowers, The odd-parity states of $^{16}$) and $^{16}N$. *Proc. Roy. Soc.* **A242** (1957) 57.

[47] D. M. Brink and G. F. Nash, Excited states in Oxygen 16. *Nucl. Phys.* **40** (1963) 608.

[48] A. Volya and Y. M. Tchuvil'sky, Nuclear clustering using a modern shell model approach. *Phys. Rev.* **C91** (2015) 044319.

[49] E. Epelbaum, H. Krebs, T. A. Lähde, D. Lee, U. G. Mei$\beta$ner and G. Rupak, Ab initio calculation of the spectrum and structure of $^{16}O$. *Phys. Rev. Lett.* **112** (2014) 102501.

[50] Y. Kanada-En'yo and Y. Hidaka, Tetrahedral shape and surface density wave of $^{16}O$ caused by $\alpha$-cluster correlations. *arXiv* (2016) 1608.03642.

[51] D. M. Dennison, Energy levels of the $O^{16}$ nucleus. *Phys. Rev.* **96** (1954) 378.

[52] D. Robson, Evidence for the tetrahedral nature of $^{16}$O. *Phys. Rev. Lett.* **42** (1979) 876.

[53] D. M. Brink, H. Friedrich, A. Weiguny and C. W. Wong, Investigation of the alpha-particle model for light nuclei. *Phys. Lett.* **33B** (1970) 143.

[54] H. Friedrich, H. Hüsken and A. Weiguny, Alpha clustering in light nuclei with density dependent forces. *Phys. Lett.* **38B** (1972) 199.

[55] R. Battye, N. S. Manton and P. Sutcliffe, Skyrmions and the $\alpha$-particle model of nuclear physics. *Proc. Roy. Soc. Lond.* **A463** (2007) 261.

[56] M. Haberichter, P. H. C. Lau and N. S. Manton, Electromagnetic transition strengths for light nuclei in the Skyrme model. *Phys. Rev.* **C93** (2016) 034304.

[57] J. Zhang and W. D. M. Rae, Systematics of a 2-dimensional $\alpha$-cluster configurations in $4N$ nuclei from $^{12}$C to $^{44}$Ti. *Nucl. Phys.* **A564** (1993) 252.

[58] G. Royer, G. Ramasamy and P. Eudes, Energies of molecular structures in $^{12}$C, $^{16}$O, $^{20}$Ne, $^{24}$Mg, and $^{32}$S. *Phys. Rev.* **C92** (2015) 054308.

[59] G. F. Bertsch and W. Bertozzi, $\alpha$-partcle model of $^{16}$O. *Nucl. Phys.* **A165** (1971) 199.

[60] N. Onishi and R. K. Sheline, The tetrahedral deformation in the nucleus $^{16}$O. *Nucl. Phys.* **A165** (1971) 180.

[61] R. Bijker and F. Iachello,Evidence for tetrahedral symmetry in $^{16}$O. *Phys. Rev. Lett.* **112** (2014) 152501.

[62] R. Bijker and F. Iachello, The algebraic cluster model: structure of $^{16}$O. *Nucl. Phys.* **A957** (2017) 154.

[63] H. M. Farkas and I. Kra, Theta constants, Riemann surfaces and the modular group. *American Mathematical Society: Providence RI* (2001).

[64] J. H. Kelley, D. R. Tilley, H.R. Weller and C. M. Cheves, Energy levels of light nuclei $A = 16 - 17$. *Nucl. Phys.* **A564** (1993) 1.

[65] W. Bauhoff, H. Schultheis and R. Schultheis, Alpha cluster model and the spectrum of $^{16}$O. *Phys. Rev.* **C29** (1984) 1046.

[66] R. Bijker and F. Iachello, Evidence for tetrahedral symmetry in $^{16}$O. *Phys. Rev. Lett.* **112** (2014) 152501.

[67] C. J. Halcrow and N. S. Manton, A Skyme model approach to the spin-orbit force. *JHEP* **1501:016** (2016).

[68] W. Greiner and J. A. Maruhn, Nuclear Models. *Springer: Berlin* (1996).

[69] O. Haxel, J. Hans, D. Hensen and H. E. Suess, On the "magic numbers" in nuclear structure. *Phys. Rev.* **75** (1949) 1766.

[70] M. Goeppert-Mayer, On closed shells in nuclei II. *Phys. Rev.* **75** (1949) 1969.

[71] P. Ring, Relativistic mean field theory in finite nuclei. *Prog. Part. Nucl. Phys.* **37** (1996) 193.

[72] Y. K. Gambhir, P. Ring and A. Thimet, Relativistic mean field theory for finite nuclei. *Ann. Phys.* **198** (1990) 132.

[73] D. O. Riska and E. B. Nyman, Spin-orbit interaction in the Skyrme model. *Phys. Lett.* **B183** (1987) 7.

[74] N. S. Manton, Classical Skyrmions – static solutions and dynamics. *Math. Meth. Appl. Sci.* **35** (2012) 1188.

[75] N. S. Manton, Unstable manifolds and soliton dynamics. *Phys. Rev. Lett.* **60** (1988) 1916.

[76] M. Abramowitz and I. Stegun, Handbook of Mathematical Functions with Formulas, Graphs and Mathematical Tables (Chapter 20). *Dover Publications: New York* (1964).

[77] P. H. C. Lau, Construction and Quantisation of Skyrmions. *University of Cambridge, PhD Thesis* (2015).

[78] R. Battye and P. M. Sutcliffe, Skyrmions and the pion mass. *Nucl. Phys.* **B705** (2005) 384.